Structure and Dynamics of Complex Liquids - The Phase Behaviour of Silica-PNIPAm Nanogels

Dissertation
zur Erlangung des Doktorgrades
an der Fakultät für
Mathematik, Informatik und Naturwissenschaften
Fachbereich Physik
der Universität Hamburg

vorgelegt von

Lara Sophie Frenzel

Hamburg

2019

Gutachter der Dissertation:	Prof. Dr. Gerhard Grübel Prof. Dr. Alf Mews
Zusammensetzung der Prüfungskommission:	Prof. Dr. Gerhard Grübel Prof. Dr. Alf Mews Prof. Dr. Edgar Weckert Prof. Dr. Michael Potthoff Prof. Dr. Nina Rohringer
Vorsitzender der Prüfungskommission:	Prof. Dr. Michael Potthoff
Datum der Disputation:	18.10.2019
Vorsitzender Fach-Promotionsausschusses Physik:	Prof. Dr. Michael Potthoff
Leiter des Fachbereichs Physik:	Prof. Dr. Wolfgang Hansen
Dekan der Fakultät für Mathematik, Informatik und Naturwissenschaften:	Prof. Dr. Heinrich Graener

Abstract

In this thesis, the structure and dynamics of highly concentrated core-shell nanogel particles composed of a silica core and a poly(N-isoproylacrylamide) (PNIPAm) shell suspended in water are studied. The particles were synthesised with different core-to-shell size ratios and prepared at various concentrations with volume fractions Φ_{eff} between approximately 0.004 and 2. X-ray photon correlation spectroscopy (XPCS) enables to follow the dynamical, small-angle X-ray scattering (SAXS) the structural changes of the thermo-responsive nanogel particles which undergo a volume phase transition at a so-called lower critical solution temperature (LCST) of 32°C. All samples were studied in a broad temperature range around the LCST with approximately $15°\text{C} < T < 45°\text{C}$ and the main focus is on densely-packed systems.

For a system with $\Phi_{\text{eff}} = 0.55$, the structural relaxation time τ_{c} was found to decrease with increasing temperature. Above the LCST, the structural relaxation time initially continues to decrease. The effect is accompanied by a transition from stretched to compressed exponential behaviour of the intensity autocorrelation functions, which could be determined by analysing the intensity autocorrelation functions. Upon further heating a sudden slowing down at a critical temperature $T_{\text{c}} \approx 37°\text{C}$. In parallel, the q-dependence of the relaxation time shows an anomalous change from $\tau_{\text{c}} \propto q^{-3}$ to $\tau_{\text{c}} \propto q^{-1}$. The results reveal a temperature-induced transition from swollen repulsive particles with polymer driven dynamics at lower temperatures $T < T_{\text{c}}$ towards a colloidal gel composed of collapsed attractive particles. The transition of structure and dynamics shows a distinct dependency on the effective particle volume fraction. Below a critical concentration no transition upon heating was found.

The de-swelling behaviour of the PNIPam nanogel was influenced with the addition of Trimethylamine *N*-oxide (TMAO) to the concentrated particle suspension. With increasing TMAO concentration, a shift of the LCST towards lower temperatures and a preferential hydrophobic state could be determined.

With all results a full phase diagram of a silica-PNIPAm core-shell system is presented as a function of temperature and concentration. It spans from dilute suspensions to an effective volume fraction of more than ninety percent covering two liquid phases, a structural rearrangement phase and a colloidal gel phase.

Kurzfassung

Diese Arbeit untersucht die Struktur und Dynamik hochkonzentrierter Kern-Schale Nanogel-Partikel, die sich aus einem Silizumoxidkern (Silica) und einer Hülle aus Poly(N-isoproylacrylamid) (PNIPAm) zusammensetzen und in Wasser suspendiert sind. Die Silica-PNIPAm-Partikel wurden mit verschiedenen Größenverhältnissen von Kern zu Schale synthetisiert und zu effektiven Volumenbrüchen Φ_{eff} zwischen 0.004 und 2 aufkonzentriert. PNIPAm zeigt einen Phasenübergang bei einer kritischen Temperatur LCST (engl. *Lower Critical Solution Temperature*) von 32°C, bei der das PNIPAm Nanogel von einem hydrophilen geschwollenen Zustand zu einem kollabierten dehydrierten Zustand übergeht.

Mit Röntgenphotonenkorrelationsspektroskopie (XPCS) und Kleinwinkelröntgenstreuung (SAXS) ist es möglich die Dynamik und Struktur eines solchen kolloidalen Systems zu charakterisieren. Alle Proben wurden in einem breiten Temperaturbereich von zirka $15°\text{C} < T < 45°\text{C}$ um die LCST untersucht wobei der Fokus auf dichtgepackten Systemen lag.

Für ein System mit $\Phi_{\text{eff}} = 0.55$ nimmt die strukturelle Relaxationszeit τ_{c} bei ansteigender Temperatur ab. Für Temperaturen oberhalb der LCST verringert sich die Relaxationszeit zunächst weiterhin, während die Intensitätsautokorrelationsfunktionen einen Übergang von gestreckten zu komprimierten Exponentialfunktionen zeigen. Bei weiterer Temperaturerhöhung wird eine plötzliche Verlangsamung der Partikel bei einer kritischen Temperatur $T_{\text{c}} \approx 37°\text{C}$ beobachtet. Zeitgleich zeigt die q-Abhängigkeit der Relaxationszeit eine anomale Änderung von $\tau_{\text{c}} \propto q^{-3}$ to $\tau_{\text{c}} \propto q^{-1}$. Die Ergebnisse weisen auf einen Übergang von hydrophilen, repulsiven Partikeln mit polymergelenkter Dynamik bei $T < T_{\text{c}}$ zu einem kolloidalen Gel aus kollabierten, attraktiven Partikeln. Dieser Übergang von Struktur und Dynamik ist stark konzentrationsabhängig. Unterhalb einer kritischen Konzentration weist das System keinen temperaturinduzierten Übergang auf.

Der Phasenübergang des konzentrierten Silica-PNIPAm Nanogels wurde durch Zugabe von Trimethylamin N-oxid (TMAO) beeinflusst. Mit erhöhter TMAO-Konzentration wurde eine Verschiebung der LCST zu niedrigeren Temperaturen und ein durch TMAO induzierter kollabierter Zustand analysiert.

Auf Basis aller Ergebnisse kann ein vollständiges Phasendiagramm für kolloidales Silica-PNIPAm als Funktion von Temperatur und Konzentration aufgestellt werden. Es reicht von verdünnten Suspensionen bis zu effektiven Volumenbrüchen von über neunzig Prozent und umfasst zwei flüssige Phasen, eine strukturelle Reorganisationsphase und die Phase eines kolloidalen Gels.

Contents

1 Introduction **1**

2 Colloidal Systems **3**

2.1 Steric stabilization 3

2.2 Charge stabilization 5

2.3 Colloidal nanogels 7

2.3.1 Poly(*N*-isopropylacrylamide) 8

2.3.2 Effects of co-solvents on PNIPAm systems 10

2.3.3 Core-Shell structured PNIPAm nanogels 11

3 Scattering Methods **13**

3.1 The interaction of X-rays with matter 13

3.2 Small-angle X-ray scattering 15

3.2.1 Static scattering of single particles 15

3.2.2 Scattering of disperse systems 17

3.2.3 Scattering from systems with interparticle interactions 19

3.3 X-ray photon correlation spectroscopy 21

3.3.1 Dynamics of colloidal suspensions 23

4 Experimental Details **25**

4.1 Particle synthesis 25

4.2 Sample characterization and preparation 26

4.2.1 Experimental procedure 27

5 Structural and Dynamical Properties of Silica-PNIPAm **31**

5.1 Structural properties: SAXS results 31

5.1.1 Form factor analysis 31

5.1.2 Structural properties of dense-packed silica-PNIPAm 33

5.1.3 Influence of the shell size on the structure formation 34

5.1.4 Ultra-small-angle X-Ray scattering 37

5.1.5 Reversibility 41

5.2 Structural influence of TMAO as co-solvent 43

5.3 Interpretation and discussion of the structural properties 44

5.4 Dynamic properties 46

5.4.1 Radiation damage 46

5.4.2 Dynamics of non-interacting silica-PNIPAm particles 47

5.4.3 Dynamics of concentrated suspensions 48

5.4.4 Influence of the shell size on the dynamics 56

5.4.5 Ultra-small-angle X-Ray photon correlation spectroscopy 58
5.4.6 Reversibility 60
5.5 Dynamical influence of TMAO as co-solvent 62
5.6 Interpretation and discussion of the dynamical properties 64
5.7 The phase diagram of silica-PNIPAm 67

6 Conclusion and Outlook **69**

Bibliography **83**

Publications **85**

Acknowledgements **87**

Eidesstattliche Versicherung **91**

1 Introduction

Colloids, or more precisely colloidal dispersions, are two-phase systems composed of nano- to micrometer sized insoluble particles in a homogeneous molecular phase. Such colloidal systems are abundant and known for numerous applications. Examples are: Paints that are composed of pigments in a solvent; black ink made from colloidal carbon; cosmetics, such as sunscreens, contain light reflecting particles; or pharmaceuticals where colloids are utilised for targeted drug delivery [1,2]. Scientifically, colloidal systems are powerful model systems used for fundamental research on fluids and solids. The interparticle interactions allow self-organisation and the system can exhibit different phases such as liquid, gel-like, glassy, or even crystalline states. Variation of the particle number-density or tuning of the interparticle interactions provides a wide range of systems from dilute, non-interacting samples - where the particles undergo Brownian motion due to thermal fluctuations of the surrounding solvent - to systems with strong interparticle correlation and confined dynamics. With particles playing the role of atoms but being large enough for observation, much can be learned about phase behaviour and traditional atomic materials [2,3]. For the understanding of phase behaviour, temperature-tunable colloidal nanogels have been and still are a crucial sample system. Those stimulus-responsive cross-linked polymer networks find as colloidal nanogels increasing use in biomedicine and pharmaceutics [4, 5]. Special interest has been given to core–shell structured particles with single nanoparticle cores and a stimuli-responsive polymer shell [6–9]. The aim of such so-called smart particles is to combine the sensitivity and response to changes of the environment in the particle surface with interesting optical or magnetic properties of the solid core particles.

Among stimuli-responsive materials, aqueous poly(*N*-isoproylacrylamide) (PNIPAm) nanogels are a prominently investigated and fascinating system with a reversible volume phase transition at a so-called lower critical solution temperature (LCST) of 32°C. Below this threshold temperature the nanogel particles are swollen with water due to hydrophilic interaction whereas above the LCST the polymer network is hydrophobic. The result is a collapse of the particle volume upon increase of the temperature [4, 10–12]. With this unique property PNIPAm nanogel particles are particularly interesting for investigation of the phase transition and dynamics in soft colloidal systems. Numerous predominantly light scattering studies exist on the structure and dynamics of PNIPAm hydrogels and micro- or nanogels in dilute suspensions [13–17]. However, investigations of dynamics in the technologically interesting dense-packed state, in which the samples are opaque are not accessible to visible light scattering methods due to multiple scattering. The utilisation of coherent X-rays from third generation storage ring sources enables to obtain information from both dilute and dense-packed colloidal systems. Therein, the use of a core-shell system, composed of a solid core, *e.g.* silica, and a PNIPAm shell increases the radiation damage threshold compared to a pure PNIPAm system [18]. Since their discovery, X-

rays were developed into a valuable tool for the investigation of condensed matter. X-ray scattering, or diffraction, reveals insight in the molecular and atomic structure of crystals, which has fascinated scientists throughout the first half of the 20th century and beyond. For the first time information about the differences of materials, the size of atoms, and the length and types of chemical bonds could be identified [19, 20]. While crystalline matter with long-range structural order has been studied extensively, in recent times the interest in the field of soft matter increased comprising fluids, polymers, self-organised suspensions, colloidal particles, and complex mixtures among others [21]. The compounds of such super-molecular and colloidal arrays in soft matter systems are more complex than crystals in terms of order and disorder but nevertheless can be dense and have strong spatial correlations [1].

The studies in this thesis shed light on the structure and dynamics of dense-packed silica-PNIPAm core-shell systems. The static and dynamic behaviour is accessed by dynamic light scattering, small-angle X-ray scattering (SAXS) and X-ray photon correlation spectroscopy (XPCS). Intensity correlation functions from silica-PNIPAm nanogels at various concentrations and with different PNIPAm shell thicknesses provide information about dynamic anomalies upon heating and cooling. Paired with the latest detector generation, time scales down to less than a millisecond can be reached which is in accordance with the dynamics of a single particle on the length scale of about its particle size [22, 23]. These results enable the determination of the full phase diagram of silica-PNIPAm particles spanning from dilute suspensions to an effective volume fraction of more than ninety percent, and covers the full relevant temperature range around the LCST.

The outline of the thesis is as follows: A general overview of colloidal systems is given and different forms of inter-particle interactions are discussed (▷ Chapter 2). Here, emphasis has been put on colloidal PNIPAm nanogels and silica-PNIPAm core-shell systems. The probing methods SAXS and XPCS are explained with the theoretical background relevant for this thesis (▷ Chapter 3). Subsequently, the silica-PNIPAm core-shell particle synthesis is reported and experimental details are given (▷ Chapter 4). The following experimental results (▷ Chapter 5) are separated in a discussion of the static (SAXS) and the dynamic (XPCS) behaviour of the samples. A phase diagram of silica-PNIPAm as a function of temperature and concentration is presented. Finally, the results are summarized and an outlook is given (▷ Chapter 6).

2 Colloidal Systems

Colloidal systems are in general particles evenly distributed in a dispersion medium such as water. The colloids themselves are defined as objects with at least one dimension in the range of 1 nm to 1 µm. The size is too small to be visible to the eye but at the same time much larger than atomic dimension. Thus, the overall system is a macro liquid, often referred to as complex liquid, consisting of particles which can have various shapes, dispersed in a suspending molecular liquid [24]. Examples for such two-phase systems are known from daily life: Paints and inks are small color pigments in a solvent, blood consists of cells in water, and much more besides.

The interparticle interactions between the colloidal particles are qualitatively comparable to the interaction of atoms and molecules in molecular fluids and solids [2, 25]. This property and their various forms of self-organisation make colloids scientifically highly interesting model systems for the investigation of the phase behaviour in liquids and solids.

With different polarisabilities of the particle bulk material and the solvent, two colloidal particles experience van-der-Waals attraction [24,26,27]. For homogeneous spherical particles with radius R and a center-to-center distance r this results in the interaction potential

$$V_A(r) = -\frac{H}{6}\left[\frac{2R^2}{r^2-4R^2} + \frac{2R^2}{r^2} + \ln\left(1-\frac{4R^2}{r^2}\right)\right] \quad , \tag{2.1}$$

where H is the Hamaker constant, depending on the polarisability of the atoms [26]. With only van-der-Waals attraction, the colloidal particles would coagulate irreversibly and precipitate in large clusters. To prevent agglomerations the particles have to be stabilized. This can be achieved by introducing a repelling force, typically via either steric or electrostatic stabilization.

2.1 Steric stabilization

Simplified, for steric stabilization the particles are coated with short ligands as illustrated in Fig. 2.1. If two particles approach each other, the ligands interpenetrate or compress before the particle surfaces can touch, which leads to entropic repulsion. In a stabilized system the repulsive force must be larger than the van-der-Waals attraction. A typical model system for this short-range repulsive interaction is the pairwise hard-sphere potential. The effective pair potential $V_{\mathrm{HS}}(r)$ for two particles with radius R and a center-to-center distance r can be written as

$$V_{\mathrm{HS}}(r) = \begin{cases} \infty & \text{for} \quad r \leq 2R \\ 0 & \text{for} \quad r > 2R \end{cases} \quad , \tag{2.2}$$

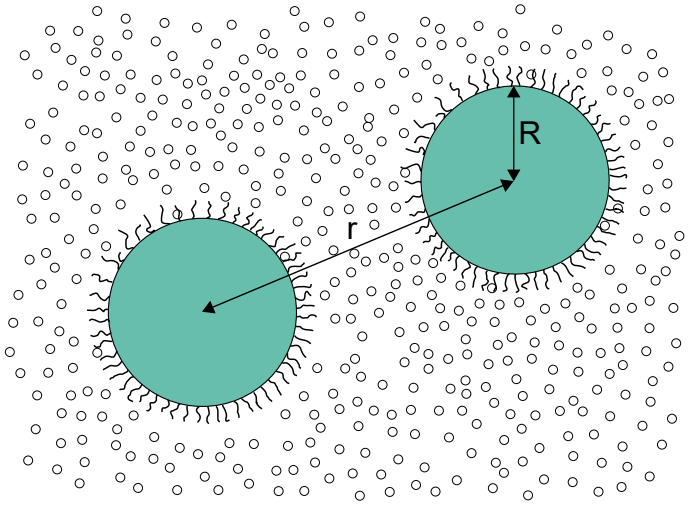

Figure 2.1: Illustration of a sterically stabilised hard-sphere suspension: Spherical colloids (large circles) with polymer brushes in solvent (small circles).

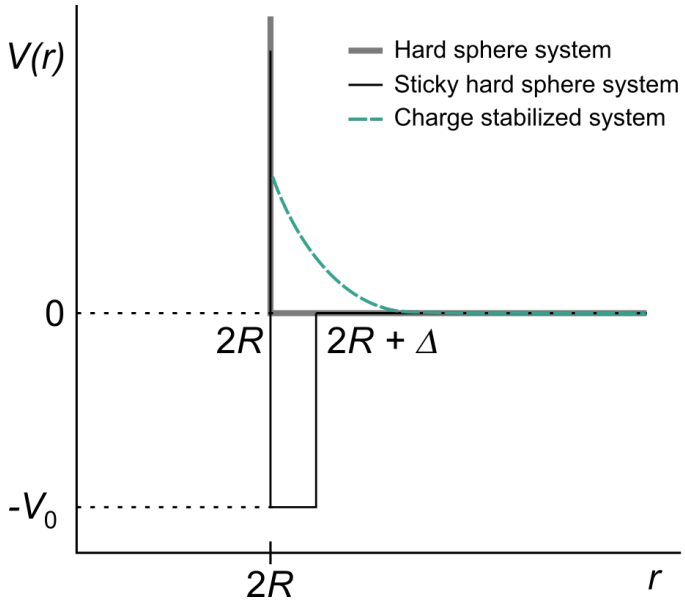

Figure 2.2: Illustration of a hard-sphere potential, a square-well potential with depth $-V_0$ and well width Δ for a sticky hard-sphere system and a potential for a charge-stabilized system as a function of core-to-core distance. $2R$ represents the particle diameter.

and is shown in Fig. 2.2. In a hard-sphere system with N particles in the volume V all structural correlations and hence the phase behaviour depend only on the volume fraction Φ, with

$$\Phi = \frac{4}{3}\pi R^3 \frac{N}{V} \quad , \tag{2.3}$$

where N/V denotes the particle number density. With increasing Φ the system passes through the phase diagram (Fig. 2.3) where Φ can vary between 0 and the close packing of spheres with $\Phi_{\mathrm{dp}} = 0.741$. For $\Phi < 0.494$ the system is liquid while it is found to be fully crystalline for $\Phi > 0.545$ [24, 28, 29]. Above $\Phi \approx 0.58$ a hard sphere system can form a glassy state.

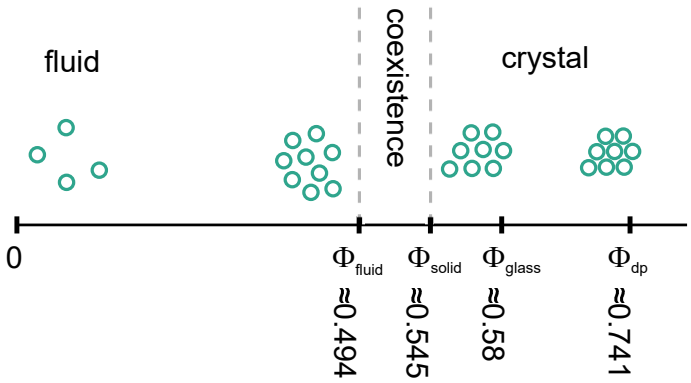

Figure 2.3: Phase diagram of a hard sphere system as a function of Φ (replicated from [35]).

For a system of hard spheres with surface adhesion the potential consists of a hard core combined with a deep and narrow rectangular attractive surface potential V_{SHS} as shown in Fig. 2.2 [30, 31]. This system has been addressed as sticky hard-sphere model (SHSM) and is applied to describe particle systems with very short-ranged, attractive potentials. The potential V_{SHS} is related to the stickiness parameter s which is inversely proportional to the strength of the attractive interaction and defined via the depth of the square well $-V_0$ and the width of the well Δ [31, 32] via

$$s = \frac{2R + \Delta}{12\Delta} \exp\left(-\frac{V_0}{k_B T}\right) \quad . \tag{2.4}$$

This leads to the SHSM interaction potential

$$V_{\mathrm{SHS}}(r) = \begin{cases} \infty & \text{for} \quad r < 2R \\ -V_0 & \text{for} \quad 2R \leq r \leq 2R + \Delta \\ 0 & \text{for} \quad r > 2R + \Delta \end{cases} \quad , \tag{2.5}$$

which is illustrated in Fig. 2.2. Eq. 2.5 shows that for large stickiness parameters s the well width goes to the limit $\Delta \to 0$. Consequently, $-V_0$ vanishes and the interaction potential becomes hard-sphere like. The phase behaviour of a sticky hard-sphere system depends on the volume fraction and the stickiness parameter and can be found in [33, 34].

2.2 Charge stabilization

A charge- or electrostatically-stabilized system consists of particles with surface radicals suspended in a polar solvent. Most of these ionisable surface groups detach into the solvent where they form a cloud of counterions around the particle, resulting in a diffuse electric double layer. Consequently, after dissociation of the charged surface groups, the particle itself is highly charged and therefore also called a macroion. Fig. 2.4 shows an illustration of a charge-stabilized system with macroions, counterions and solvent.

The encounter of the electric double layers of two approaching macroions leads to a repulsive force, which is usually larger than the van der Waals attraction and hence stabilizes

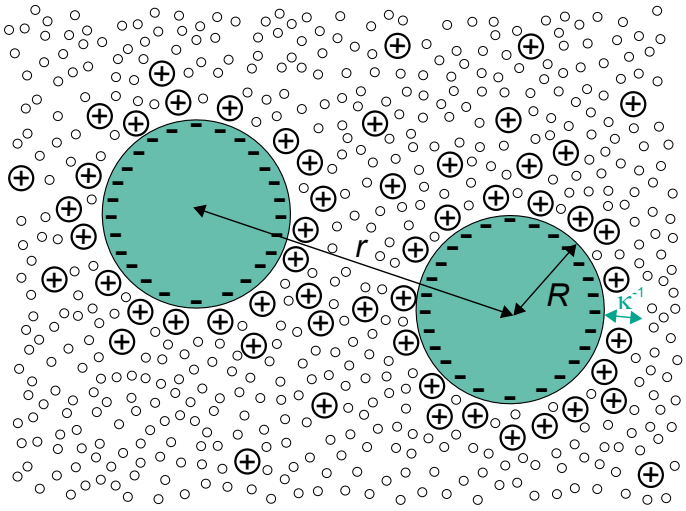

Figure 2.4: Illustration of an electrostatically stabilized suspension with macroions (large circles) and counterions (mid-size circles, marked with "⊕") in a solvent (small circles).

the colloidal system. The macroions are shielded by the counterions. This shielding can be tuned with the addition of salt, leading to additional co-ions in the solvent. The theoretical description of a charge-stabilized system is more complex than for hard spheres. A detailed expression for an effective pair potential has been given by Derjaguin, Landau, Verwey and Overbeek (DLVO-theory) and consists of an electrostatic and a van der Waals contribution [36]. For the effective DLVO potential, the three-component system has been reduced to a one-component system where the nature of the solvent is neglected irrespective of the dielectric constant ϵ. The electrostatic part can be described between two isolated particles by the Yukawa (also screened Coulomb or screened Debye-Hückel) potential [24, 37–39]

$$\frac{V_{\mathrm{CS}}}{k_B T}(r) = \begin{cases} \infty & \text{for} \quad r \leq 2R \\ \frac{e_0^2 Z_{\mathrm{eff}}^2}{\epsilon k_B T} \left(\frac{\exp(\kappa R)}{1+\kappa R} \right)^2 \frac{\exp(-\kappa r)}{r} & \text{for} \quad r > 2R \end{cases} . \tag{2.6}$$

Here, k_B is the Boltzmann constant, T is the absolute temperature, e_0 is the elementary charge, r is the center-to-center distance, Z_{eff} is the effective charge of the macroion in units of the elementary charge e_0, ϵ is the permittivity of the surrounding medium and R is the particle radius. ϵ is given by $\epsilon = \epsilon_0 \epsilon_r$ as the product of the permittivity of the vacuum ϵ_0 and the permittivity of the medium ϵ_r. The parameter κ^{-1} denotes the Debye-Hückel screening length, defined by

$$\kappa^2 = \frac{4\pi \rho_c (q e_0)^2}{\epsilon k_B T} , \tag{2.7}$$

with the mean counterion number density ρ_c and their charge $q e_0$. In the limit $\kappa R \to 0$ the Yukawa potential increases, leading to strong repulsion. For $\kappa R \to \infty$ the system becomes hard-sphere like with increasingly screened interactions as shown in Fig. 2.2. Compared to the hard-sphere potential the charge-stabilized interaction potential is long-ranged. The phase behaviour of an electrostatically-stabilized system depends on the volume fraction

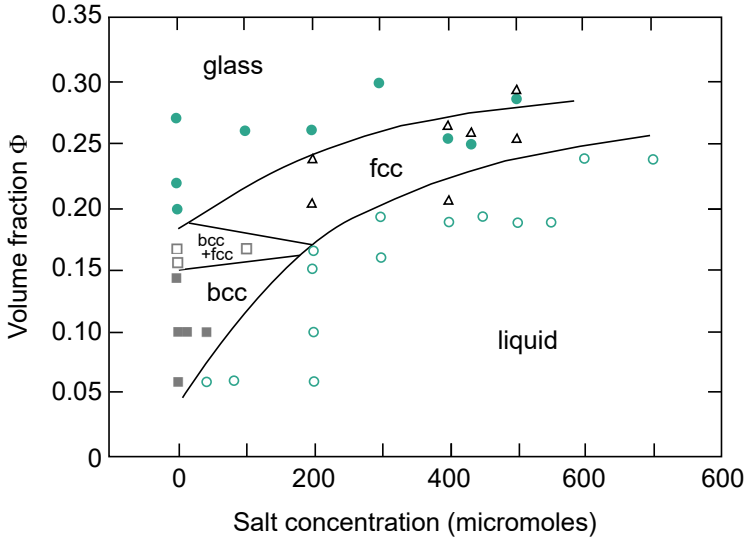

Figure 2.5: Phase diagram of a charge stabilized colloidal system with variation of volume fraction Φ and salt (HCl) concentration. The system shows a liquid phase (open circles), a bcc crystal (solid squares), an fcc crystal (open triangles), a fcc+bcc coexistence phase (open squares) and a glass phase (solid circles) (phase diagram replicated from [40]).

and the surface charge. The long-range electrostatic interaction leads to ordering in the system even at low Φ as demonstrated exemplary in Fig. 2.5 [40]. The phase diagram is shown for a charged-stabilized colloidal system as a function of volume fraction and salt concentration. For a constant salt concentration the system undergoes a transition from a liquid over a crystalline to a glassy phase with increasing Φ. In contrast, for a medium volume fraction as $\Phi \approx 0.2$ the order in the system changes from a glass to a crystal and further to a liquid with increasing salt concentration and hence screened interactions. Thus, for high salt concentrations the system is comparable to a hard-sphere system.

2.3 Colloidal nanogels

A colloidal nanogel is a colloidal system with nanometer-sized crosslinked polymer particles (for micrometer-sized particles often also referred to as microgel) that reversibly respond to external stimuli by changing their volume. The response can be connected to a variation of temperature, pH value, electrolyte concentration, hydrostatic or external pressure [3, 41]. The phase behaviour of such nanogels depends on both colloidal and material properties and is found to be between a hard-sphere and an ultra-soft colloidal system [8,42] whereas, depending on the conditions, they can behave like either of them. Among the stimulus-responsive systems the temperature-sensitive systems have been of great interest in the last decades. However, the exact interaction between nanogel particles and their phase behaviour covering the whole temperature regime is not yet understood in detail [3, 8].

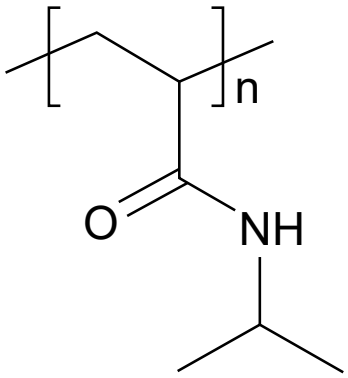

Figure 2.6: Molecular structure of poly(N-isopropylacrylamide) (PNIPAm) with the repeating unit n.

2.3.1 Poly(N-isopropylacrylamide)

A prominent and frequently studied example for a thermo-responsive polymer is poly(N-isopropylacrylamide) (PNIPAm) (Fig. 2.6). The polymer network shows a reversible volume phase transition at a lower critical solution temperature (LCST) of 32°C. The system changes from hydrophilic, where water molecules are bound to the polymer network, to hydrophobic where the water is expelled [3] and the polymer chains undergo a so-called coil-to-globule transition.

Colloidal PNIPAm nanogel consists of particles composed of cross-linked PNIPAm hydrogel in water. For PNIPAm particles the volume phase transition leads to a change of particle size with temperature variations ±20°C around the LCST. At temperatures below the LCST where the polymer network is hydrophilic the particles are swollen with water. With raising temperature above the LCST the polymer becomes hydrophibic and the volume decreases as illustrated in Fig. 2.7 due to deterioration of the solvent. Consequently the particle stiffness increases significantly [4, 10–12]. In a traditional colloidal suspension it is difficult to directly control the phase behaviour by external stimuli, as they are mostly induced by variation of the volume fraction which requires many different samples or a complex sample environment [3, 43]. For PNIPAm nanogels, the effective volume fraction and interaction potential can be varied with temperature, whereas the weight fraction and particle number density remains constant. With this unique property PNIPAm enables the study of the particle size and the phase behaviour of a soft colloidal system *in situ*. Particularly for studies on the phase behaviour of dense-packed jammed systems and disordered gel-phase PNIPAm nanogels are model systems of great interest.

With a typically low surface charge resulting from the initiator molecules of the synthesis, the particles interact via electrostatic interaction for interparticle distances larger than the particle diameter $2R$ [3, 41]. However, due to their softness, the nanogel particles can deform, interpenetrate and for very high concentrations even be compressed which allows effective volume fractions larger than one [44–46] and thus above the close packing limit of hard spheres ($\Phi \approx 0.74$, see Fig.2.3) [47]. For such dense- or over-packed systems at temperatures $T <$ LCST the interaction potential was found to be dominated by short-ranged, elastic repulsion [3, 48]. It has been described using a Hertzian potential

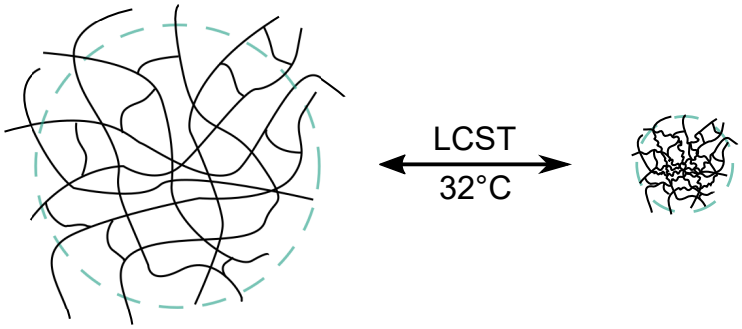

Figure 2.7: Schematic illustration of PNIPAm nanogel particles, in the swollen state for $T <$ LCST (left) and collapsed for $T >$ LCST (right). The black lines represent the PNIPAm network, the dashed line indicates the effective particle size.

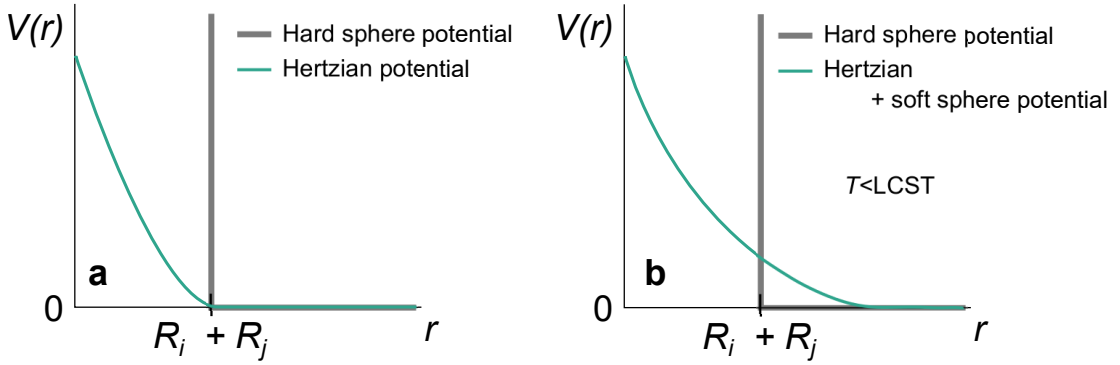

Figure 2.8: Illustration of a) Hertzian particle interaction potential of deformable interpenetrating nanogel particles in comparison with a hard-sphere potential as a function of core-to-core distance r. $R_i + R_j$ represents the overlap threshold. b) Possible particle interaction potential for colloidal PNIPAm nanogel particles. The potential consists of a Hertzian potential for $r < R_i + R_j$ and a soft repulsive potential for $r > R_i + R_j$.

which originally explains the change of elastic energy of two deformable compressed or interpenetrating objects with instantaneous radii R_i and R_j and center-to-center distance r [47, 49–51] via

$$V_{\mathrm{H}}(r) = \begin{cases} a\left(\frac{1-r}{R_i+R_j}\right)^{5/2} & \text{for} \quad r < R_i + R_j \\ 0 & \text{for} \quad r \geq R_i + R_j \end{cases} \quad . \tag{2.8}$$

Here, a is the Hertz pair potential amplitude

$$a = \frac{4Y\nu}{5\pi\left(1-\nu^2\right)} \quad , \tag{2.9}$$

which depends on the elastic properties of the nanogel with the Young's modulus Y and the Poisson ratio ν. The potential decreases as a power law with exponent 5/2 and becomes hard-sphere like at the overlapping threshold $r = R_i + R_j$ [47, 51] as illustrated in Fig. 2.8a. The phase behaviour of a Hertzian system with N particles is determined by the particle volume fraction and a. In combination with the soft repulsion for $r > R_i + R_j$ the combined potential for swollen PNIPAm nanogels ($T <$ LCST) is shown in Fig. 2.8b.

The phase behaviour of such soft particles at a constant temperature $T <$ LCST can be

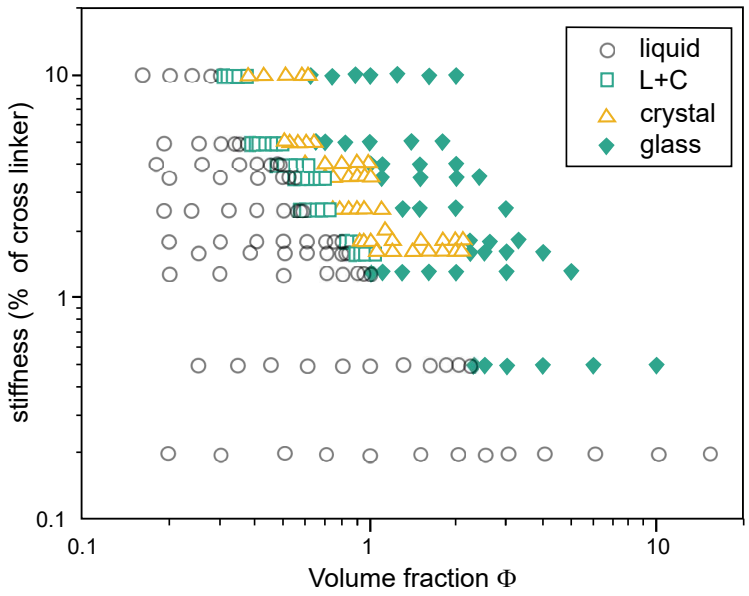

Figure 2.9: Phase diagram of colloidal PNIPAm suspensions of varying stiffness and volume fraction Φ obtained by oscillatory rheology (phase diagram replicated from [52]).

affected by variations in the particle synthesis regarding for instance the initial particle stiffness. By only varying the particle stiffness and the particle concentration at a constant temperature $T <$ LCST a system of colloidal PNIPAm exhibits a liquid, a crystalline, a liquid-crystal coexistence and a glassy phase (Fig. 2.9) which are the same phases found in hard-sphere systems at different volume fractions [52]. Here, the stiffness is indicated by the percentage of cross-linker content (in the range 0.2–10 wt%) and the particle concentration is defined via the volume fraction Φ. For low stiffness only a liquid phase was observed. It is explained that those very soft particles have too many internal degrees of freedom to form a solid phase. At low volume fractions the system also only shows a liquid phase irrespective of the stiffness. At large Φ and high stiffness the phase of the system is a glass, whereas for medium Φ and medium to high stiffness a crystalline phase and a liquid-crystal coexistence phase were found.

For $T >$ LCST, the interparticle potential is found to change to an attractive interaction between the collapsed PNIPAm particles. This can lead to aggregates without long-range order and strongly interpenetrating particles for highly concentrated samples [8, 48] due to a combination of van der Waals interactions and hydrophobic effects [3]. Thus the increase of temperature leads to a completely different interaction potential. Consequently, the phase behaviour can be tuned with both the temperature and the (external) variation of the volume fraction and different potentials have to be taken into account for a PNIPAm phase diagram covering a broad range of volume fractions and temperatures.

2.3.2 Effects of co-solvents on PNIPAm systems

Various experimental and theoretical work has shown that the addition of co-solvents to the solution affect the LCST of PNIPAm [53–58]. Co-solvents can be ethanol, sodium salts, urea or trimethylamine *N*-oxide ($(CH_3)_3NO$, TMAO) among others. TMAO is a biological

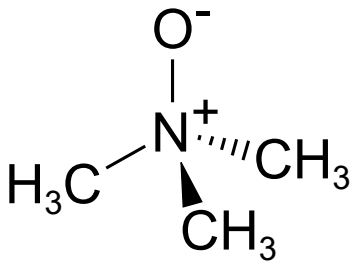

Figure 2.10: Molecular structure of trimethylamine *N*-oxide (TMAO).

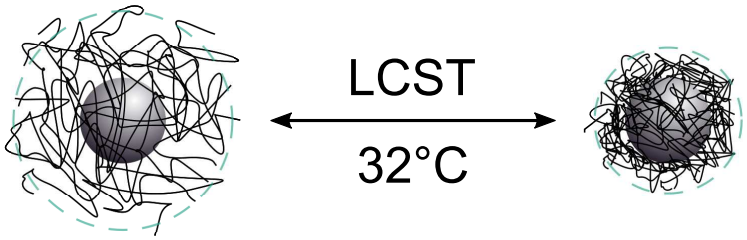

Figure 2.11: Schematic illustration of silica-PNIPAm particles and their temperature-induced change of size, *i.e.* the swollen state for $T <$ LCST (left) and the collapsed state for $T >$ LCST (right). The grey circles in the middle represent the silica cores and the black lines the cross-linked PNIPAm network. The dashed line indicates the effective particle size.

stabilizing osmolyte, known as a powerful protein protectant [59, 60]. The addition of TMAO to an aqueous PNIPAm suspension was found to stabilize the collapsed state and shift the LCST to lower temperatures with increasing TMAO concentrations [53, 55]. With three methyl groups (Fig. 2.10) and the ability to form hydrogen bonds, TMAO molecules have a preferred interaction with water which reduces the number of hydrogen bonds between polymer and water molecules [54,55]. The interaction between TMAO and PNIPAm was found to be a repulsive van-der-Waal interaction [53]. Those results about the influence of TMAO on the thermo-responsive character of PNIPAm was studied in dilute suspensions. However, little is known about the effect of TMAO on interparticle interaction in concentrated suspensions where inter-nanogel interactions are present.

2.3.3 Core-Shell structured PNIPAm nanogels

Thermoresponsive core-shell particles are systems of increasing interest. They can be divided into particles with either a polymerized nanogel shell on a solid core or core and shell composed of different hydrogels [7]. In the framework of this thesis, only the case of a solid core with a thermoresponsive shell is discussed. Such systems are used to precisely control the interparticle spacings *in situ* with temperature which is a key goal in colloidal science. The encapsulation of a core in the nanogel particle provides many mechanical advantages without influencing the thermal response of the nanogel [61, 62].

Thus, with a temperature increase above the LCST the shell of the particle collapses and the volume of the particle changes analogously to the pure nanogel particle (Fig. 2.11). A convenient core material is silica, since the synthesis is well-known and the particles need no stabilizing agents to prevent aggregation [63].

For a comprehensive understanding of the phase behaviour of a colloidal nanogel, complementary 3D information about both structure and dynamics up to large concentrations is essential with covering of the entire interesting temperature range around the LCST. Novel X-ray scattering methods allow studying structure and dynamics simultaneously from dilute to concentrated systems. Here, the encapsulation of a solid core in the nanogel particle provides a scattering object since for X-rays the scattering contrast between polymer and water is low.

3 Scattering Methods

X-rays have been established as a valuable tool to probe the structure of matter. In the first half of the 20th century, X-ray crystallography fascinated scientists by revealing insight about the atomic structure of crystals and hence the structural differences of materials, the size of atoms and the length and types of chemical bonds [19,20]. While crystalline matter with long-range structural order has been studied extensively, in recent times the interest in the field of soft matter increased, where the compounds are more complex regarding order and disorder. With high-brilliance third-generation synchrotron light sources and the development of high frame-rate detectors, X-ray scattering has developed from a static to a dynamic technique [64]. The access to coherent X-rays enables the study of dynamics of a disordered system on shorter time- and length-scales than accessible with other methods [65]. The main sources for this chapter are *Basic X-ray Scattering for Soft Matter* by Wim de Jeu [19] and *Elements of Modern X-ray Physics* by Jens Als-Nielsen and Des McMorrow [20].

3.1 The interaction of X-rays with matter

X-rays are electromagnetic radiation whose energy is given by $E = hc/\lambda$, where h is Planck's constant, c is the speed of light and λ the wavelength. The wavelengths of X-rays are in the region of $0.1\,\text{Å} \lesssim \lambda \lesssim 100\,\text{Å}$ which covers the length scale of inter-atomic distances ($1\,\text{Å} = 10^{-10}\,\text{m}$). The penetration of matter by X-ray photons can, depending on the energy, lead to interaction with the atom via absorption or scattering.

In the scattering process, the incoming X-ray wave interacts with electrons of the atoms in the sample material and is scattered. The oscillating electromagnetic field of the incoming wave stimulates oscillatory motion of the electron around its origin in the plane of the incoming field. Within this process, the accelerated charge functions as an X-ray source emitting a wave with the same wavelength as the incoming wave. With no energy transfer and hence no change of wavelength during the scattering process the scattering is

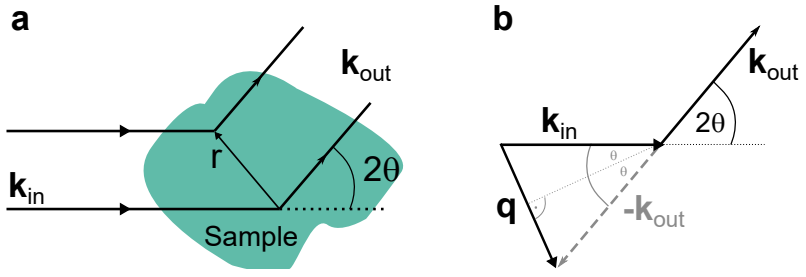

Figure 3.1: a) Schematic representation of an elastic scattering event ($|\mathbf{k}_{\text{in}}| = |\mathbf{k}_{\text{out}}| = k = 2\pi/\lambda$). b) Wave vector diagram.

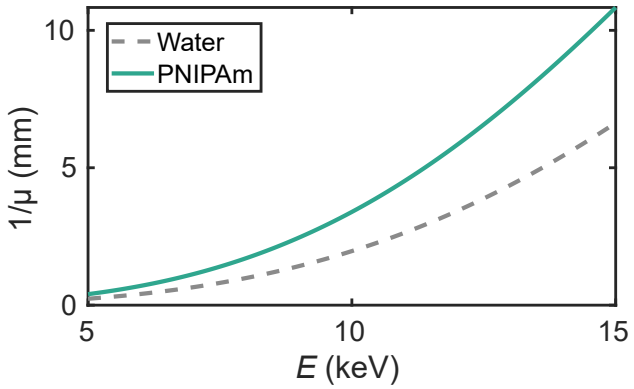

Figure 3.2: X-ray attenuation length $1/\mu$ for water and PNIPAm plotted for photon energies between 5 and 15 keV.

elastic. In the following only elastic scattering is considered. Inelastic scattering involving a change of energy is not discussed in the framework of this thesis.

The electromagnetic wave $E(r,t)$ propagates in a direction, which is defined by the wave vector $\mathbf{k}$:

$$E(r,t) = E_0 \exp\left[i(\mathbf{k}\cdot\mathbf{r} - \omega t)\right] \quad . \tag{3.1}$$

Here E_0 is the amplitude of the electric field and ω the frequency of the incoming wave. For reasons of simplicity the magnetic field is not included here. Fig. 3.1a shows a schematic representation of a typical elastic scattering event where the incoming wave is defined by $\mathbf{k}_{\text{in}}$ and the outgoing wave by $\mathbf{k}_{\text{out}}$. The angle 2θ is the scattering angle between $\mathbf{k}_{\text{in}}$ and $\mathbf{k}_{\text{out}}$. The vector diagram for an elastic scattering event through the angle 2θ defines $\mathbf{q} = \mathbf{k}_{\text{in}} - \mathbf{k}_{\text{out}}$ (Fig. 3.1b). With $|\mathbf{k}_{\text{in}}| = |\mathbf{k}_{\text{out}}| = k = 2\pi/\lambda$ this leads to

$$q = |\mathbf{q}| = 2k\sin\theta = \frac{4\pi}{\lambda}\sin\theta \quad . \tag{3.2}$$

Here, $\mathbf{q}$ is called wavevector transfer or scattering vector.

In an absorption process, the excess energy of the incoming photon is transferred to an electron of the atom which can be expelled and lead to ionization of the atom. The incoming intensity of an X-ray beam passing through sample material decreases exponentially with the penetration depth z. Defining I_0 as the initial intensity $I(z=0) = I_0$ the attenuated intensity becomes

$$I(z) = I_0 \exp(-\mu z) \quad . \tag{3.3}$$

Here, μ is the linear absorption coefficient whereas $1/\mu$ is the attenuation length. At this penetration depth, the initial intensity I_0 drops by the factor of 1/e. The absorption coefficient and therewith the attenuation length are material specific parameters and vary for different photon energies (see Fig. 3.2). For a small-angle X-ray scattering experiment in transmission geometry therefore an optimum sample thickness d_{opt} is required compromising between a large sample volume for high scattering and a thin sample to minimize

the absorption. This optimum is typically reached with a sample thickness equal to the absorption length [19, 20]

$$d_{\text{opt}} = \frac{1}{\mu} \quad . \tag{3.4}$$

3.2 Small-angle X-ray scattering

For an assembly of electrons as in an atom, molecule or particle, the scattered field is a superposition of the secondary waves originating from all N implicated scattering centres. The resulting instantaneous scattered field can be seen as a plane wave front in the far field with the scattering amplitude

$$E(\mathbf{q}, t) = E_0 \sum_{n=1}^{N} F_n(\mathbf{q}) \exp\left(i\mathbf{q} \cdot \mathbf{r}_n - i\omega t\right) \quad , \tag{3.5}$$

where $F_n(\mathbf{q})$ is the scattering amplitude of the n-th scatterer at position $\mathbf{r}_n(t)$. The term $\exp\left(i\mathbf{q} \cdot \mathbf{r}_n(t)\right)$ denotes a phase factor related to the arrangement of the scatterers at time t. The scattered intensity $I(\mathbf{q}, t)$ in the far-field can be written as

$$I(\mathbf{q}, t) = |E(\mathbf{q}, t)|^2 \quad . \tag{3.6}$$

The scattering from an atom is described by the atomic form factor

$$f^{\text{atom}}(\mathbf{q}) = \int_{\text{atom}} \rho(\mathbf{r}) \mathrm{e}^{i\mathbf{q}\cdot\mathbf{r}} d\mathbf{r} \quad , \tag{3.7}$$

where $\rho(r)$ is the electron density of the atom. The contribution of a volume element $d\mathbf{r}$ at position $\mathbf{r}$ with electron density $\rho(\mathbf{r})$ to the scattered field is proportional to $\rho(\mathbf{r})d\mathbf{r}$ with a phase factor $\exp(i\mathbf{q} \cdot \mathbf{r})$. Eq. 3.7 reveals the atomic form factor as the Fourier transform of the electron charge density.

For an accumulation of atoms as in a molecule or particle Eq. 3.7 can be extended to the scattering amplitude

$$F^{\text{mol}}(\mathbf{q}) = \sum_j f_j^{\text{atom}}(\mathbf{q}) \mathrm{e}^{i\mathbf{q}\cdot\mathbf{r}_j} \quad . \tag{3.8}$$

3.2.1 Static scattering of single particles

To obtain the scattered intensity the amplitude $F(\mathbf{q})$ has to be multiplied by its complex conjugate $F^*(\mathbf{q})$. The scattered intensity $I(\mathbf{q})$ is given by

$$I(\mathbf{q}) = |F(\mathbf{q})|^2 = F(\mathbf{q})F(\mathbf{q})^* \quad . \tag{3.9}$$

For an assembly of N equal atoms or molecules, the scattered intensity may be expressed with $F(\mathbf{q})$ as the atomic or molecular form factor as

$$I(\mathbf{q}) = \sum_n F_n(\mathbf{q}) \mathrm{e}^{i\mathbf{q}\cdot\mathbf{r}_n} \sum_m F_m(\mathbf{q}) \mathrm{e}^{-i\mathbf{q}\cdot\mathbf{r}_m} = F(\mathbf{q})^2 \sum_n \sum_m \mathrm{e}^{i\mathbf{q}\cdot(\mathbf{r}_n - \mathbf{r}_m)} \quad . \tag{3.10}$$

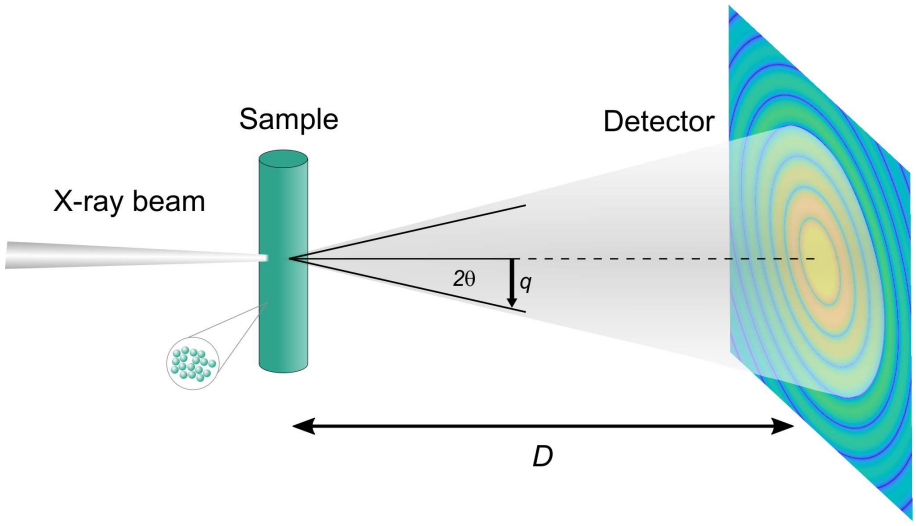

Figure 3.3: Schematic setup of a SAXS experiment in transmission geometry. A monochromatic X-ray beam is scattered by the sample in a capillary. The scattered intensity is detected by a 2D detector in the far-field with a sample-detector distance D.

Analogue to $\mathbf{k}$, $\mathbf{q}$ is connected to a length scale d in the system via $q = 2\pi/d$ which relates short distances as atomic distances to large $\mathbf{q}$ and vice versa. In a typical SAXS experiment particles in solution are quantified on the length scale around the particle size. To reveal information on this large length scale compared to the wavelength, access to small $\mathbf{q}$ is required. This is implemented by a large sample-detector distance D of usually several meters. Fig. 3.3 shows the schematic layout of a SAXS experiment in transmission geometry.

Assuming a homogeneous spherical particle with radius R and a constant electron density contrast $\Delta\rho$ ($\Delta\rho = \rho_S - \rho_0$, with the electron densities ρ_S of the particle and ρ_0 of the surrounding medium), the electron density is given by

$$\rho(\mathbf{r}) = \begin{cases} \Delta\rho, & |\mathbf{r}| < R \\ 0, & |\mathbf{r}| > R \end{cases} , \tag{3.11}$$

as a function of $\mathbf{r}$. With a spherical symmetric particle the electron density $\rho(\mathbf{r})$ depends only on $r = |\mathbf{r}|$. Consequently $F(\mathbf{q})$ becomes direction independent and depends only on $|\mathbf{q}| = q$. The particle scattering factor becomes a symmetric Fourier transform with

$$F(q) = \int_0^\infty 4\pi r^2 \rho(r) \langle \exp(i\mathbf{q} \cdot \mathbf{r}) \rangle dr. \tag{3.12}$$

Here $\langle \cdot \rangle$ denotes the spherical average over all orientations which allows the position vector $\mathbf{r}$ to be randomly orientated with regard to $\mathbf{q}$ as the case for many systems with spherical symmetry. The evaluation of the average of the phase factor is

$$\langle e^{i\mathbf{q}\cdot\mathbf{r}} \rangle = \frac{\sin(qr)}{qr} , \tag{3.13}$$

which leads to

$$F(q) = \int_0^\infty 4\pi r^2 \rho(r) \frac{\sin(qr)}{qr} dr \quad , \tag{3.14}$$

and consequently

$$F(q) = 3\Delta\rho V_P \left[\frac{\sin(qr) - qr\cos(qr)}{q^3 r^3} \right] = \Delta\rho V_P \Psi(qr) \quad . \tag{3.15}$$

Here V_P is the particle volume and the substitution $\Psi(x) = \frac{3\sin x - x \cdot \cos x}{x^3}$ introduces $\Psi(qr)$ as the form factor of a sphere. With Eq. 3.15, the scattered intensity of a dilute system consisting of N homogeneous spherical particles with radius R can be written as

$$I(q) = N\Delta\rho^2 V_P^2 |F(q)|^2 = 9N\Delta\rho^2 V_P^2 \left(\frac{\sin(qR) - qR\cos(qR)}{(qR)^2} \right)^2 \quad , \tag{3.16}$$

with the single particle form factor $P(q) = |F(q)|^2$ from Eq. 3.15.
The Equations 3.14-3.15 point out sinusoidal intensity oscillations with increasing q where the slope of the intensity with the here shown spherical form factor follows a q^{-4} dependence. Fig. 3.4a shows the calculated form factor for single spheres with $R = 50\,\text{nm}$ and $R = 150\,\text{nm}$. The position of the minima and maxima are related to the size of the particles. For the larger sphere the oscillations become narrower with a smaller Δq between two minima and the position of the first minimum shifts to a smaller q.
For a system of spherical core-shell particles the particle form factor consists of different contributions. The particle is composed of a spherical core with radius R_2 and electron density contrast $\Delta\rho_{\text{core}}$, and a shell with electron density contrast $\Delta\rho_{\text{shell}}$ leading to the total radius R_1. The core-shell form factor is composed as pictured in Fig. 3.5 and thus the intensity is calculated as

$$I^{\text{core-shell}}(q) = \Delta\rho_{\text{core}}^2 \left[V_1 \Delta\rho_{\text{shell}} \Psi(qR_1) - (\Delta\rho_{\text{shell}} - \Delta\rho_{\text{core}}) V_2 \Psi(qR_2) \right]^2 \quad , \tag{3.17}$$

with $\Psi(qR_{1,2})$ as the spherical form factor relating to the total size of the particle and only the core, respectively (see Eq. 3.15). Fig. 3.4b shows the calculated form factor for a spherical core-shell system with $R_1 = 150\,\text{nm}$ and $R_2 = 50\,\text{nm}$ and a lower electron density contrast of the shell compared to the core ($\Delta\rho_{\text{core}} > \Delta\rho_{\text{shell}}$). The first minimum is found at the same q as for the sphere with $R = 150\,\text{nm}$. However, other than the form factors of the simple spheres, the minima show different distances Δq with increasing q. The envelope of $P(q)$ still decays with a q^{-4} dependence but shows higher oscillations itself, relating to interferences of the intensity scattered by core and shell.

3.2.2 Scattering of disperse systems

In reality the size of the particles in a colloidal systems is distributed around an average value $\bar{R}$ with a size distribution $D(R)$, where $\int D(R)dR = 1$. This property is called dispersity. The size dispersity p of a colloidal system is typically described by the Schulz-

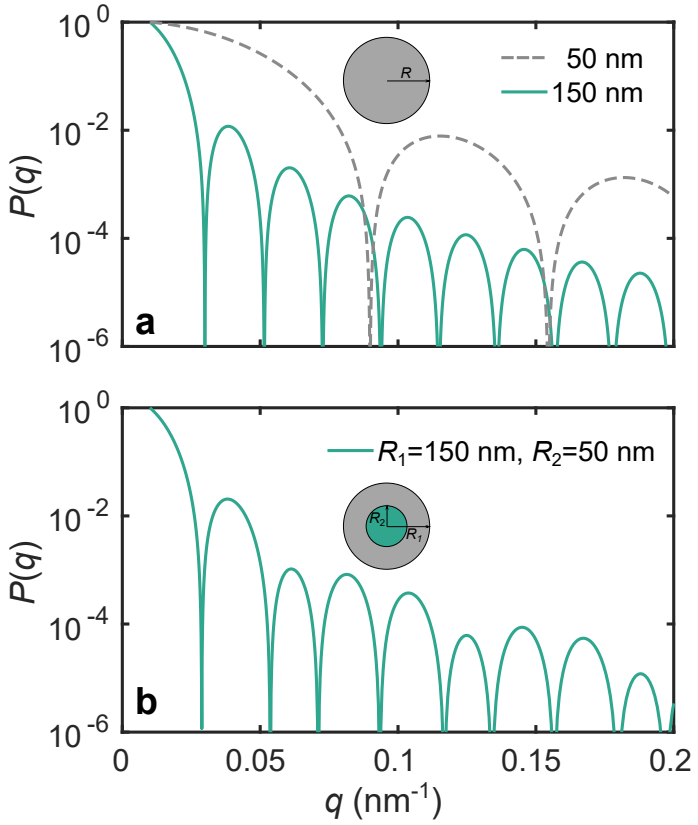

Figure 3.4: Calculated form factor $P(q)$ as a function of q for a) a sphere with $R = 150\,\mathrm{nm}$ und $R = 50\,\mathrm{nm}$ (Eq. 3.15) and b) a spherical core-shell system with $R_1 = 150\,\mathrm{nm}$ and $R_2 = 50\,\mathrm{nm}$ (Eq. 3.17) .

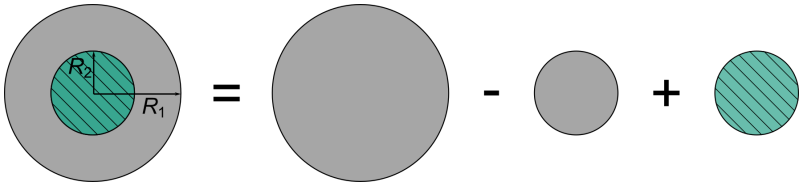

Figure 3.5: Schematic composition of the spherical core-shell form factor.

Zimm distribution [66–68]:

$$D(R, \bar{R}, z) = \frac{1}{(z+1)!}\left(\frac{z+1}{\bar{R}}\right)^{z+1} R^z \exp\left(-\frac{z+1}{\bar{R}}R\right) \quad . \tag{3.18}$$

The parameter z is a measure of the spread in particle sizes and connected to the dispersity p via

$$p = \frac{\Delta R}{\bar{R}} = \sqrt{\frac{1}{z+1}} \quad . \tag{3.19}$$

In the presence of dispersity, the particle form factor and hence the intensity defined in Eq. 3.16 has to be extended to

$$I(q) = \Delta\rho^2 \int_0^\infty D(R, \bar{R}, z) V_P(R)^2 P(q, R) dR \quad . \tag{3.20}$$

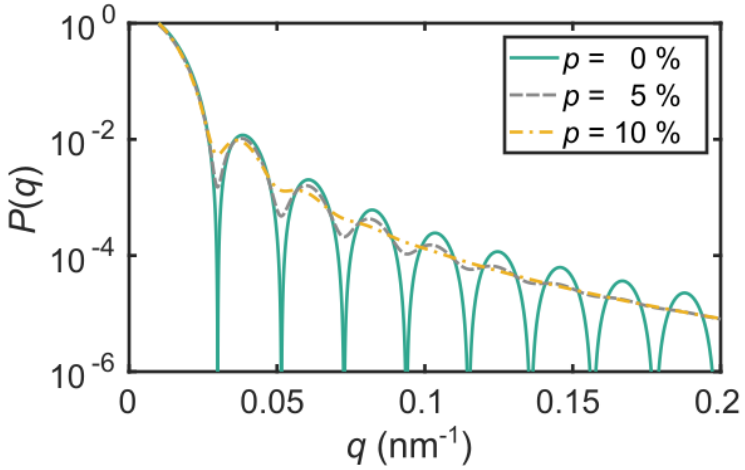

Figure 3.6: Calculated form factor for spherical particles with $\bar{R} = 150\,\text{nm}$ with different dispersities, following the Schulz-Zimm size distribution.

Fig. 3.6 shows the influence of dispersity on the form factor of a sphere. For increasing dispersity, the oscillations blur with regard to their amplitude, which is more pronounced at large q. Following Eq. 3.17 the intensity of a disperse core-shell system is given by

$$I^{\text{core-shell}}(q) = \Delta\rho_{\text{core}}^2 \left[\Delta\rho_{\text{shell}} \int_0^\infty D(R_1, \bar{R}_1, z_1) V_1(R_1) \Psi(qR_1) dR_1 - (\Delta\rho_{\text{shell}} - \Delta\rho_{\text{core}}) \int_0^\infty D(R_2, \bar{R}_2, z_2) V_2(R_2) \Psi(qR_2) dR_2 \right]^2 . \tag{3.21}$$

3.2.3 Scattering from systems with interparticle interactions

In a concentrated particle system where spatial interparticle correlations have to be taken into account the intensity is not sufficiently described by $|F(q)|^2$. Therefore, the static structure factor $S(q)$ is introduced which depends on the interaction potential in the system. The structure factor is connected to the radial distribution function $g(r)$ which describes the density variation in a system as a function of distance r from a chosen reference particle. It is defined by $g(r) = \rho(r)/\rho_a$ where ρ_a is the average areal number density.

For a concentrated system of volume V with N monodisperse particles the structure factor can be written as

$$S(q) = 1 + 4\pi \frac{N}{V} \int_0^\infty r^2 \left[g(r) - 1 \right] \frac{\sin qr}{qr} dr. \tag{3.22}$$

The scattering intensity in Eq. 3.16 is complemented by $S(q)$ to

$$I(q) = N \Delta\rho^2 V_P^2 P(q) S(q) \quad . \tag{3.23}$$

Considering the limiting values, Eq. 3.22 shows that for the limit $q \to \infty$ follows $S(q) \to 1$. For $q \to 0$ follows $\frac{\sin(qr)}{q} \to r$ and consequently the right hand side of Eq. 3.22 becomes proportional to $g(r) - 1$. Thus, $S(q)$ depends on density fluctuations in the system and

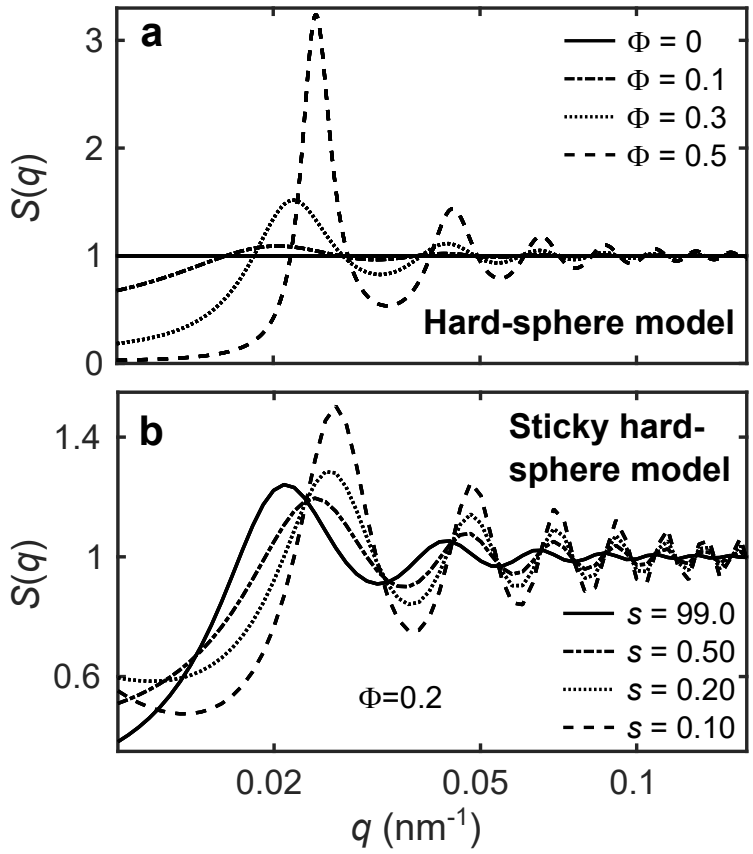

Figure 3.7: Evolution of the static structure factors for a) a hard sphere system with increasing volume fraction and b) a spherical core-shell system with sticky hard sphere potential at $\Phi = 0.2$ and decreasing stickiness parameter s.

approaches unity towards large q. Unlike crystals, the disordered particles in a colloidal system have no long-range order, so the intensity oscillations related to $S(q)$ are not sharp and decrease with increasing q.

The interaction potential and thus the structure factor vary for different colloidal systems. For a system of steric repulsive hard spheres with radius R, the particles are described by a model of impenetrable spheres whose minimal distance equals the center-to-center-distance $d = 2R$. For adhesive colloidal particles interacting via short-ranged attractive forces the sticky hard sphere model (SHSM) has become a common approach. The SHSM is a prominent model found for colloidal gels or glasses [30, 31, 69].

Fig. 3.7a shows the calculated structure factors of a hard sphere system with $R = 145\,\mathrm{nm}$ at different volume fractions Φ. For a very dilute suspension when $\Phi \to 0$, the structure factor equals unity ($S(q) = 1$). For higher concentrations, $S(q)$ shows oscillations with a pronounced first maximum at $q_{\max}$, related to the mean interparticle distance. With increasing volume fraction, the peak height increases and shifts to larger $q_{\max}$, suggesting decreased interparticle distances.

In Fig. 3.7b the $S(q)$ of a spherical sticky hard sphere core-shell system is shown for decreasing stickiness parameter s (Eq. 2.4). The variation of the stickiness parameter s, which characterizes the adhesive strength, affects the height and position of $S(q_{\max})$ as

well as the width. Smaller s means stronger attraction (see Eq. 2.4). Thus, with a large stickiness parameter of 99, $S(q)$ resembles the structure factor of a hard sphere system (see Fig. 3.7a). With stronger attraction $q_{\max}$ shifts to larger q. For $s < 0.5$ the width of the structure factor peak decreases while the height increases. The interparticle attraction further affects the $S(q)$ at $q \to 0$, where $S(q)$ increases for $q \to 0$, whereas it monotonously decreases for a repulsive hard-sphere system. The increase at $q \to 0$ is more pronounced for lower s and thus directly related to the stickiness in the system which can favour the formation of agglomerations.

3.3 X-ray photon correlation spectroscopy

If coherent light is scattered by a disordered system the result is a random interference pattern in the far-field, called "speckle" pattern. This diffraction pattern contains exact information about the configuration of the scatterers, e.g. the colloidal sample system. In an experiment with incoherent light this information would not be accessible because the diffraction pattern contains only information on the average spatial correlations in the sample. If the particles underlie a certain dynamics and thus the spatial arrangement of the scatterers changes with time, the speckle pattern changes as well. At a given point on the detector this can be observed as intensity fluctuations, directly related to the dynamics in the sample. This technique is called X-ray photon correlation spectroscopy (XPCS) and provides information about the sample dynamics by analysis of the temporal intensity correlations [65]. An XPCS experiment on colloidal systems is typically performed in SAXS geometry as illustrated in Fig. 3.8. The coherent X-ray beam is scattered in transmission through the sample. The scattered intensity is detected by a 2D detector in snapshots with a fixed time interval τ.

The electric field amplitude of a scattered coherent beam of electromagnetic radiation is

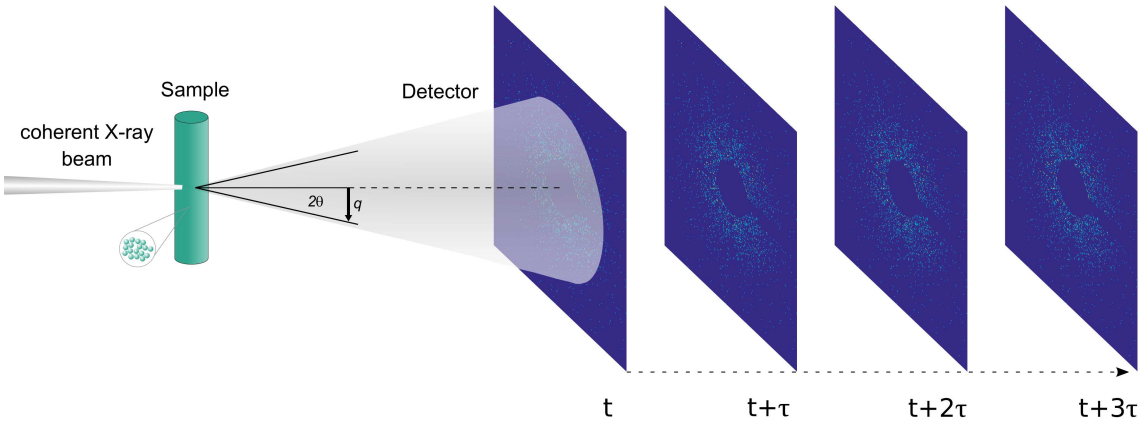

Figure 3.8: Schematic setup of an XPCS experiment. A coherent X-ray beam is scattered by the colloidal sample. The scattered intensity results in a speckle pattern in the far-field which is detected by a 2D detector with fixed time intervals τ.

given by

$$E(\mathbf{q},t) = E_0 \sum_{n=1}^{N} F_n(\mathbf{q}) \exp\left(i\mathbf{q}\cdot\mathbf{r}_n(t)\right) \quad . \tag{3.24}$$

Thus, the intensity in the far-field can be written as

$$I(\mathbf{q},t) = |E(\mathbf{q},t)|^2 = \left| E_0 \sum_{n=1}^{N} F_n(\mathbf{q}) \exp\left(i\mathbf{q}\cdot\mathbf{r}_n(t)\right) \right|^2 \quad , \tag{3.25}$$

with the scattering amplitude $F_n(\mathbf{q})$ of the n-th scatterer at position $\mathbf{r}_n(t)$.

To measure intensity correlations of the speckle patterns over time, the single speckles must be distinguished by the detector. Thus, the speckle size $\hat{s}$ should match or be larger than the pixel size of the detector $d_{\mathrm{pix}} \leq \hat{s}$. The speckle size is given by

$$\hat{s} \approx \frac{\lambda D}{L} \quad , \tag{3.26}$$

with the wavelength λ, the sample-detector distance D and L the lateral extension of the beam profile.

The fluctuating intensity is recorded by the detector in the far-field. It contains the information of dynamics of the colloidal system and can be quantified with the normalised second order intensity autocorrelation function $g_2(q,\tau)$:

$$g_2(q,\tau) = \frac{\langle I(q,t) I(q,t+\tau)\rangle}{\langle I(q,t)\rangle^2} \quad , \tag{3.27}$$

where $\langle\cdot\rangle$ denotes the temporal average over all times t. $I(q,t)$ represents the intensity at a certain wave vector transfer q and time t. $I(q,t+\tau)$ is the intensity at the same q in average with a time delay τ.

For short times $\tau \to 0$, the intensity is correlated with $I(q,t)$ at time t. $\langle I(q,t)I(q,t+\tau)\rangle$ becomes

$$\lim_{\tau\to 0} \langle I(q,t) I(q,t+\tau)\rangle = \langle I^2\rangle \quad . \tag{3.28}$$

For large delay times τ, the correlation between $I(q,t)$ and $I(q,t+\tau)$ is zero. In this case $\langle I(q,t)I(q,t+\tau)\rangle$ yields

$$\lim_{\tau\to\infty} \langle I(q,t) I(q,t+\tau)\rangle = \langle I(q,t)\rangle \langle I(q,t+\tau)\rangle = \langle I^2\rangle \quad . \tag{3.29}$$

The intensity hence drops from $\langle I^2\rangle$ at $t = 0$ to $\langle I\rangle^2$ for large times. The second order correlation function $g_2(q,\tau)$ can be expressed via the normalised intermediate scattering function $\mathrm{f}(q,\tau)$:

$$g_2(q,\tau) = 1 + \beta(q) \frac{\langle I(q,t) I^*(q,t+\tau)\rangle^2}{\langle I(q)^2} = 1 + \beta(q)\cdot |\mathrm{f}(q,\tau)|^2\rangle \quad , \tag{3.30}$$

where $\beta(q)$ is the speckle contrast depending on the coherence of the source [70] and the brackets $\langle\cdot\rangle$ denote an ensemble average. The second part of Eq. 3.30 is known as

Siegert-relation [70] which relates the g_2 function to the normalized intermediate scattering function $\mathrm{f}(q,\tau)$.

The normalized intermediate scattering function is defined by

$$\mathrm{f}(q,\tau) = \frac{F(q,\tau)}{F(q,0)} \quad , \tag{3.31}$$

where $F(q,\tau)$ is the intermediate scattering function, defined for N particles by

$$F(q,\tau) = \frac{1}{N}\sum_{n=1}^{N}\sum_{m=1}^{N}\langle\exp(i\boldsymbol{q}[\mathbf{r}_n(t)-\mathbf{r}_m(t+\tau)])\rangle \quad , \tag{3.32}$$

and $F(q,0)$ can be associated with the static structure factor $S(q)$.

3.3.1 Dynamics of colloidal suspensions

For many soft matter systems $\mathrm{f}(q,\tau)$ can be expressed with the Kohlrausch-Williams-Watts (KWW) function [71] as

$$\mathrm{f}(q,\tau) = \exp\left(-(\Gamma(q)\tau)^{\gamma}\right) \quad , \tag{3.33}$$

which leads to

$$g_2(q,\tau) = 1+\beta\cdot\exp\left[-2(\Gamma(q)\cdot\tau)^{\gamma}\right] \quad . \tag{3.34}$$

The KWW function (Eq. 3.33) contains information about the dynamics of the system [72] with the Kohlrausch exponent γ and the relaxation rate $\Gamma(q)$. The relaxation rate is directly related to the characteristic relaxation time τ_c via $\Gamma = \tau_\mathrm{c}^{-1}$. The characteristic relaxation time τ_c is specified as the time where the g_2 function has decayed to the value $1/\mathrm{e}^2$ which relates to the time where a spherical particle has roughly moved by the distance of its own size. For diffusive systems the decay of intermediate scattering function is exponential with $\gamma = 1$ and the relaxation rate is given by

$$\Gamma(q) = D_0\cdot q^2 \tag{3.35}$$

with the (Stokes-Einstein) diffusion constant D_0 [73]

$$D_0 = \frac{\mathrm{k_B}T}{6\pi\eta R} \tag{3.36}$$

with η as viscosity of the solvent and the hydrodynamic radius R_H of the diffusive particles. R_H can be determined from the intensity autocorrelation function via the Stokes-Einstein relation

$$R_\mathrm{H} = q^2\cdot\frac{k_\mathrm{B}T}{6\pi\eta\Gamma} \quad . \tag{3.37}$$

For non-diffusive dynamical processes this q dependence differs from the quadratic form and the decay of $\mathrm{f}(q,\tau)$ is typically non-exponential. Hence, τ_c as a function of q contains information about the respective underlying dynamics in the system which can be typically described by a power law $\tau_\mathrm{c}\propto q^p$. Simple Brownian particle motion where $\tau_\mathrm{c} = 1/Dq^2$

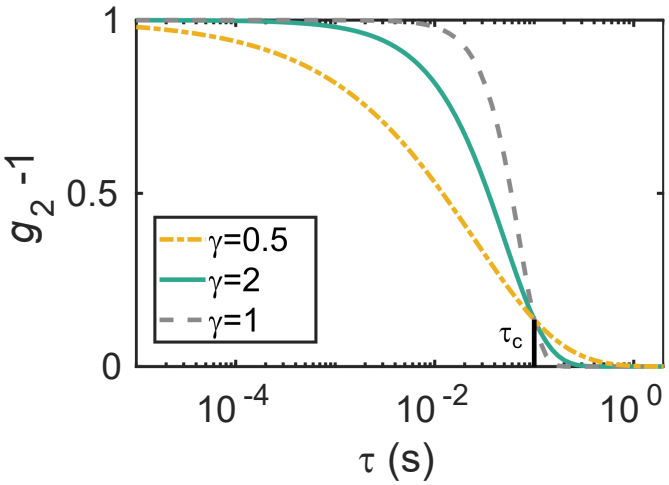

Figure 3.9: Calculated intensity autocorrelation function $g_2 - 1$ for different KWW exponents $\gamma = 1$, $\gamma = 2$ and $\gamma = 0.5$ all with the same characteristic relaxation time $\tau_c = 0.1\,\mathrm{s}$.

(Eq. 3.35) is connected to a linearly increasing mean-squared displacement $\langle \Delta r^2(t) \rangle \propto t^a$ with $a = 1$. A q dependency of τ_c with $p > 2$ leads to a mean-squared displacement with $a < 1$ which can be associated with sub-diffusive particle motion [74, 75]. Scalings of $\tau_c \propto q^{-3}$ and even $\tau_c \propto q^{-4}$ have been observed for colloids in a polymer matrix [74, 76] where the dynamics of the colloid is linked to the motion of the surrounding polymer chains. Polymer dynamics with q^{-3} dependence of τ_c have been interpreted as characteristics of membrane-like polymers following the Zimm model [77–80]. Additionally, the characteristic dynamics influence the slope of $g_2(q, \tau)$, quantified by the KWW exponent γ (see Fig.3.9). Sub-diffusive dynamics usually show a stretched and thus slower than exponential decay of the correlation function with a KWW exponent $\gamma < 1$ [74, 75, 81]. It further may indicate the presence of dynamical heterogeneities with the presence of multiple structural relaxation processes in the system [82].

On the contrary, a q dependency of τ_c with $p < 2$ together with a compressed exponential slope indicated by the KWW exponent $\gamma > 1$ is typically attributed to ballistic, hyper-diffusive motion [83,84]. Dynamics of this type are often reported for jammed non-diffusive soft materials such as colloidal gels, concentrated emulsions and glasses [83–91]. Transitions between different types of slopes indicates, e.g., the occurrence of heterogeneities and correlated motion as often seen in glass formers [92, 93].

4 Experimental Details

All sample systems studied in this thesis have been synthesised and characterised in-house. X-ray experiments have been performed at different coherence beamlines of third-generation storage ring sources.

4.1 Particle synthesis

To prepare colloidal silica-PNIPAm core-shell particles, silica (SiO_2) nanoparticles have been synthesized following the well-known Stöber synthesis [94]. The Stöber process is a sol-gel approach to obtain spherical monodisperse silica particles of a controllable size via hydrolysis of the precursor tetraethyl orthosilicate ($Si(OEt)_4$, TEOS) in ethanol with ammonia functioning as catalyst. For particles with radii in the range of $50-60$ nm 450 ml of non-denatured ethanol (95%, Sigma-Aldrich, Germany) are mixed with 20 ml ammonia solution (25%, Sigma-Aldrich, Germany) in a cone flask, equipped with a magnetic stirbar. Then 7.5 ml TEOS (Sigma-Aldrich, Germany) are added and stirred at room temperature for about 24 h. After expiration of this time the reaction has come to completion and the silica particles have grown to their final size. In the following step, with the aim of grafting the silica particles, the particle surface gets functionalized. Therefore, 2 ml 3-(Trimethoxysilyl)propyl methacrylate (TPM) is added together with 15 ml ammonia solution and the suspension has to be stirred for another 24 h. After the functionalization process the particle suspension is purified by evaporation of the ammonia using a rotary evaporator and subsequent dialysis against pure ethanol for approximately one week.

In the next step, following [62], the surface of the functionalized silica particles is grafted with PNIPAm. Firstly, the silica dispersion is filled in a round-bottom flask equipped with a magnetic stirrer whereas the flask is in an oil bath with adjustable temperature. Under stirring, about 0.38 g sodium dodecyl sulfate ($CH_3(CH_2)_{11}SO_4Na$, SDS) and 0.42 g sodium sulfite (Na_2SO_3) are added followed by 1500 ml of ultrapure water. To remove the oxygen, the dispersion is stirred for one hour at 60°C under a nitrogen stream. Afterwards, still under nitrogen, grains of ammonium iron(II) sulfate ($(NH_4)_2Fe(SO_4)_2$) are added as catalyst together with 0.4 g potassium peroxo persulfate ($K_2S_2O_8$) as oxidizing agent to enable the subsequent polymerization process at 60°C by forming a redox couple. In the next step, 5 g *N*-Isopropylacrylamide (NIPAm) and 0.22 g *N,N'*-Methylenebisacrylamide (MBAm) as the cross-linker have to be solved in 40 ml of ethanol. This monomer solution is slowly added in drops to the silica dispersion and stirred over night at 60°C. After expiration of this time, the reaction is completed and the suspension is filtered and dialysed for one week against ultrapure water to remove the SDS. To synthesize different shell sizes on silica particles from the same stock dispersion, the quantities of the cross-linker MBAm and the monomer NIPAm were varied while keeping the ratio towards each other constant.

4.2 Sample characterization and preparation

Overall, six different samples SP-1, SP-2A, SP-2B, SP-2C, SP-3A and SP-3B with varied core-to-shell ratio were studied in this thesis. After the synthesis, the particles were pre-characterized with transmission electron microscopy (TEM). Fig. 4.1 shows the TEM images for the pure silica cores of SP-2, the silica-PNIPAm particles of SP-2B and a close-up of a single particle of SP-2B. Since for the TEM characterization the particle suspension is in the dry state the values of particle or shell size do not provide the values the particles have dispersed in water.

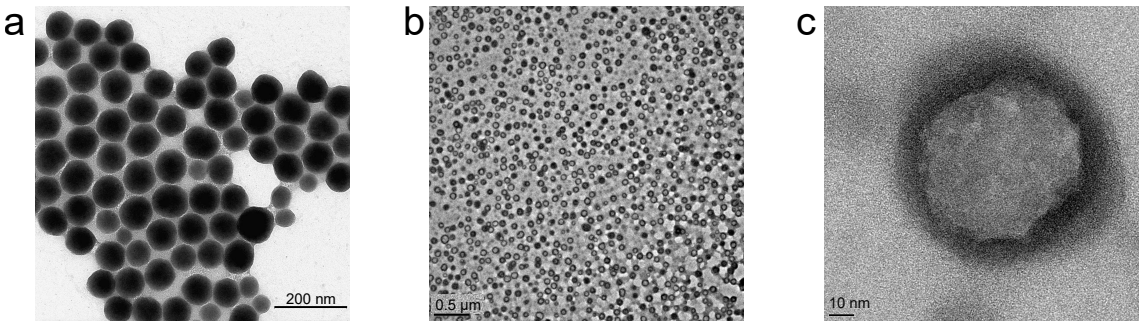

Figure 4.1: TEM images of a) uncoated silica particles of SP-2, b) silica-PNIPAm of SP-2B and c) a single silica-PNIPAm particle of SP-2B.

To verify that the PNIPAM grafting process was successful and to obtain the hydrodynamic radius R_{H} of the swollen and collapsed particles in water, all samples were characterized by dynamic light scattering (DLS) for temperatures between $T = 15°\mathrm{C}$ and $45°\mathrm{C}$ (see. section 5.4.2). A dilute suspension ($\Phi < 0.004$) was used for DLS. Table 4.1 shows all samples studied in this thesis whereas the radius of the swollen particles relates to $T = 20°\mathrm{C}$ and the radius of the collapsed particles to $T = 40°\mathrm{C}$, respectively. Sample SP-1 has a swollen PNIPAm shell of $d_{\text{SP-1}} \approx 35\,\mathrm{nm}$ on a silica core of $R_{\mathrm{H_{Si}}} = 50\,\mathrm{nm}$. For the second silica batch with $R_{\mathrm{H_{Si}}} = 54\,\mathrm{nm}$ three different layer thicknesses have been synthesized. The shells were varied between the samples SP-2A with $d_{\text{SP-2A}} \approx 20\,\mathrm{nm}$, SP-2B with $d_{\text{SP-2B}} \approx 75\,\mathrm{nm}$ and SP-2C with $d_{\text{SP-2C}} \approx 140\,\mathrm{nm}$ in the swollen state at 20°C. Together with the radius of the core $R_{\mathrm{H_{Si}}}$ and the width of the swollen shell d with $d = R_{\mathrm{H_{total}}} - R_{\mathrm{H_{Si}}}$, the particle "softness" ξ can be calculated via $\xi = d/R_{\mathrm{H_{Si}}}$ following Boles and Talapin [95, 96].

For the XPCS experiments the samples were concentrated. Therefore, a temperature adjustable Multivapor (Büchi, Swizerland) has been used. For the implementation to the experimental setup the sample solution was filled in borosilicate glass capillaries with diameters of $0.7 - 2\,\mathrm{mm}$, depending on the X-ray energy of the experiment. After filling the capillaries were vacuum-sealed by melting the top of the capillary with a flame and finally sealing it with hot glue.

By drying a small volume ($0.1 - 0.3\,\mathrm{ml}$) of each sample at approximately 90°C and determining the weight difference, the weight percentage has been obtained. Together with the sizes of the silica core and the collapsed core-shell particle from Table 4.1, and assuming a dense pure PNIPAm shell in the hydrophobic state, the particle volume fraction

Sample	$R_{H_{Si}}$	$R_{H_{total}}$ (swollen)	$R_{H_{total}}$ (collapsed)	ξ
SP-1	50 nm	100 nm	75 nm	1
SP-2A	54 nm	76 nm	59 nm	0.41
SP-2B	54 nm	125 nm	70 nm	1.32
SP-2C	54 nm	240 nm	100 nm	3.44
SP-3A	55 nm	140 nm	102 nm	1.55
SP-3B	55 nm	220 nm	100 nm	3

Table 4.1: Hydrodynamic radii R_H of all samples measured by DLS. The respective swollen radius relates to $T = 20°C$, the collapsed radius to $T = 40°C$. ξ indicates the particle "softness" calculated following Boles and Talapin [95, 96].

Φ_{coll} for the collapsed state can be calculated via:

$$\Phi_{coll} = \frac{V_{coll}}{V_{coll} + V_{H_2O}}. \tag{4.1}$$

Here, V_{coll} is the volume of the collapsed particle and V_{H_2O} the water volume per particle, obtained by

$$V_{H_2O} = \frac{\frac{m_{SiP}}{w} - m_{SiP}}{\rho_{H_2O}}. \tag{4.2}$$

m_{SiP} is the mass of silica-PNIPAm particle, w its weight fraction and ρ_{H_2O} the mass density of the solvent, i.e. water. With this an effective volume fraction of Φ_{eff} can be calculated for the system of swollen particles:

$$\Phi_{eff} = \frac{\Phi_{coll} \cdot V_{swoll}}{V_{coll}}. \tag{4.3}$$

Throughout the following chapters, the concentration of all samples is indicated with the effective volume fraction Φ_{eff} calculated with the radius of the particles obtained at room temperature of $T = 20°C$.

Sample SP-1 has been additionally studied under the influence of Trimethylamine *N*-oxide (TMAO) as co-solvent. For this purpose, a suspension with $\Phi_{eff} = 0.19$ has been diluted with TMAO solved in water. To keep the silica-PNIPAm concentration the same for all TMAO dilutions, the volume of both the silica PNIPAm and the added TMAO solution was kept constantly at 50:50 resulting in $\Phi_{eff} \approx 0.095$. The TMAO stock solution was prepared with 0 M, 0.2 M, 0.5 M and 1 M resulting in a concentration about 0 M, 0.11 M, 0.26 M and 0.52 M in the final silica-PNIPAm suspension.

4.2.1 Experimental procedure

The concentrated samples were studied by XPCS experiments, carried out at three different coherence beamlines of third generation storage rings: Beamline 8-ID-I at the Advanced Photon Source (APS), Argonne National Laboratory in Chicago, USA [97, 98], beamline ID10 at the Eurupean Synchrotron Radiation Facility (ESRF) in Grenoble [99], France and beamline P10 at PETRA III, DESY in Hamburg [100], Germany. In each case

the sample was studied with partially coherent X-rays in transmission SAXS or ultra-small angle X-ray scattering (USAXS) geometry in a temperature-adjustable vacuum sample chamber. Besides beamline-dependent parameters the experimental setup was the same for all experiments and is sketched in Fig. 3.8 (section 3.2).

At 8-ID-I, the scattered intensity was detected with a two dimensional LAMBDA 750K (Large Area Medipix Based Detector Array) detector [101] containing of 1536×512 pixels with a pixel size of $55 \times 55\,\mu m^2$ each and a dead time free readout up to a frame rate of 2 kHz. The detector was mounted with a sample-detector distance of 4.0 m. The capillaries with the samples were placed in the SAXS sample chamber in vacuum. The temperature of the capillaries is adjusted by a Peltier element integrated in the holder where usually two capillaries were placed at the same time. For two experiments performed at 8-ID-I, the beamline operated at 7.4 keV and 10.9 keV related to a wavelength of $\lambda = 1.7$ Åand $\lambda = 1.1$ Å, respectively. The corresponding speckle contrasts was 0.15 at 7 keV and 0.07 at 10.9 keV.

At ID10, the chosen energy was 8.1 keV corresponding to $\lambda = 1.53$ Å. The sample was mounted in the vacuum SAXS chamber in a copper capillary holder where the temperature was adjusted with a Peltier element. At the end of the flightpath with a distance of 5.3 m to the sample, the detector was placed on a stage. To detect the scattered intensity, a MAXIPIX (Multichip Area X-ray detector based on a photon-counting PIXel array) 2×2 array [102] was used, which achieves up to 300 Hz frame rate with 6 µs readout dead time containing 512×512 pixels with size of $55 \times 55\,\mu m^2$.

	8-ID-I, APS (I)	8-ID-I, APS (II)	ID10, ESRF	P10, PETRA III
Photon energy (keV)	7.4	11	8.1	8
Detector	Lambda 750K	Lambda 750K	MAXIPIX 2x2	EIGER X 4M
Sample-detector distance (m)	4.0	4.0	5.3	21.2
Beam size (μm^2)	20×20	20×20	10×10	80×80
Flux (photons/s)	$6 \cdot 10^9$	$6 \cdot 10^9$	$8.7 \cdot 10^{10}$	$6 \cdot 10^{11}$
τ_{min} (ms)	0.5	0.5	3.6	2
contrast β	0.15	0.07	0.3	0.18

Table 4.2: Experimental setup parameters of experiments performed at beamlines 8-ID-I (APS) (two separate experiments I and II), ID10 (ESRF) and P10 (PETRA III): Photon energy, sample-detector distance, beam size, flux and contrast.

The experiments at P10 have been performed in USAXS geometry at a photon energy of 8 keV, corresponding to a wavelength $\lambda = 1.55$ Å. As detector, a DECTRIS EIGER X 4M detector was implemented, which consists of 2070×2167 pixels with a pixel size of $75 \times$

$75\,\mu m^2$ and allows for framing rates up to 750 Hz. P10 has two experimental hutches located one after another, EH1 and EH2, whereas the standard sample environment of the beamline is installed in EH2. A second sample environment is located at EH1, enabling experiments in USAXS geometry. With the detector in EH1 and the sample in EH2 the experiment was performed with a sample-detector distance of 21.2 m.

Table 4.2 condenses the beamline-dependent parameters of all experiments at 8-ID, ID10 and P10. All experiments have been performed in a broad temperature range of approximately $15 - 45°C$ to quantify structural and dynamic changes around the LCST. Typically the temperature was increased stepwise starting from the lowest requested point. The samples were equilibrated about 600 s at each temperature before the respective measurement was started. At each temperature series of $500 - 4000$ speckle patterns with an illumination time of $0.5 - 3$ ms were taken. To improve the statistics the measurement for each temperature has been repeated at $10 - 20$ different sample spots and averaged.

5 Structural and Dynamical Properties of Silica-PNIPAm

The structural and dynamical properties of colloidal silica-PNIPAm suspensions have been studied at various concentrations, particle core to shell ratios and shell sizes. With DLS the diluted sample has been characterised to obtain the hydrodynamic radius of the core-shell particles. SAXS and USAXS provide information about the static assembly of the colloidal system. The dynamics of the sample are probed with XPCS, by analysing temporal correlations in the scattered intensity [65]. To obtain a general idea about the structure and dynamics of Silica-PNIPAm dispersions, firstly the static and dynamical results of sample SP-2B at a concentration of $\Phi_{\text{eff}} = 0.55$ are shown and discussed in detail. Subsequently, the influence of sample concentration, PNIPAm shell size and the addition of TMAO as co-solvent is discussed.

5.1 Structural properties: SAXS results

The structural order of silica-PNIPAm suspensions was studied with SAXS. To obtain the structural information from the scattered intensity, a series of coherent diffraction patterns has been averaged. For the orientation independent $I(q)$, the two-dimensional patterns were averaged azimuthally.

The scattered intensity $I(q)$ contains information about both the size and form of the particles, described by the particle form factor $P(q)$ as well as interparticle correlations leading to a superstructure, described by the static structure factor $S(q)$ (see section 3.2.3):

$$I(q) \propto P(q) \cdot S(q). \tag{5.1}$$

To determine the particle form factor $P(q)$, each sample system was measured at low concentrations with $\Phi_{\text{eff}} < 0.05$ where interparticle interactions can be neglected. In this case, the structure factor is $S(q) = 1$ which leads to $I(q) = P(q)$. The intensity profile obtained with a dilute system hence can be described by a spherical core-shell model with a Schulz-Zimm size distribution of the core radius.

5.1.1 Form factor analysis

Each sample has been measured at 25°C in a dilute suspension to obtain the particle form factor. Due to the high electron density of silica compared to PNIPAm the scattering signal is dominated by the core. For sample SP-2B the model gives an averaged radius of $\bar{R} = R_{\text{Si}} = 47\,\text{nm}$. The form factor and the fit are shown in Fig. 5.1a together with the particle size distribution $D(R)$. For a spherical object the hydrodynamic radius R_{H} is typically larger than R obtained by the form factor fit. This can be attributed to a

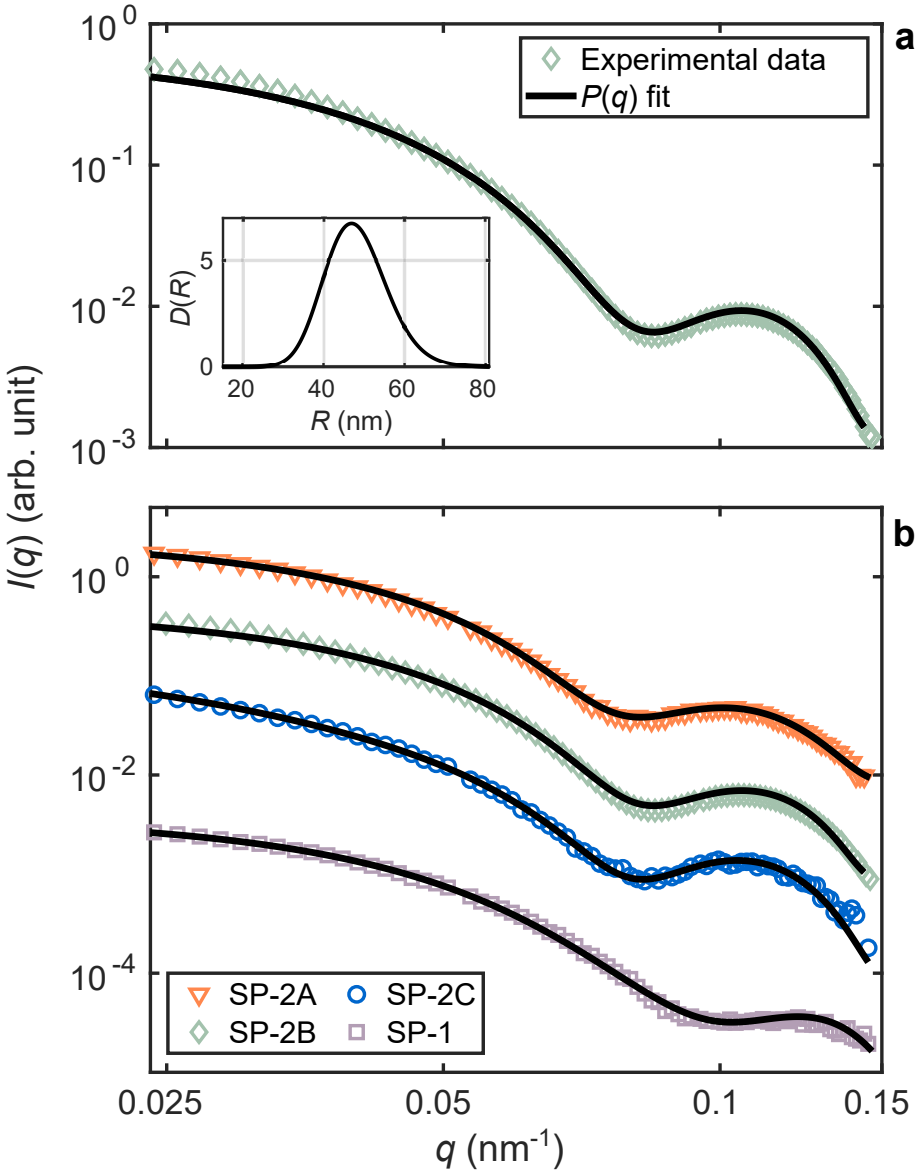

Figure 5.1: SAXS results of SP-2 and SP-1 at 20°C: (a) Intensity profile $I(q)$ of the dilute silica-PNIPAm sample SP-2B. The inset shows the size distribution $D(R)$ for the core, obtained with a Schulz-Zimm distribution. (b) $I(q)$ of SP-1 and all SP-2 with varied shell thickness. From top to bottom SP-2A (orange ▽, swollen shell size of $d \approx 22\,\mathrm{nm}$), SP-2B (green ◇, swollen shell size of $d \approx 71\,\mathrm{nm}$), SP-2C (blue ◯, swollen shell size of $d \approx 186\,\mathrm{nm}$) and $I(q)$ of SP-1 (purple □). The profiles are shifted vertically for clarity. The black lines in (a) and (b) represent the respective fit with a spherical core-shell form factor.

thin solvent layer on the particle surface which moves with the particle. Consequently the particle appears larger for visible light [70] (see Table 5.1). In Fig. 5.1b the $I(q)$ of all studied samples are compared. The upper three curves represent SP-2 with three different shell sizes grafted on silica cores from the same batch, whereas the middle curve is the same as in Fig. 5.1a. All three $I(q)$ resemble each other with the form factor minimum at $q_{\mathrm{min}} \approx 0.083\,\mathrm{nm}^{-1}$, which clarifies that the scattering signal originates mainly from the silica core with little influence of the PNIPAm shell. The lowest profile relates to SP-1, with slightly smaller silica cores which is observed in a shift of the first minimum to a

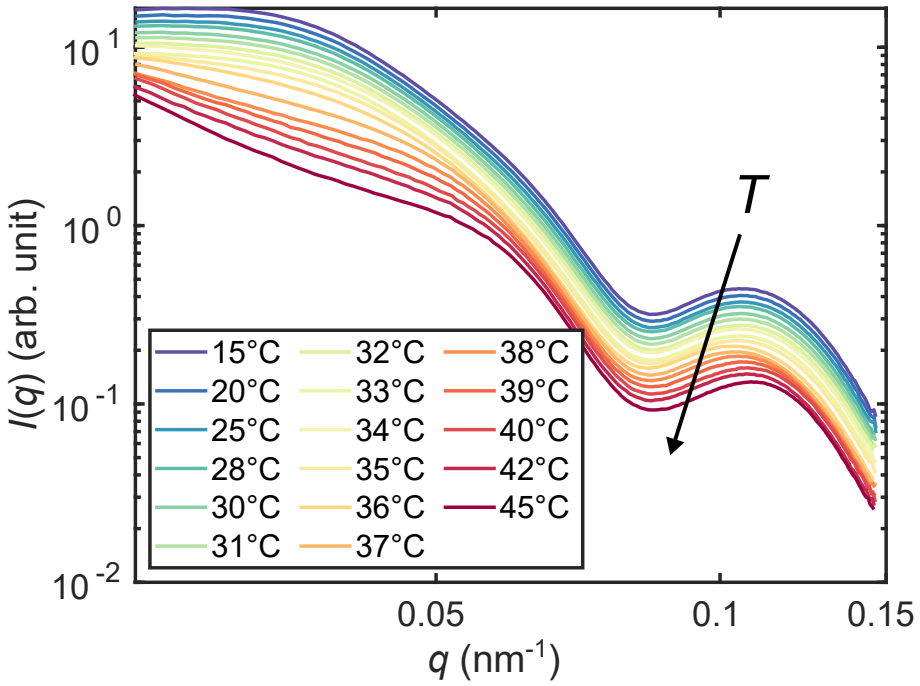

Figure 5.2: SAXS results of concentrated silica-PNIPAm, sample SP-2B at $\Phi_{\text{eff}} = 0.55$. $I(q)$ is shown upon heating from 15°C (blue) to 45°C (red). The profiles have been shifted vertically for clarity.

larger q value $q_{\text{min}} = 0.095\,\text{nm}^{-1}$.

Sample	R_{Si} (SAXS)	$R_{\text{H}_{\text{Si}}}$ (DLS)
SP-1	44.5 nm	50 nm
SP-2A	47	54 nm
SP-2B	47	54 nm
SP-2C	49	54 nm
SP-3A	50	55 nm
SP-3B	50	55 nm

Table 5.1: Silica radii of all samples measured by SAXS and DLS.

5.1.2 Structural properties of dense-packed silica-PNIPAm

For the densely-packed sample, interparticle correlations affect the static scattering signal and $S(q)$ cannot be neglected. Fig. 5.2 shows the scattering intensity of sample SP-2B at $\Phi_{\text{eff}} = 0.55$ as a function of temperature between 15°C and 45°C. All intensity profiles between $T = 15$°C and 36°C resemble each other in the whole covered q range. Upon heating from $T = 37$°C to 45°C the intensity profiles start to decrease continuously in magnitude for $0.026\,\text{nm}^{-1} < q < 0.055\,\text{nm}^{-1}$ whereas the intensity increases for $q \to 0$. The change in $I(q)$ can be attributed to the collapsing shells since the minimum at $q = 0.085\,\text{nm}^{-1}$ arising from the spherical form factor of the silica particles remains temperature independently constant for all $I(q)$. For $T > 37$°C, the q regime of the

occurring feature relates to a scale in the range of the particle size including the shell.

This effect has been studied deeperwith sample SP-1 upon variation of concentration. For this purpose, a sample with $\Phi_{\text{eff}} = 0.19$ has been diluted systematically. Fig. 5.3a shows the temperature profile of the $I(q)$ for SP-1 at three concentrations $\Phi_{\text{eff}2} = 0.12$, $\Phi_{\text{eff}2} = 0.15$ and $\Phi_{\text{eff}3} = 0.19$.

For all concentrations the $I(q)$ are almost identical for $T < 36°\text{C}$. Above this threshold temperature $T_c \approx 36°\text{C}$ a temperature and concentration dependency is found. For temperatures $T > T_c$ all intensity profiles show an increase at low q values while a dip in intensity appears for approximately $0.03 < q < 0.06\,\text{nm}^{-1}$ as it has been observed previously for SP-2B in Fig. 5.2. The effect is illustrated in Fig. 5.3b where the intensity at a selected q value of $q_p = 0.042\,\text{nm}^{-1}$ is shown for all Φ_{eff} and T. With the profiles calibrated to $I(q_\text{p})$ of $\Phi_{\text{eff}1}$ at $T = 25°\text{C}$ the trend can be clearly identified as an effect of concentration whereby the decrease of $I(q_\text{p})$ becomes larger for higher concentrations.

5.1.3 Influence of the shell size on the structure formation

Additionally to the study of concentration dependence, the effective volume fraction Φ_{eff} was changed by variation of the PNIPAm layer thickness while keeping the core size constant. The samples are classified via their softness ξ following the the definition of Boles and Talapin [95, 96]. Three different shell sizes have been grafted on silica cores from the same batch, *i.e.* the samples SP-2A with $\xi_{2\text{A}} \approx 0.41$, SP-2B with $\xi_{2\text{B}} \approx 1.31$ and SP-2C with $\xi_{2\text{C}} \approx 3$, all calculated for the swollen particles at 20°C (see Tab. 4.1). Thus, a wide range of Φ_{eff} could be covered of $\Phi_{\text{eff}}(\text{SP}_{2\text{A}}) \approx 0.13$, $\Phi_{\text{eff}}(\text{SP}_{2\text{B}}) \approx 0.55$ and $\Phi_{\text{eff}}(\text{SP}_{2\text{C}}) \approx 0.73$. Therein SP-2B has already been discussed in section 5.1.2 (Fig. 5.2).

Fig. 5.4 compares the temperature dependent intensity profile of SP-2B (Fig. 5.2) with the profile of SP-2A and SP-2C. For all three samples the minimum related to the core remains constant at $q \approx 0.08\,\text{nm}^{-1}$, however, the $I(q)$ show a clear influence of the shell in the lower q regime ($q < 0.05\,\text{nm}^{-1}$). For SP-2A (Fig. 5.4 a) the signal resembles the $P(q)$ and the upturn of magnitude in $I(q)$ for $q \to 0$ and high T as described above (Fig. 5.2) is marginal. The direct comparison to SP-2B (Fig. 5.2 and 5.4 b) further shows as well a generally increased intensity for SP-2B and indications of formation of a structure factor at low T. This can be attributed to the higher packing fraction and hence an increased scattering signal at the length scale of the nearest neighbour distance. SP-2C shows a second oscillation with a minimum at $q \approx 0.033\,\text{nm}^{-1}$ for the lowest temperatures. Upon heating the amplitude of the oscillation reduces until the $I(q)$ shows only the core related minimum at $T = 36°\text{C}$. With further heating a similar but stronger upturn in $I(q)$ for $q \to 0$ as for SP-2B starts to occur. In contrast to the samples with thinner PNIPAm shells, the shell of SP-2C shows a clear influence on the $I(q)$ at temperatures below the LCST of 32°C.

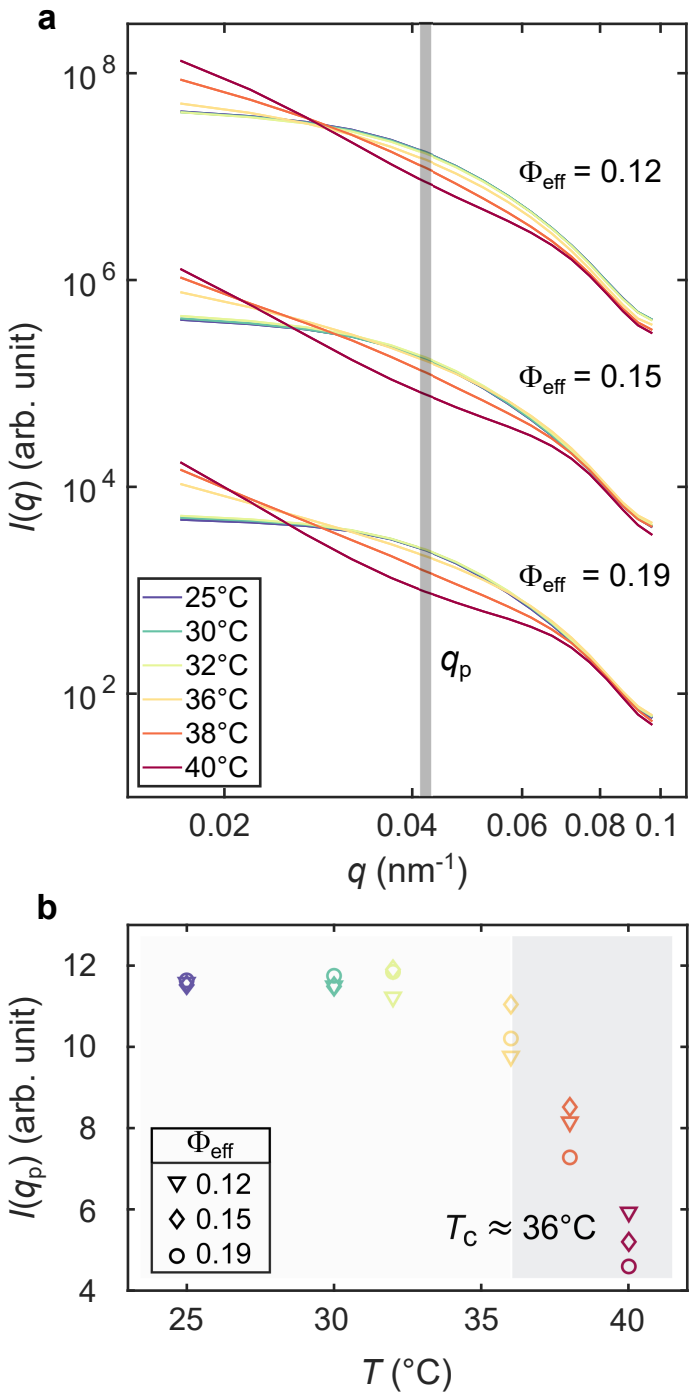

Figure 5.3: SAXS results of SP-1: (a) $I(q)$ of Silica-PNIPAm for $\Phi_{\text{eff}} = 0.12$, 0.15 and 0.19, respectively, measured between 25°C and 40°C. Intensity profiles have been shifted vertically for clarity. (b) Intensity $I(q_{\text{p}})$ at $q_{\text{p}} = 0.042\,\text{nm}^{-1}$ as a function of temperature for all concentrations.

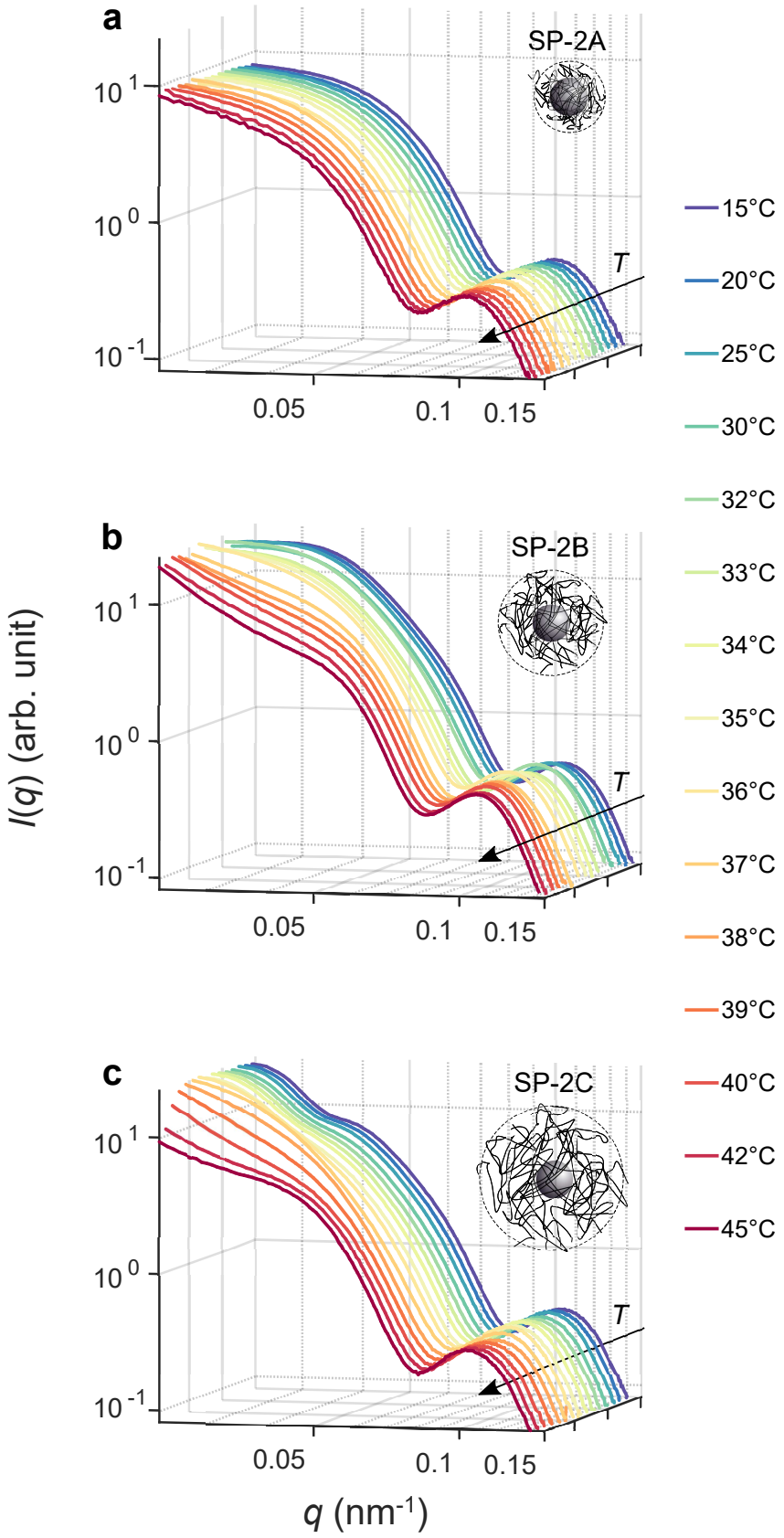

Figure 5.4: SAXS results of SP-2 under variation of the PNIPAm layer thickness: $I(q)$ of Silica-PNIPAm from top to bottom (a) SP-2A ($\Phi_{\text{eff}}(\text{SP}_{2\text{A}}) \approx 0.13$), (b) SP-2B ($\Phi_{\text{eff}}(\text{SP}_{2\text{B}}) \approx 0.55$) and (c) SP-2C ($\Phi_{\text{eff}}(\text{SP}_{2\text{C}}) \approx 0.73$), all measured between 15°C and 45°C. The arrow indicates the increase of temperature.

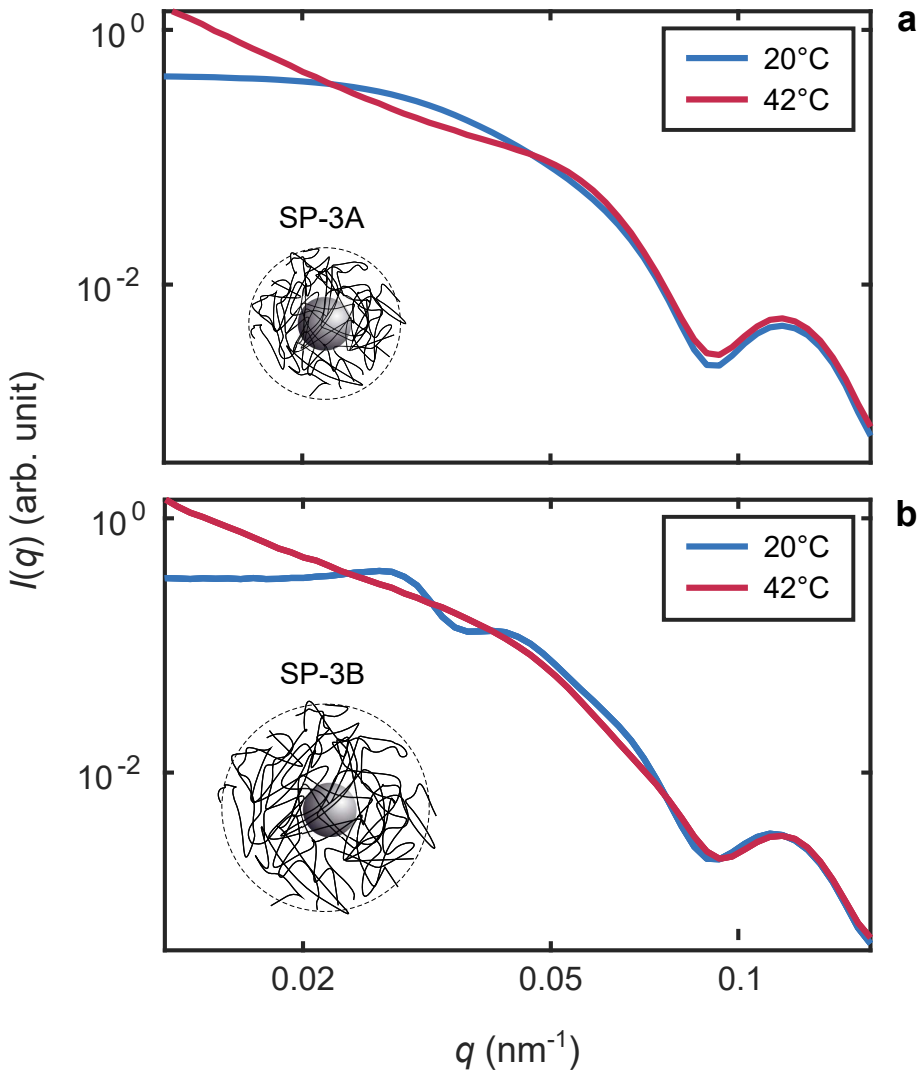

Figure 5.5: USAXS results: Scattered intensity of SP-3 under variation of the PNIPAm layer thickness. $I(q)$ of Silica-PNIPAm (a) SP-3A, (b) SP-3B each for 20°C and 42°C.

5.1.4 Ultra-small-angle X-Ray scattering

In order to deepen the observation of section 5.1.3 and to access a length scale comparable to the particle shell size and larger, a wave vector transfer $q \approx 0.01\,\mathrm{nm}^{-1}$ is required. This requirement has been fulfilled by measuring in ultra-small-angle X-Ray scattering (USAXS) geometry with a large sample-to-detector distance (see section 4.2.1). For this purpose, a fresh batch of silica-PNIPAm was prepared obtaining the samples SP-3A and SP-3B with comparable core and shell sizes as SP-2B and SP-2C. The radius of the core is $R_{\mathrm{HSi}} \approx 55\,\mathrm{nm}$, the shell of SP-3A $d_{3\mathrm{A}} \approx 85\,\mathrm{nm}$ and the shell of SP-3B $d_{3\mathrm{B}} \approx 165\,\mathrm{nm}$. Both samples were again studied at various temperatures below and above the LCST.

Fig. 5.5 shows the $I(q)$ of SP-3A at $\Phi_{\mathrm{eff}} = 0.38$ and SP-3B at $\Phi_{\mathrm{eff}} = 1.35$ both for $T = 20$°C and 42°C. For SP-3B with the large shell the sample volume is over-packed. With PNIPAm as a soft nanogel, the particles can be deformed which enables volume fractions $\Phi_{\mathrm{eff}} > 1$ [18, 44].

SP-3A (Fig. 5.5a) resembles SP-2B (Fig. 5.2) *i.e.* the $I(q)$ shows an upturn for $q \to 0$

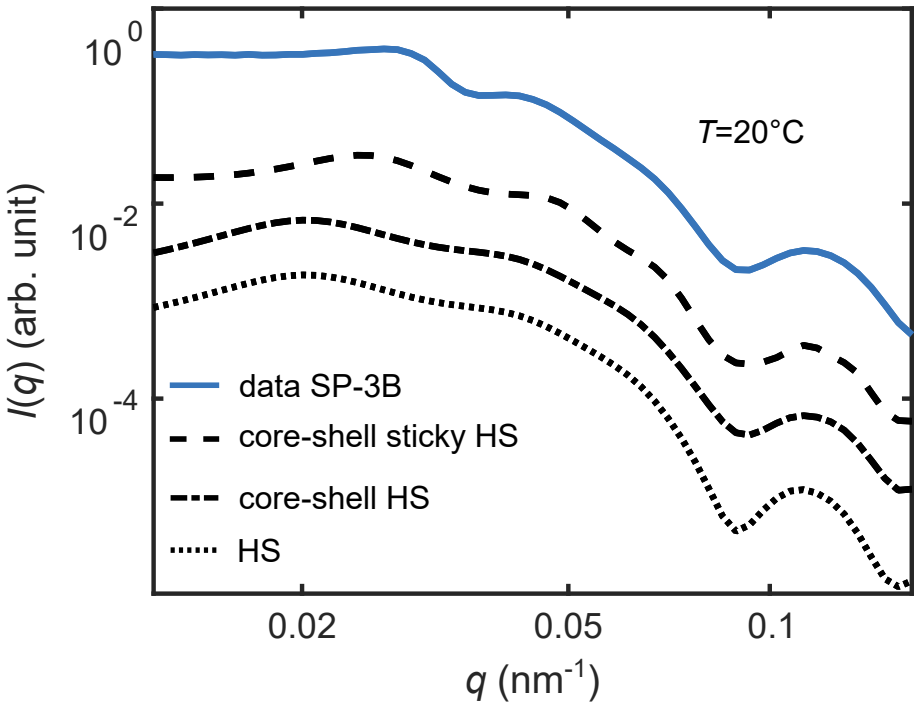

Figure 5.6: Scattered intensity of SP-3B at $\Phi_{\text{eff}} = 1.35$ with the calculated $I(q)$ of a hard sphere (HS) system (dotted line), a core-shell hard sphere system (dashed line) and a core-shell sticky hard-sphere system (solid line).

and no indications of a structure factor in the extended q regime. In contrast, SP-3B shows pronounced oscillations in the small q region for low temperatures which disappear with the collapse of the shell, similar to SP-2C (Fig. 5.4). To find a model describing the $I(q)$ of SP-3B at 20°C, the scattered intensity has been calculated for different model systems. Fig. 5.6 compares SP-3B with the $I(q)$ of a hard sphere (HS) system (dotted line), a core-shell hard-sphere system (dashed line) and a core-shell sticky hard-sphere system (solid line) (see section 3.2.3). For all three models the core size, dispersity and repulsion radius were kept constant at $R = 48\,\text{nm}$, $p = 0.15$ and $RR = 140\,\text{nm}$. The comparison of the models with the data shows that both core-shell models match the data in the higher q region for $q > 0.05\,\text{nm}^{-1}$ where the scattering signal originates mainly from the core. For $q > q_{\text{max}}$ with $q_{\text{max}} = 0.028\,\text{nm}^{-1}$ as the position of the structure factor peak the core-shell sticky hard-sphere model describes the data well. However, at low q none of the models matches the data well. In the low q regime all models show an increase of intensity for $q < q_{\text{max}}$ whereas the data shows a plateau in this regime. Clearly, the hard sphere and the core-shell hard-sphere model are not well suited to explain the data in the low q regime. The core-shell sticky hard-sphere model resembles the data best on a qualitative level, however, the discrepancy of the scattered intensity on this length scale suggests the presence of agglomeration which are not captured in the model.

In Fig. 5.7a the scattering intensity of SP-3B at $\Phi_{\text{eff}} = 1.35$ is shown together with the measured particle form factor $P(q)$, obtained from a dilute suspension. The comparison clarifies that the peaks in the $I(q)$ for $q < 0.07\,\text{nm}^{-1}$ are not described by the form factor. By dividing the $I(q)$ of the concentrated sample by the scattered intensity $P(q)$ of the

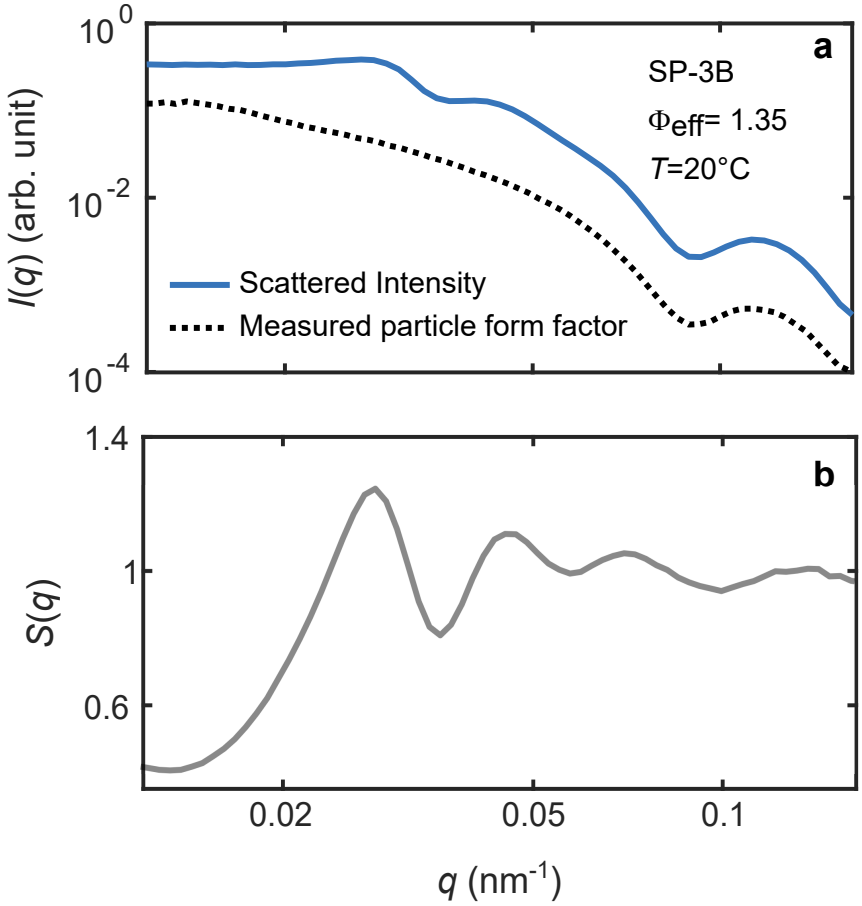

Figure 5.7: a) $I(q)$ of SP-3B at $\Phi_{\text{eff}} = 1.35$ together with the measured particle form factor $P(q)$ as the scattering intensity of SP-3B for a diluted suspension, both at $T = 20°\text{C}$. b) Static structure factor $S(q)$ obtained by division of the data sets (Eq 5.2).

dilute sample the static structure factor can be extracted via

$$S(q) = \frac{I(q)}{aP(q)}. \tag{5.2}$$

Therein a denotes a scaling factor, related to the number of scatterers in the illuminated volume. The obtained static structure factor is shown in Fig. 5.7b. It has a pronounced peak at $q_{\text{max}} = 0.028\,\text{nm}^{-1}$ and oscillates around unity towards larger q.

The static structure factor of SP-3B has been collected for various volume fractions and temperatures between 20°C and 40°C (Fig. 5.8). Each $S(q)$ has been obtained by division of the respective $I(q)$ by $P(q)$ of the same temperature.

Fig. 5.8a shows the $S(q)$ of SP-3B for $\Phi_{\text{eff}} = 0.33$, 0.50, 0.68, 0.85, 1.02 and 1.35. Two effects can be observed from low to high packing fractions: First, the position q_{max} of the first peak shifts to larger q values and second, the peak height increases matching the models shown in section 3.2.3, Fig. 3.7a and b.

For $\Phi_{\text{eff}} = 0.33$ only a weak structure factor peak is found for $T \geq 36°\text{C}$. Due to poor statistics the data for $\Phi_{\text{eff}} = 0.33$ at 37°C is not shown. The comparison of Fig. 5.8f with Fig. 5.8g clearly demonstrates the structural transition between 37°C and 38°C. The

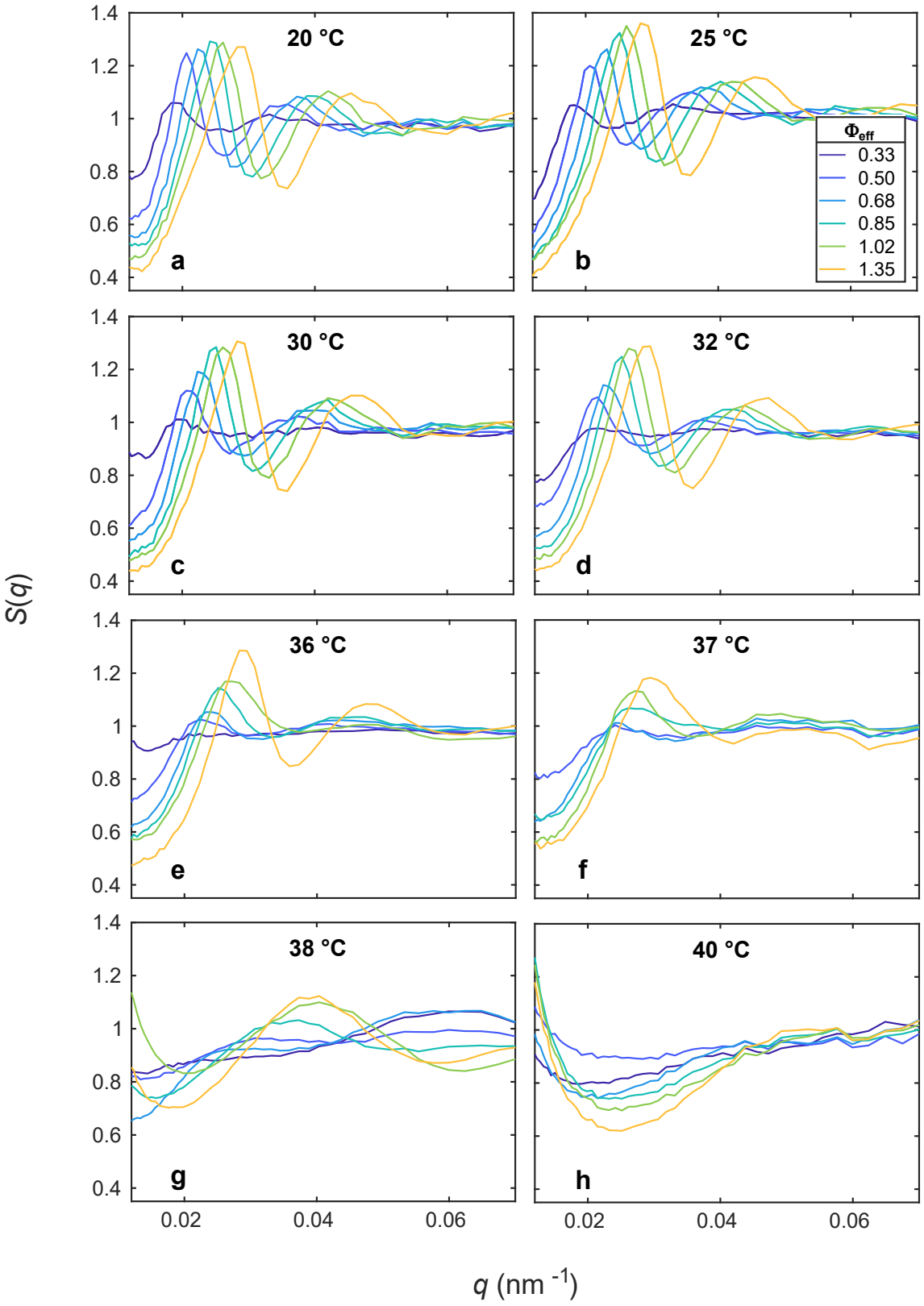

Figure 5.8: Static structure factors $S(q)$ of SP-3B for six volume fractions between $\Phi_{\text{eff}} = 0.33$ and 1.35 obtained at a) 20°C, b) 25°C, c) 30°C, d) 32°C, e) 36°C, f) 37°C, g) 38°C and h) 40°C. Due to poor statistics the data for $\Phi_{\text{eff}} = 0.33$ at 37°C is not shown.

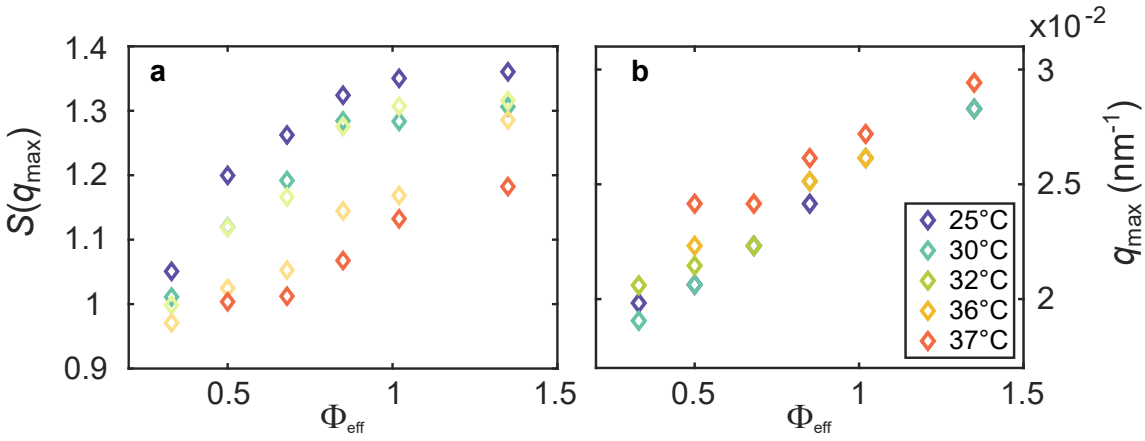

Figure 5.9: Temperature dependency of a) $S(q_{\max})$ and b) $q_{\max}$ for SP-3B at $0.33 < \Phi_{\text{eff}} < 1.35$.

$S(q)$ at 37°C resembles the structure factors in Fig. 5.8a-e apart from the peak height and width. At 38°C no peak at $q_{\max}$ is observed for $\Phi_{\text{eff}} = 0.33$, 0.50 and 0.68. For $\Phi_{\text{eff}} \geq 0.85$ the corresponding $S(q)$ peak is broadened and shifted to larger q for all Φ_{eff} with $\Delta q \approx 0.01\,\text{nm}^{-1}$. Further, the $S(q)$ shows an upturn for $q \to 0$ as seen in section 3.2.3, Fig. 3.7c for low stickiness parameters. At 40°C none of the concentrations shows a $S(q)$ peak in the whole q range whereas all datasets show a strong upturn towards small q pointing out the formation of a sticky particle system.

The $S(q_{\max})$ and $q_{\max}$, if identifiable, are shown in Fig. 5.9 for all volume fractions. in general, the height of the peak $S(q_{\max})$ decreases for higher temperatures (Fig. 5.9b) which can be associated with a reduction of the volume fraction due to less order in the system. In parallel, for each temperature, $S(q_{\max})$ increases with higher volume fractions, as expected. The peak positions $q_{\max}$ show a tendency to larger q indicating a decreased interparticle distance (Fig. 5.9b) [46]. If no marker is visible, the positions are found to be the same as for the temperature plotted on top. At each temperature, the value of $q_{\max}$ increases with higher Φ_{eff} pointing out a lower interparticle distance, respectively.

5.1.5 Reversibility

In order to study the reversibility of the previously described structural transition in highly concentrated silica-PNIPAm systems, the SAXS measurements have been performed both upon heating from 25°C to 45°C and with subsequent stepwise cooling down to 25°C. Fig. 5.10 shows the obtained intensity profiles for SP-1 at $\Phi_{\text{eff}} = 0.19$. The change in $I(q)$ related to the collapsing PNIPAm shell, which appears for 36°C$< T <$ 45°C (see also Fig. 5.3), disappears with decreasing temperature. In an iterative process the temperature of sample system SP-3B has been risen and lowered multiple times between 20°C and 45°C (Fig. 5.11). All $I(q)$ at 20°C (blue) and at 45°C (red) resemble each other, even after many heating and cooling iterations. The structure factor observed for $T < T_c$ is fully reverted in each cooling process.

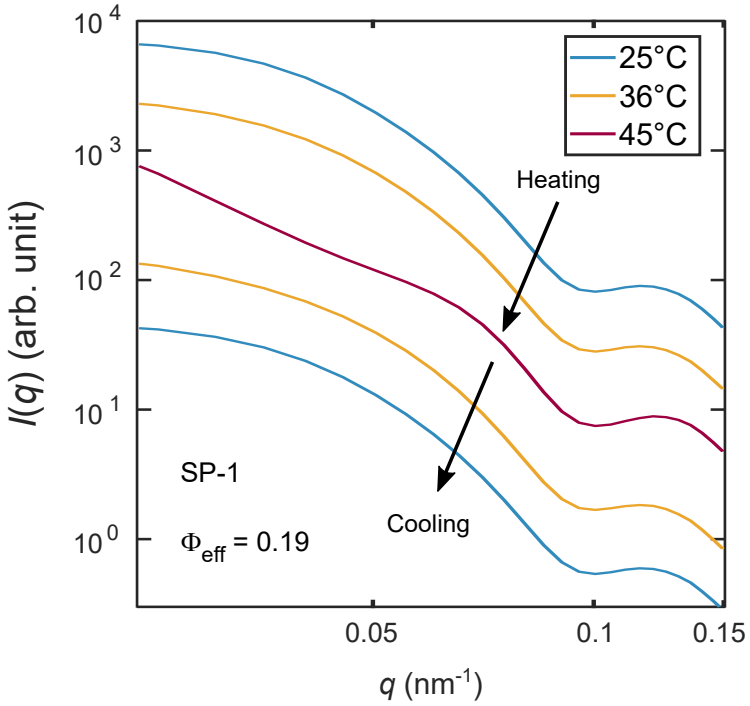

Figure 5.10: $I(q)$ of SP-1 for $T = 25°C$, 40°C and 45°C in a bidirectional manner. The arrow indicates the sequence of the measurements.

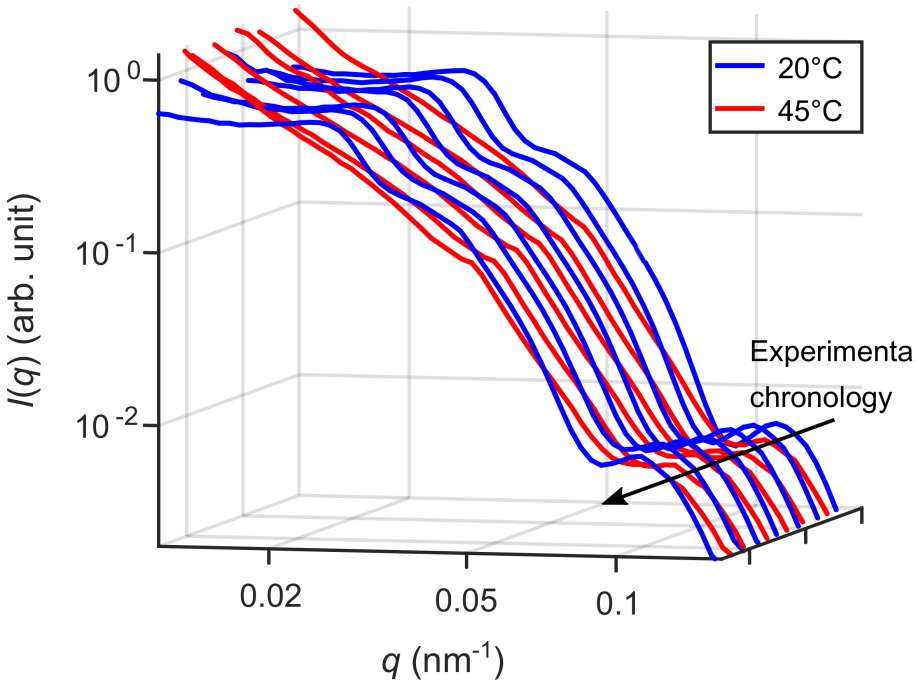

Figure 5.11: $I(q)$ of SP-3B obtained in heating and cooling cycles, iterating between 20°C to 45°C.

5.2 Structural influence of TMAO as co-solvent

The influence of TMAO on the temperature-dependence of the structure has been studied for sample SP-1. In Fig. 5.12a-d the $I(q)$ of the four systems are compared for all obtained temperatures between 20°C and 45°C. At low temperatures TMAO has no influence on the structural properties of silica-PNIPAm, independent of the TMAO concentration. The direct comparison of the pure sample (Fig. 5.12a) with the 0.11 M TMAO sample (Fig. 5.12b) shows a more distinct decay of intensity with TMAO and a shift to a lower transition temperature T_c.

While the pure sample shows an upturn in intensity at $T = 42$°C for $q \to 0$, it is observed already at $T = 39$°C for the sample with 0.11 M TMAO. For 0.26 M TMAO the change in $I(q)$ starts at around $T = 36$°C. On the contrary, no temperature-induced change of intensity is determined for the sample with 0.52 M and the $I(q)$ resembles the form factor of the core-shell system. The higher transition temperature of the pure sample compared to SP-1 in section 5.1.2 is interpreted as an effect of lower particle concentration.

Fig. 5.12 shows the $I(q)$ of SP-1 at $\Phi_{\text{eff}} = 0.095$ purely in water (0 M TMAO) and with 0.11 M, 0.26 M and 0.52 M TMAO 20°C and 45°C. The pure aqueous sample shows the

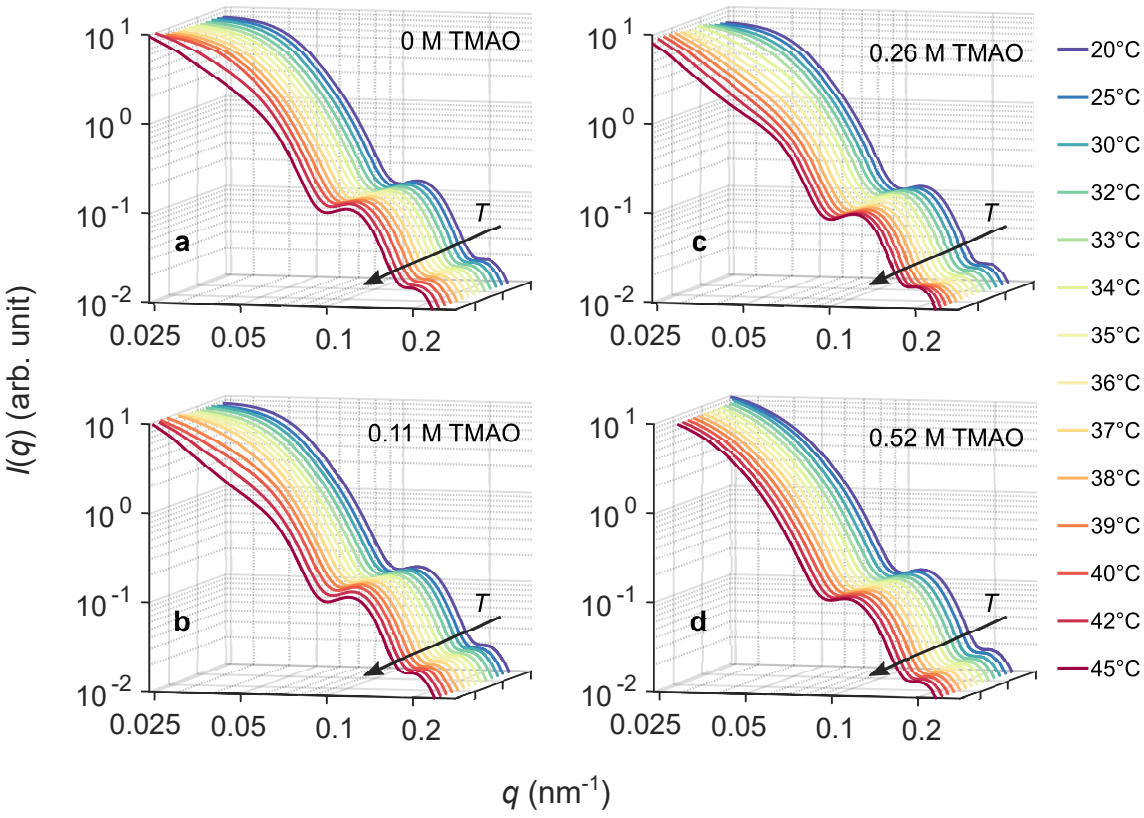

Figure 5.12: Temperature dependent $I(q)$ of a) SP-1 in pure water and b)-d) with addition of a 0.11, 0.26 and 0.52 M TMAO suspension. All samples are measured between 20°C and 45°C.

previously observed change in intensity at low q for 45°C compared to 20°C, pointing to attractive forces in the system at high T. The temperature-induced increase of intensity for $q \to 0$ is observed for 0 M, 0.11 M and 0.26 M and it is slightly more pronounced with

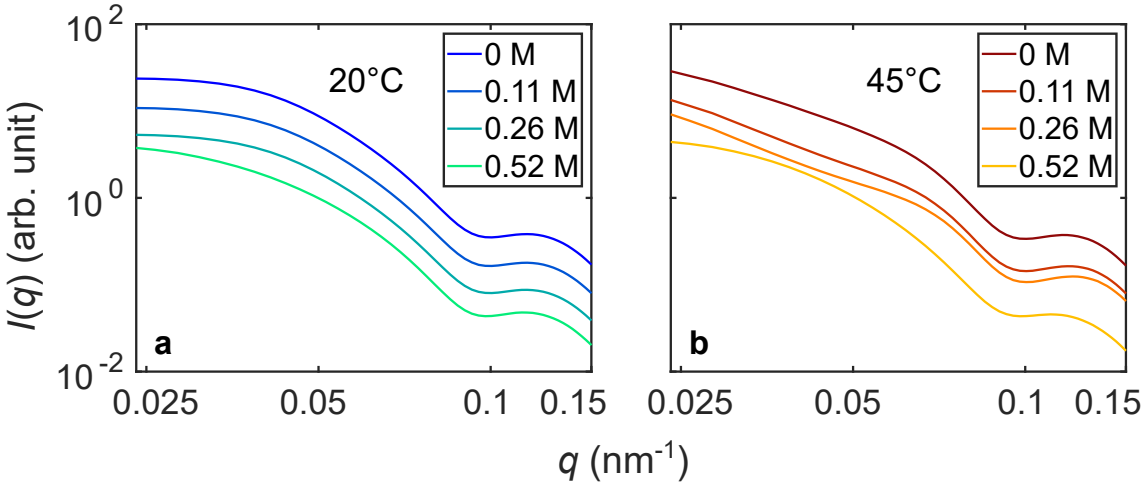

Figure 5.13: $I(q)$ of SP-1 water (0 M TMAO) and with 0.11 M TMAO, 0.26 M TMAO and 0.52 M TMAO at a) 20°C and b) 45°C. The intensity profiles are shifted vertically for clarity

the addition of TMAO. For 0.52 M TMAO the intensity profiles of 20°C and 45°C resemble each other and show no indication of attractive forces at 45°C.

5.3 Interpretation and discussion of the structural properties

For all samples, an upturn of intensity was found upon heating for $q \to 0$. It suggests the appearance of attractive forces in the system [103] once the shells of the particles are fully collapsed at $T \approx 37$°C (compare R_H in Fig. 5.17a). At lower temperatures where the PNIPAm shells are swollen with water, van der Waals attraction between the particles can be neglected since matching of the refractive indices between particles and solvent leads to a Hamaker constant $H \approx 0$ (see Eq. 2.1). Soft sphere particles as PNIPAm permit to be compressed in dense assemblies [46]. This results in a repulsive short-range interaction potential between the swollen particles. At high temperatures the shell is collapsed and hence the density and stiffness of the polymer shell increased. The occurring hydrophobic interaction and stronger van der Waals forces lead to short range attraction in the colloidal system [3, 44, 104]. The appearing change of $I(q)$ for concentrated systems at $q \to 0$ and temperatures above the transition temperature $T_c \approx 36$°C is hence associated with agglomerations of particles, favourable due to de-swelling of the PNIPAm shells with the ability to be deformed and/or inter-penetrated as sketched in Fig. 5.14 [44–46].

The structural transition from a repulsive to an attractive system is clarified with the data taken in USAXS geometry, where a static structure factor $S(q)$ could be obtained for sample SP-3B. For all volume fractions a decrease of interparticle distance is observed upon heating from 20°C to 37°C (Fig. 5.9). An upturn of $I(q)$ for $q \to 0$ appears at 38°C and even stronger at 40°C resembling the sticky hard sphere model shown in Fig. 3.7c [30,31]. This points to agglomerations, favoured by sticky particles with attractive interaction at 38°C and 40°C which was not observed for 37°C. The result thus confirms the transition from repulsive to attractive interactions indicated in the previous SAXS results whereas

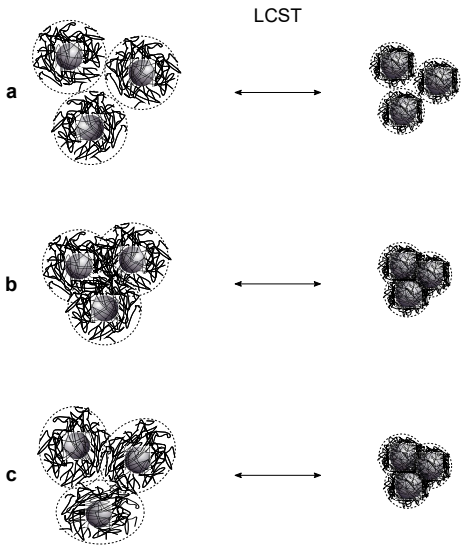

Figure 5.14: Sketch of possible behaviour of silica-PNIPAm particles at high packing fractions before and after the collapse at the LCST. a) Particles without interpenetration b) interpenetrating particle shells and c) deformed and interpenetrating particle shells. The grey circles in the middle of the particles represent the silica cores and the black lines represent the PNIPAm network. The dashed lines indicate the effective particle form and size.

the stickiness of the particles increases at temperatures $T > T_c$.

The temperature-induced structural transition was found to be reversible. Even after multiple iterations of heating with subsequent cooling the $I(q)$ show full reversibility. This points to a reversible transition from repulsive to attractive interparticle interactions.

The addition of TMAO to the silica-PNIPAm suspension, affects the critical temperature T_c. The shift of T_c with increasing TMAO concentration is in qualitative agreement with previous observations. It is known, that the presence of TMAO in dilute aqueous PNIPAm suspensions stabilizes the globular PNIPAm state and shifts the LCST to lower temperatures [53, 55] which is also suggested by comparison of the data with 0 M, 0.11 M and 0.26 M. With the strong hydrophilicity of TMAO and the preferential attraction of TMAO to the globular PNIPAm state [53] the $I(q)$ of 0.52 M TMAO can be interpreted as the scattering signal of temperature-independently collapsed particles, that behave like simple spheres.

5.4 Dynamic properties

In a dilute suspension the absence of interparticle interactions leads to diffusive particle motion. In this case, the intensity autocorrelation function g_2 can be obtained by DLS. For highly concentrated suspensions, which are often optically opaque, multiple scattering effects occur for visible light. Hence the dynamic properties of the densely-packed colloidal systems were probed with XPCS.

The dynamical information of the colloidal system is contained in the normalized second order intensity-autocorrelation function g_2 which is obtained by both DLS and XPCS. For many soft matter systems the g_2 function can be described with the Kohlrausch-Williams-Watts (KWW) function, given by Eq. (3.34) in section 3.3.1

$$g_2(q,\tau) = 1 + \beta \exp\left[-2\left(\Gamma(q)\cdot\tau\right)^{\gamma}\right] \quad .$$

Here $\beta(\boldsymbol{q})$ is the speckle contrast depending on the coherence of the source [70], γ is the KWW exponent and $\Gamma(q)$ the relaxation rate which relates to the characteristic relaxation time τ_c via $\Gamma = \tau_c^{-1}$. In the following, all g_2 functions are fitted by a KWW function except where otherwise specified.

5.4.1 Radiation damage

PNIPAm is a highly radiation sensitive system which requires a careful exposure of the sample to the X-ray beam [18]. After variation of attenuators, exposure times and beam sizes while observing the static and dynamic signal, exposure times between 0.5 ms and 3 ms per speckle pattern have been selected with series of $500 - 4000$ diffraction patterns at each sample spot. Within the chosen time scale any effect resulting from beam damage could be avoided. Fig. 5.15 shows the mean intensity $\langle I \rangle$ for 4000 patterns with 0.5 ms exposure, *i.e.* a total time of 2 s obtained with sample SP-2B. Over the whole illumination time, the mean intensity $\langle I \rangle$ remains constant, pointing towards the absence of radiation damage which could affect the stability. The total illumination time, *i.e.* the sum of

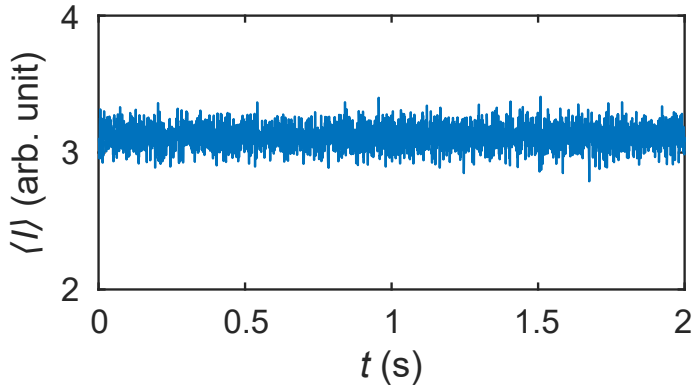

Figure 5.15: Stability plot of the mean intensity for 4000 diffraction patterns with an 0.5 ms illumination time per pattern, obtained for SP-2B at $\Phi_{\text{eff}} = 0.55$.

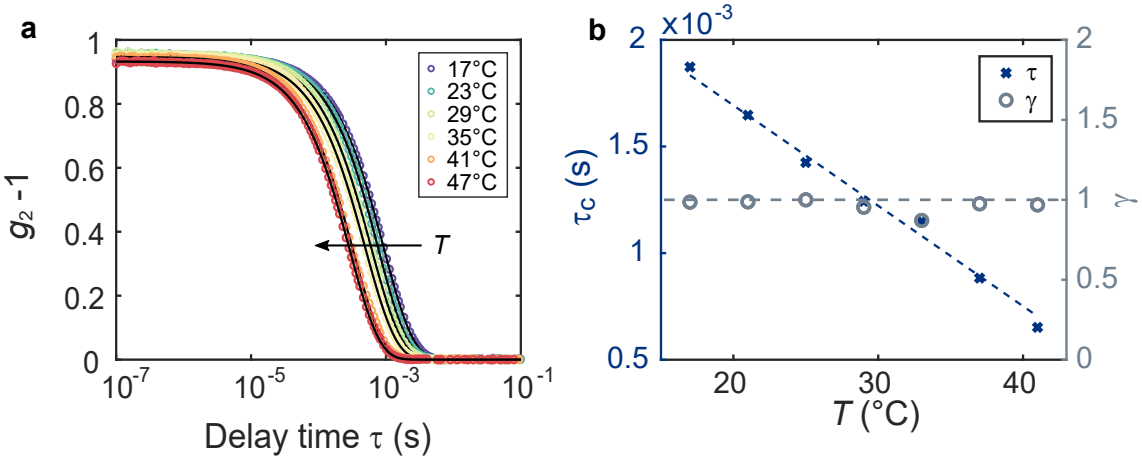

Figure 5.16: DLS results: a) Intensity autocorrelation functions $g_2 - 1$ as a function of temperature between $T = 17°C$ and 47°C, obtained by DLS at $q = 0.018\,\mathrm{nm}^{-1}$. The black lines represent KWW fits to the data. b) Characteristic relaxation time τ_c (blue ×, left axis) and KWW exponent γ (grey ∘, right axis) both as a function of temperature.

exposure times per series of diffraction patterns, can be related to a dose D [105]

$$D = 1000 \frac{N\,E}{\rho\,A\,\ell}\left(1 - \frac{1}{\exp(\rho\,\mu\,\ell)}\right) \quad . \tag{5.3}$$

Here N is the total number of photons on the sample and E the energy per photon. ρ represents the effective total density, $A(\mathrm{cm}^2)$ the beam size area and $\ell\,(\mathrm{cm})$ the sample thickness. The mass attenuation coefficient μ depends on the sample material and the photon energy. Here it was calculated for silica-PNIPAm using the NIST XCOM Photon Cross Sections Database [106] to $\mu_{\mathrm{SiP}} = 45.67\,\mathrm{cm}^2/\mathrm{g}$ for 7.4 keV.With 4000 diffraction patterns of 0.5 ms each, a dose of $D \approx 3 \times 10^4\,\mathrm{Gy}$ is reached which is below the radiation damage threshold for such silica-PNIPAm core shell systems of $D_{\mathrm{max}} \approx 1 \times 10^5\,\mathrm{Gy}$ [18]. For longer exposure times per single diffraction pattern D was kept constant by means of attenuators.

5.4.2 Dynamics of non-interacting silica-PNIPAm particles

To probe the dynamics of aqueous silica-PNIPAm without interparticle interactions and to characterize the thermo-responsive behaviour, all samples have been measured in a highly dilute state with $\Phi_{\mathrm{eff}} < 0.004$ by DLS.

Fig. 5.16a shows the intensity autocorrelation functions for SP-2B at six temperatures between 17°C and 47°C with their respective KWW fits (Eq. 3.34). Here the scattered intensity has been detected at an angle of $2\theta = 90°$ leading to a wave vector transfer of $q = 0.018\,\mathrm{nm}^{-1}$. With increasing temperatures the g_2 functions shift towards shorter delay times τ which is associated to faster structural relaxations at the corresponding temperature. The result is typical for colloidal systems due to faster thermal motion and lower solvent viscosity for higher temperatures. For PNIPAm the speed-up is supported by a reduction of the particle volume with temperature. The relaxation times are shown

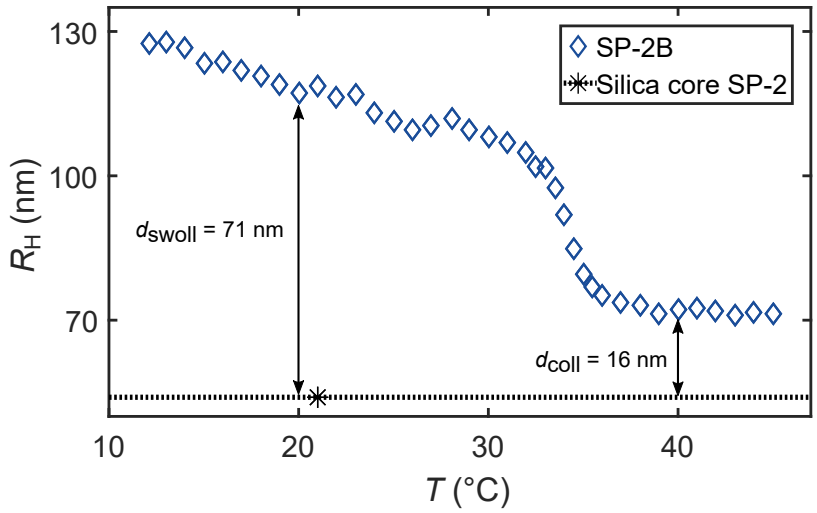

Figure 5.17: Temperature-dependent hydrodynamic radius R_H of Silica-PNIPAm sample SP-2B characterised by DLS.

in Fig. 5.16b (left axis) as a function of temperature. The temperature dependency is fitted by a linear decrease $\tau_c = a \cdot T + b$ yielding $a = -4.7 \cdot 10^{-5}$ s/°C and $b = 0.003$ s. The KWW exponent is constant $\gamma = 1$ over the whole temperature interval (Fig. 5.16b) which is the typical value for diffusive dynamics.

From the g_2 functions the temperature-dependent particle size and with that the deswelling behaviour was analysed between 15°C and 50°C. As representatively shown for sample SP-2B in Fig. 5.17, the radius starts to decrease upon heating before it rapidly collapses at $T = 32$°C, matching the literature value of the LCST [107]. For $T > 37$°C the shell is in the collapsed state and the particle size stays constant. In this hydrophobic state the hydrodynamic radius of the core-shell particles is about 70 nm while it is about 130 nm for the lowest temperature where the PNIPAm shell is completely swollen. The uncoated silica particles have as well been characterised by DLS and have a hydrodynamic radius of around 54 nm. This leads to a shell thickness of about 71 nm in the swollen state and 16 nm in the collapsed state. Passing the LCST the volume of a single SP-2B core-shell particle is thus reduced by 84%.

5.4.3 Dynamics of concentrated suspensions

For densely-packed systems interparticle interactions cannot be neglected and hence the particle motion differs from simple diffusion. The temperature-dependent dynamics of silica-PNIPAm suspensions have been investigated via XPCS at various concentrations and with varied PNIPAm core-to-shell ratios.

In Fig. 5.18 the intensity correlation functions are shown for SP-2B at $\Phi_{eff} = 0.55$ at all studied temperatures between 15°C and 45°C and at a selected q value of 0.02 nm^{-1} with the corresponding KWW fits (Eq. 3.34). All g_2 functions are normalised to the speckle contrast β. In this experiment at 8-ID the contrast was $\beta \approx 0.15$ (see Table 4.2). The g_2 functions obtained at a q value similar to the DLS measurement are slower than in

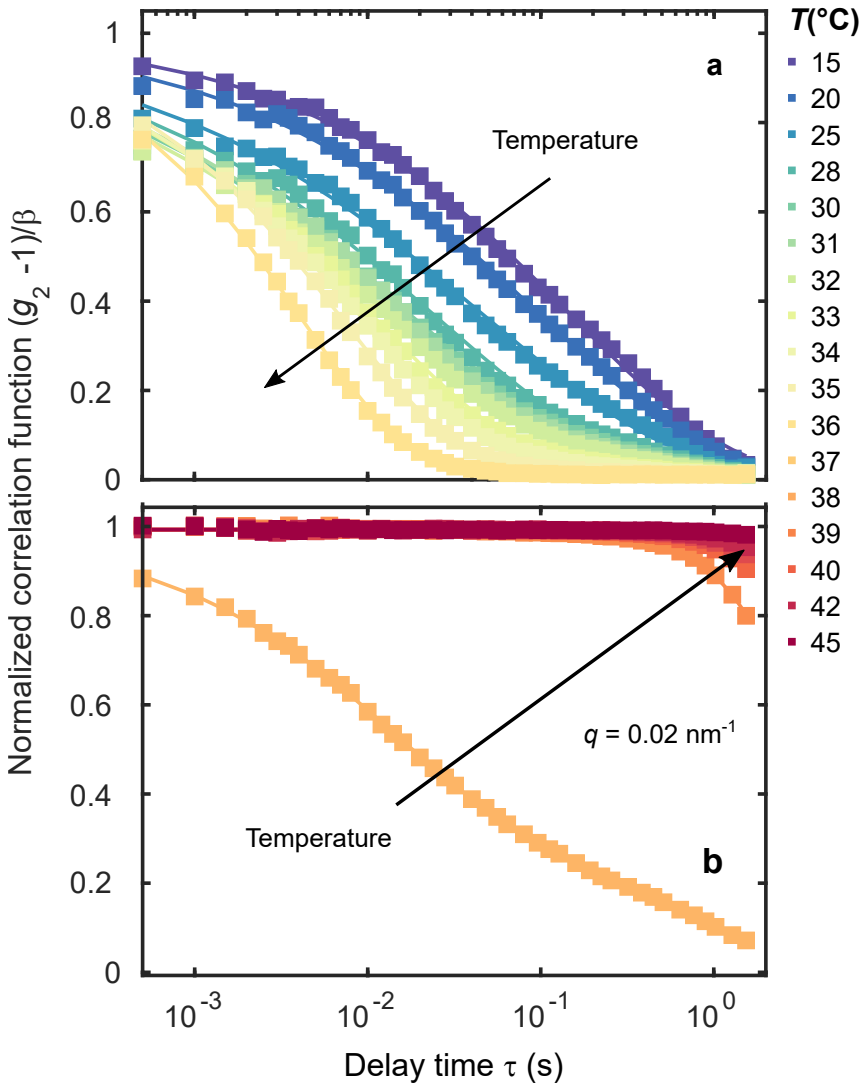

Figure 5.18: Temporal evolution of the correlation functions of SP-2B at $\Phi_{\text{eff}} = 0.55$ a) for temperatures between 15°C and 36°C where the system speeds up and b) between 37°C and 45°C where the system slows down. The increase of the temperature is indicated by the black arrow, respectively. The g_2 functions were calculated at $q = 0.02\,\text{nm}^{-1}$, the solid lines represent the KWW functions (Eq. 3.34).

Fig. 5.16a which is an effect of particle concentration. Upon heating until 36°C (Fig. 5.18a) the correlation functions shift towards shorter structural relaxation times. This implies faster dynamics of the particles towards higher temperatures as observed for the dilute case (Fig. 5.16). Interestingly for temperatures higher than 32°C also the slope changes, indicating a transition of dynamics in the system. At 37°C the system rapidly slows down shown by a jump of the correlation function towards larger times (Fig. 5.18b). Additionally the g_2 function shows two decays at 37°C, indicating a second dynamical process in the system. For this specific temperature the KWW model had to be extended to a double exponential:

$$\begin{aligned} g_2(\boldsymbol{q},\tau) &= 1 + (\beta - \alpha) \cdot \exp\left[-2(\Gamma_1(\boldsymbol{q}) \cdot \tau)^{\gamma_1}\right] \\ &\quad + \alpha \cdot \exp\left[-2(\Gamma_2(\boldsymbol{q}) \cdot \tau)^{\gamma_2}\right]. \end{aligned} \tag{5.4}$$

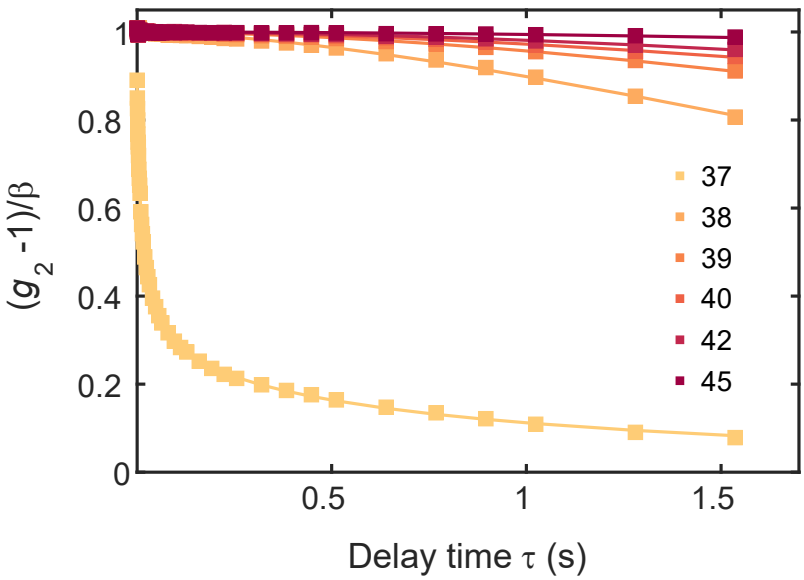

Figure 5.19: g_2 functions of SP-2B for $T > 37°C$ (comp. Fig. 5.18b) shown with a linear time axis.

At 38°C a further slowing down is observed in the g_2 function, which does not decorrelate completely within the total exposure time. The decorrelation of the g_2-function sets in at $\tau \approx 0.2\,s$ (see Fig. 5.19). Upon further heating up to 45°C the system continuously slows down further. In the total exposure time of 2 s no second relaxation process is observed for temperatures $T \geq 38°C$.

Fig. 5.20a shows all characteristic relaxation times obtained for SP-2B at $\Phi_{eff} = 0.55$ and $q = 0.02\,nm^{-1}$ from the g_2 functions displayed in Fig. 5.18. The studied temperature range can be divided into three regimes: In region A (blue) for $T < 32°C$ the relaxation time decreases monotonously from about 1 to 0.1 s. Between 32°C and 36°C, in region B (green), τ_c decreases rapidly from 0.1 to 0.01 s implying a speed-up of the particles. This temperature region B corresponds to the regime where the particles start to collapse (compare R_H in Fig. 5.17a). For $T = 37°C$, which was chosen to be the border between B and C, both τ_{c_1} and τ_{c_2} are plotted. Here τ_{c_2} (•) relates to a slowing down of several orders of magnitude, whereas τ_{c_1} (○) shows a parallel dynamical process comparable to the dynamics at $T = 34°C$. In region C (red) for $T > 37°C$ all τ_c are increased by several orders of magnitude compared to region B. In contrast to the plateau of strongly increased relaxation times typically seen for high packing fractions [108], here a tendency towards higher τ_c is observed with increasing T. Due to a decorrelation of the g_2 functions in regime C of about 20% to 2% (see Fig. 5.19) within the total exposure time of 2 s a KWW function with $\tau_c \approx 10\,s$ could be adapted. In this temperature regime C the particles in the dilute suspension were found to be fully collapsed as shown in Fig. 5.17.

The character of the dynamics is reflected in the q dependence of the g_2 functions which are shown in Fig. 5.21 for accessible q values at $T = 25°C$, 32°C, 37°C and 42°C. Dynamics at large length scales are slower and therefore g_2 functions of small q correspond to slower dynamics. This behaviour can be observed for all temperatures as shown representatively in Fig. 5.21. Fig. 5.22 compares the q dependency of the characteristic relaxation time

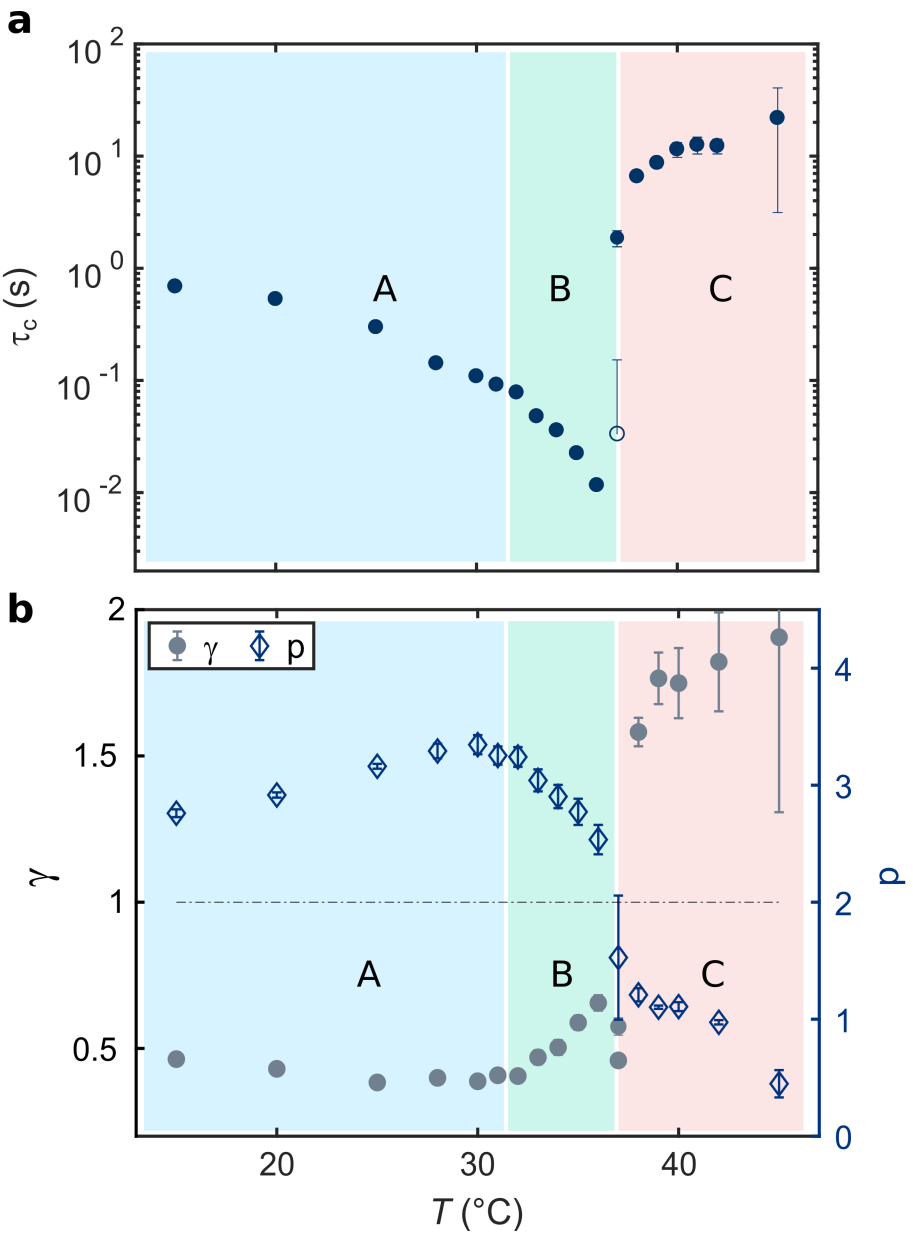

Figure 5.20: XPCS results of SP-2B: a) Temperature dependence of the characteristic relaxation time τ_c at $q = 0.02\,\mathrm{nm}^{-1}$. Between B and C at 37°C where the g_2 function shows two decays both τ_{c_1} (•) and τ_{c_2} (○) are shown. b) Temperature dependence of γ and q at $q = 0.02\,\mathrm{nm}^{-1}$ (the dashed line illustrates $\gamma = 1$ and $p = 2$ for simple diffusion). For $T = 37°\mathrm{C}$ γ_1 and γ_2 are shown while p pertains to $\tau_{c_2} = 1/\Gamma_2$.

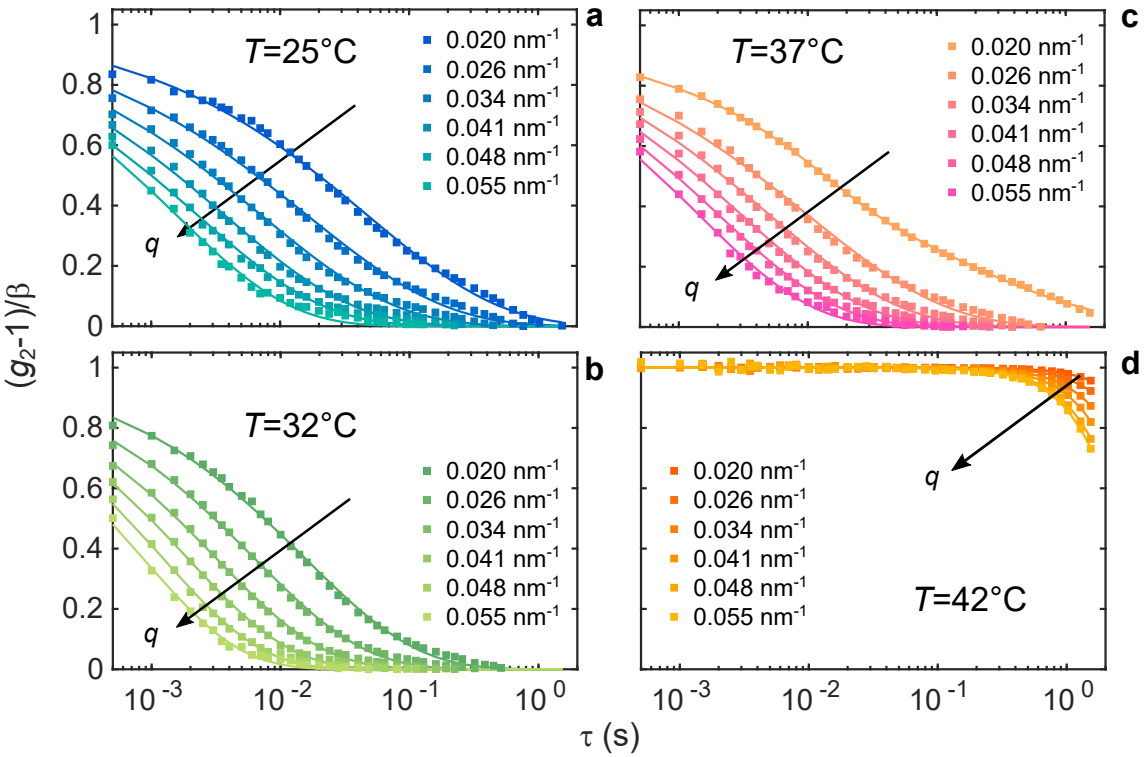

Figure 5.21: q dependent g_2 functions of SP-2B at $\Phi_{\text{eff}} = 0.55$ for a) $T = 25°\text{C}$, b) $T = 32°\text{C}$, c) $T = 37°\text{C}$ and d) $T = 42°\text{C}$.

and the KWW exponent for $T = 20°\text{C}$ and 42°C. Fig. 5.22a compares the development of τ_c for 20°C (blue, swollen particles) and 42°C (red, collapsed particles) as a function of wave vector transfer q. In either case τ_c shows a distinct q dependence. The solid lines represent fits of a power law $\tau_c \propto q^{-p}$ to the data. For $T = 20°\text{C}$ a value of $p \approx 3$ (here $p = 2.92 \pm 0.05$) was found suggesting an anomalous dynamical behaviour of the swollen particles. Fig. 5.20b shows that $2.8 < p < 3.4$ is found in the whole temperature regime A. The corresponding KWW exponent γ in temperature region A was found to be $\gamma \approx 0.5$ with no distinct q dependence (Fig. 5.22b).

For the collapsed particles at $T = 42°\text{C}$, $p \approx 1$ was found (here $p = 0.91 \pm 0.07$), indicating that a transition of dynamics must have occurred in the system upon heating. For this temperature and q value, the corresponding KWW exponent was found to be $\gamma \approx 1.8$. In contrast to regime A, γ shows a decay as a function of q. While the KWW exponent is $\gamma = 1.8$ at the lowest q probed here, it approaches $\gamma \approx 1.5$ with increasing q.

As with the structure factor (section 5.1), this temperature-induced slow-down of dynamics was studied as a function of concentration. The experiment was performed with sample SP-1 at $\Phi_{\text{eff}} = 0.12$, 0.15 and 0.19 at beamline ID10 at ESRF. Fig. 5.23 shows g_2 functions for all three concentrations during the heating process. Primarily, for all six temperatures, the correlation functions imply shorter structural relaxation times for lower concentrations of the silica-PNIPAm particles in the suspension. Smaller τ_c imply faster particle dynamics due to reduced interparticle interaction for lower concentrations. With increasing temperature from 25°C to 30°C and 32°C the g_2 function of each concentration shows successively faster dynamics. Above 36°C no further development towards faster

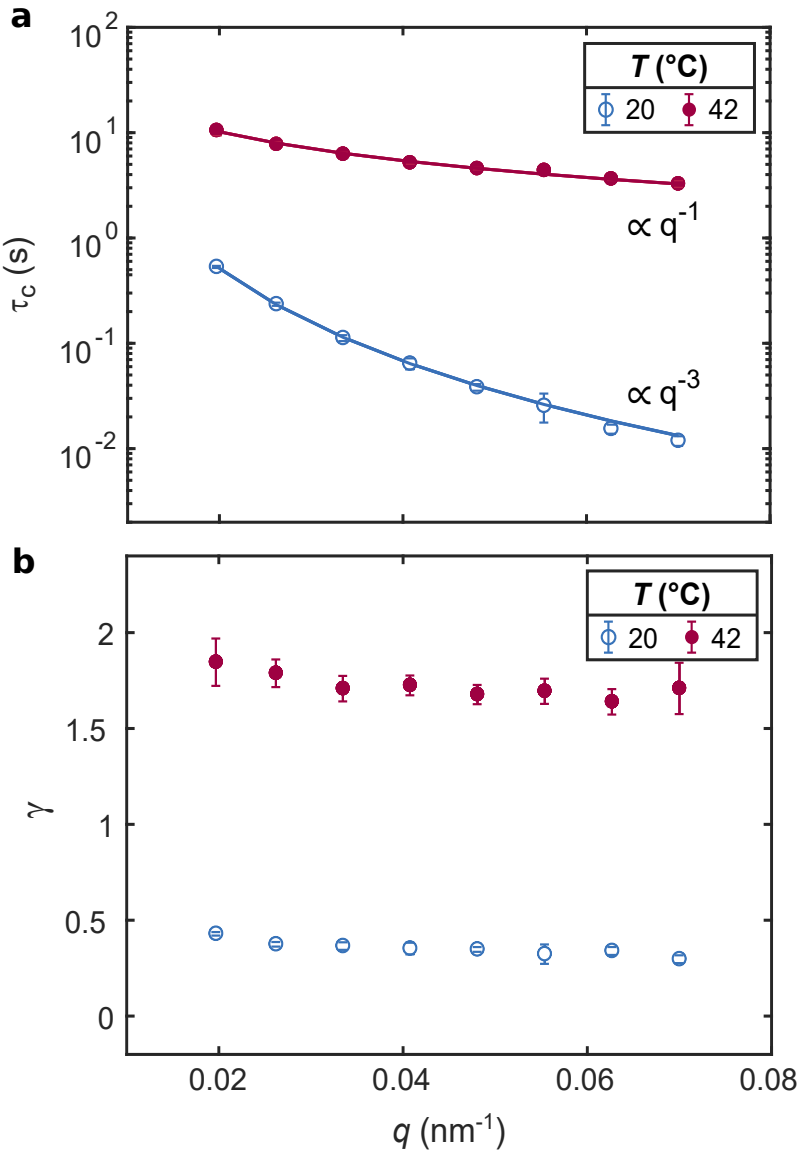

Figure 5.22: XPCS results of SP-2B: q dependence of a) τ_c and b) the KWW exponent γ for the swollen particles at 20°C (blue) and the collapsed particles at 42°C (red).

dynamics is present, however, the dynamical behaviour varies for each concentration upon further heating. While the g_2 functions of the system at $\Phi_{\text{eff}1} = 0.12$ remain unaffected and thus show no change of dynamics at $T = 36$°C, 38°C and 40°C, there is a clear slowing down present for $\Phi_{\text{eff}2}$ and $\Phi_{\text{eff}3}$. The medium concentrated solution with $\Phi_{\text{eff}2} = 0.15$ shows a continuous slowing down between 36°C and 40°C whereas a second relaxation process appears above 36°C. The KWW fit for those g_2 functions has been extended to a double exponential function (Eqn. 5.5). The pre-factor α is $\alpha = 0.21$ for 38°C and $\alpha = 0.19$ for 40°C. For both temperatures where two dynamical processes are found in the g_2 function, the faster relaxation process seems to remain constant. The slower process does not fully decorrelate within the studied time range but it nevertheless shows a further change while heating from 38°C to 40°C. At $T = 38$°C a clear decay is present whereas for 40°C the g_2 function does not decorrelate distinctly and hence just shows a plateau in

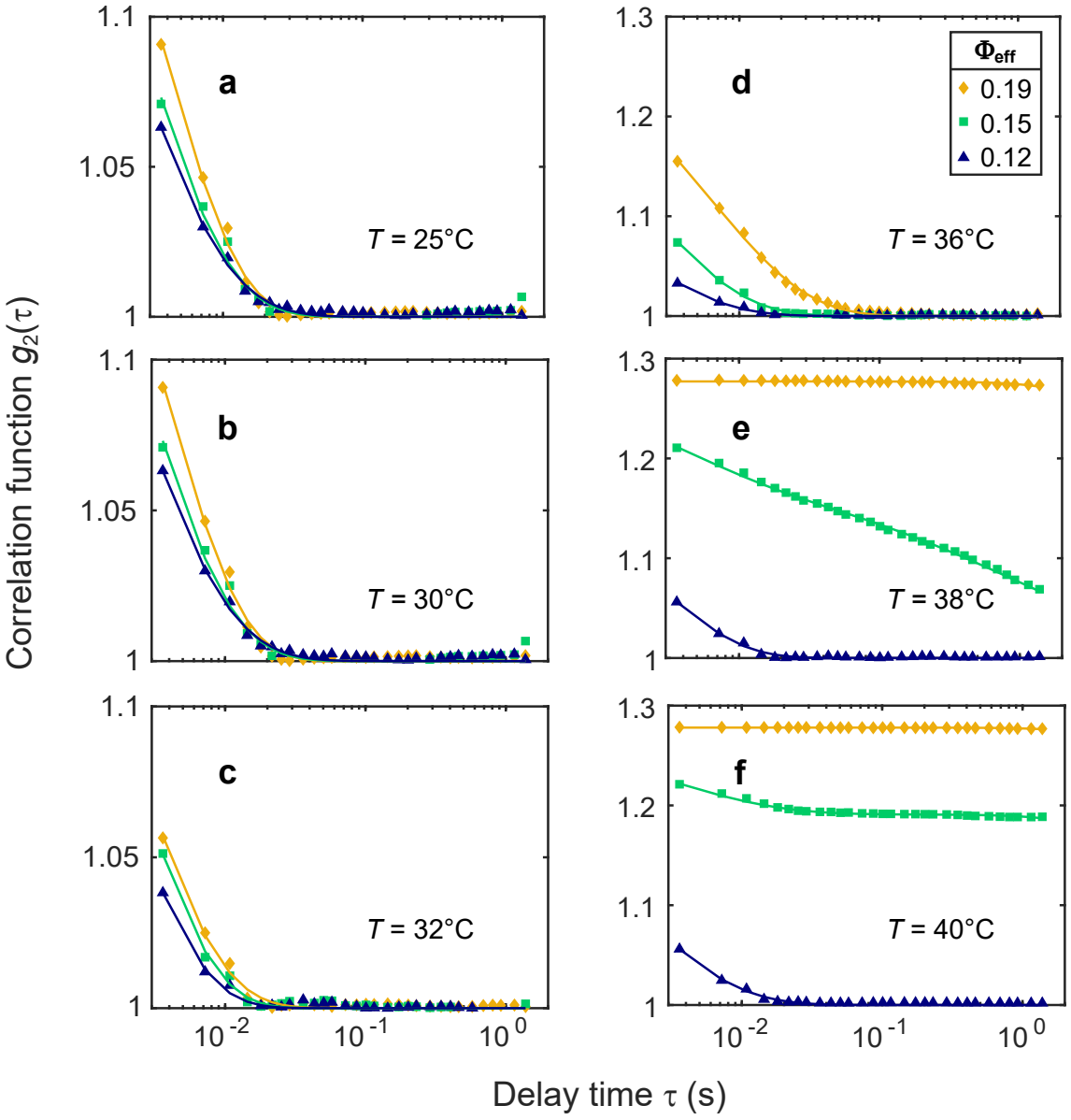

Figure 5.23: Temporal evolution of the correlation functions of SP-1 according to Fig. 5.3 measured for $\Phi_{\text{eff}1} = 0.12$ (blue ▲), $\Phi_{\text{eff}2} = 0.15$ (green ■) and $\Phi_{\text{eff}3} = 0.19$ (yellow ♦) at a) $T = 25°\text{C}$, b) $T = 30°\text{C}$, c) $T = 32°\text{C}$, d) $T = 36°\text{C}$, e) $T = 38°\text{C}$ and f) $T = 40°\text{C}$. The g_2 functions were calculated at $q = 0.02\,\text{nm}^{-1}$, the solid lines represent the calculated fits. The temperature steps correspond to Fig. 5.3.

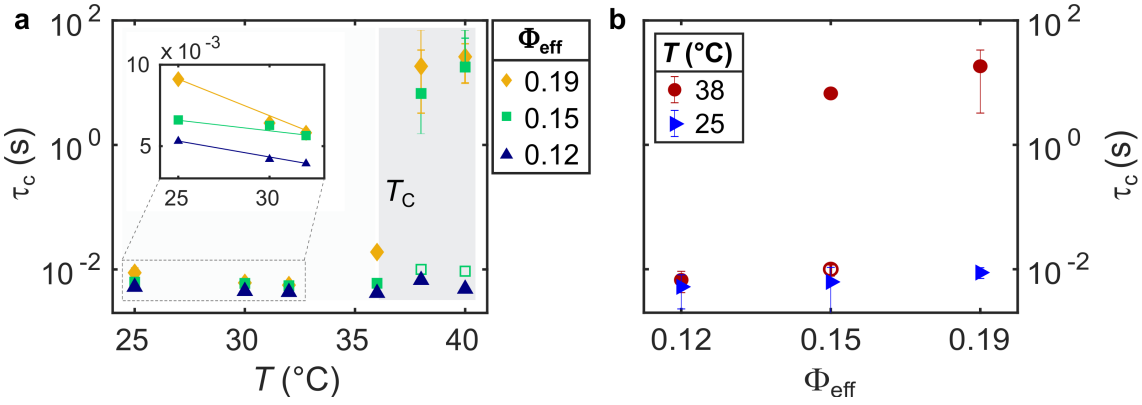

Figure 5.24: XPCS results of SP-1: a) Temperature dependence of the characteristic relaxation time τ_c at $\Phi_{eff1} = 0.12$ (blue ▲), $\Phi_{eff2} = 0.15$ (green ■/□, open symbols represent a second dynamical process at the respective temperature) and $\Phi_{eff3} = 0.19$ (yellow ♦). The inset depicts a zoom of region A whereas the solid lines are guides to the eye. b) Concentration dependence of τ_c of the swollen particle at 25°C (blue) and the collapsed particle at 38°C (red). All values correspond to the g_2 functions at $q = 0.02\,\mathrm{nm}^{-1}$ presented in Fig. 5.23.

the covered time range.

For the highest concentration Φ_{eff3}, the g_2 functions of 38°C and 40°C show no decorrelation within the total exposure time. Hence, the sample resembles a static system in the time range of 1.5 s. Analogous to the structural result from the SAXS data, the development of τ_c can be classified below and above the critical temperature $T_c \approx 36$°C: For T_c all relaxation times decrease linearly upon heating from 25°C to 32°C with larger relaxation times the higher the respective concentration (see inset Fig. 5.23a). Hence, the system speeds up for all concentrations upon heating from 25°C to 32°C. Therein, the initial relaxation time is proportional to the particle concentration. Upon further heating from 36°C to 40°C and hence for $T > T_c$, the dynamics shows a concentration-dependent behaviour. While τ_c remains constant for Φ_{eff1} (blue ▲), the system with Φ_{eff3} (yellow ♦) does not decorrelate in the total experimental time of 1.5 s for $T = 38$°C and 40°C. Hence, no relaxation time could be extracted, however, it increases several orders of magnitude compared to $T < T_c$.

Based on the previously discussed results on SP-2B a KWW function with a compressed exponent of $\gamma = 2$ has been applied for the g_2 functions which still decorrelate about 1% within 1.5 s. In case of the sample with Φ_{eff2}, the compressed exponent relates to the slower relaxation process. The relaxation times obtained from the modelled KWW functions are shown Fig. 5.23a (area B) with an errorbar covering the wide range of possible values. For the sample with Φ_{eff2} whose g_2 functions show two dynamical processes τ_c is split up in regime B. While τ_{c_1} (green □) coincides with the behaviour observed for Φ_{eff1}, τ_{c_2} (green ■) rising analogously to the highest concentration Φ_{eff3}. A different representation of the relation is shown in Fig. 5.24b with the relaxation time as a function of particle volume fraction Φ_{eff}. At 25°C the particles are swollen and τ_c hardly increases with concentration whereas it shows a strong increase at 38°C where the particles are collapsed.

5.4.4 Influence of the shell size on the dynamics

Similar to the analysis of the structural behaviour, the dynamics were studied while changing the effective volume fraction Φ_{eff} by variation of the PNIPAm shell sizes with a constant silica core. With the relation of shell to core size, the samples are classified via their softness ξ following [95, 96]. The here discussed samples are sample SP-2A with a softness of $\xi_{2A} \approx 0.41$, SP-2B with $\xi_{2B} \approx 1.31$ and SP-2C with $\xi_{2C} \approx 3$ calculated for the swollen state at 20°C (see Tab. 4.1)). Fig. 5.25 shows the g_2 functions of SP-2A with $\Phi_{\text{eff}}(\text{SP-2A}) = 0.13$, SP-2B with $\Phi_{\text{eff}}(\text{SP-2B}) = 0.55$ and SP-2C with $\Phi_{\text{eff}}(\text{SP-2C}) = 0.73$, relating to the $I(q)$ in Fig. 5.4.

The dynamics of all three samples first becomes faster with increasing temperature between 36°C and 38°C, until it rapidly slows down with further heating. Despite the common features the observed dynamics of each sample show different characteristics. Sample SP-2A (Fig. 5.25a) shows the fastest dynamics of all three samples within the total exposure time of 1 s. The g_2 functions show a KWW exponent of $\gamma \approx 1$ for all temperatures $T \leq 39$°C. The slowing down occurs for $T > 38$°C and proceeds with smaller temperature steps than observed earlier for larger shell sizes. At the same time a second relaxation process occurs for 40°C and 42°C before it does hardly show any time dependence at 45°C. In comparison, the correlation functions of SP-2B (Fig. 5.25b) with the medium shell size are found at larger times and hence related to slower particle motions than SP-2A.

Sample SP-2B has been discussed extensively in section 5.4.3. Sample SP-2C with the largest shell size of 186 nm shows the slowest dynamics of all three SP-2 samples (Fig. 5.25c). As with the the other samples, the g_2 functions show a speed up until 36°C followed by a rapid slow down until there is only a slight decorrelation for $40 - 45$°C where the shell is fully collapsed. In this third case the KWW exponent is found to be $\gamma \approx 0.5$.

The direct comparison of a-c hence clarifies the influence of the PNIPAm shell thickness on the dynamics in the system. Primarily, the particular set of g_2 functions for each sample was shifted to larger characteristic relaxation times with higher shell thickness. Furthermore, towards larger shell thicknesses the slope of the correlation functions changed from a single exponential decay with $\gamma = 1$ to a stretched exponential decay with $\gamma = 0.5$. Fig. 5.26a gives a closer insight in the overall behaviour of τ_c with increasing temperature for all three shell sizes. As before, the threshold temperature $T_c \approx 36$°C can be classified. For $T < T_c$, all three samples show a decrease of τ_c and hence a speed up in the system upon heating whereas slower dynamics are determined for larger shell sizes.

For $T > T_c$ the samples show a shell size dependent behaviour. For SP-2A the transition of dynamics happens between $T = 36$°C and $T = 38$°C where τ_c starts to increase until it raises more than four orders of magnitude at $T = 45$°C. For $T = 42$°C τ_{c1} and τ_{c2} of both relaxation processes are plotted in Fig. 5.26a.

Sample SP-2B, as discussed above, shows a further decrease of τ_c by 32% at 36°C. At 37°C the system slowed down and shows two dynamic processes with with $\tau_{c1} \approx 0.035$ s, matching with the relaxation time found for 34°C, and $\tau_{c2} \approx 6.4$ s increased by more than two orders of magnitude. Upon heating to 45°C τ_c shows a further tendency towards

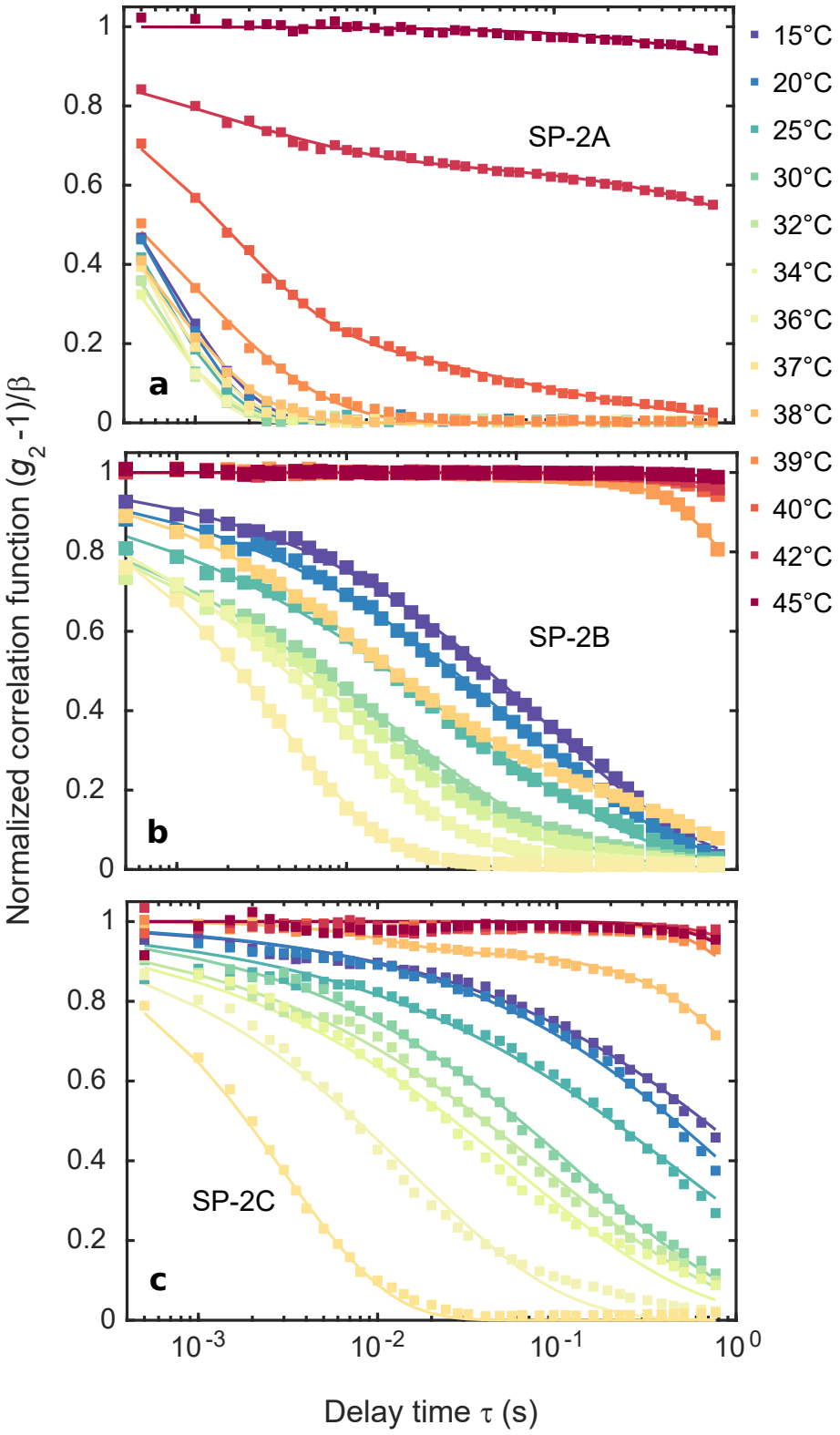

Figure 5.25: XPCS results of SP-2: Temperature dependent intensity autocorrelation functions g_2 at $q = 0.02\,\mathrm{nm}^1$ of SP-2 with a swollen PNIPAm shell thickness of a) 22 nm at $\Phi_{\mathrm{eff}}(\mathrm{SP\text{-}2A}) = 0.13$, b) 71 nm at $\Phi_{\mathrm{eff}}(\mathrm{SP\text{-}2B}) = 0.55$ and c) 186 nm at $\Phi_{\mathrm{eff}}(\mathrm{SP\text{-}2C}) = 0.73$.

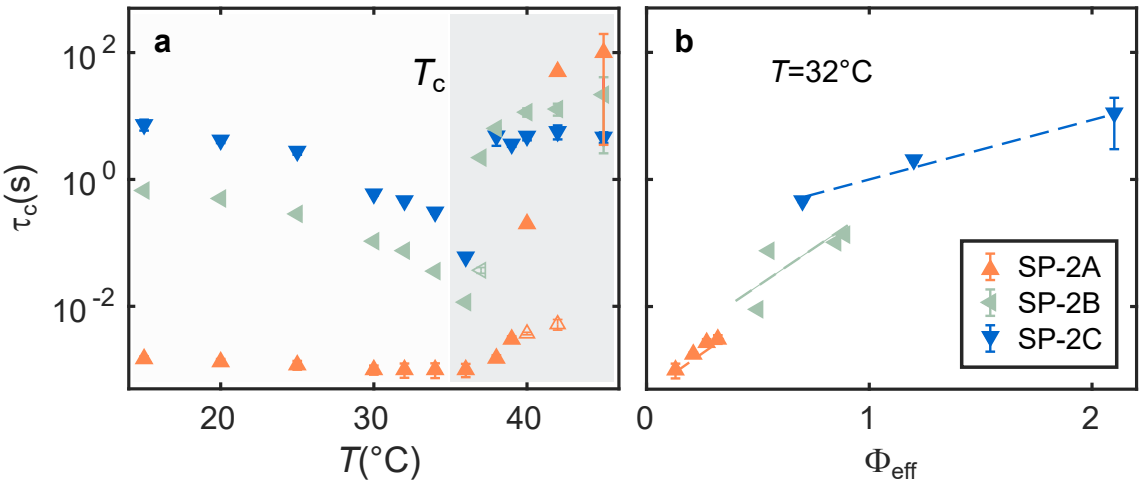

Figure 5.26: a) Temperature dependence of the characteristic relaxation time τ_c for SP-2A (orange ▲/△) with $\Phi_{eff} = 0.13$, SP-2B (pink ◀) with $\Phi_{eff} = 0.55$ and SP-2C (blue ▼) with $\Phi_{eff} = 0.73$. b) τ_c of various highly concentrated silica-PNIPAm suspensions of SP-2A, SP-2B and SP-2C. All parameters correspond to the g_2 functions obtained at $q = 0.02\,\mathrm{nm}^{-1}$ shown in Fig. 5.25, dashed lines represent guides to the eye.

larger times. SP-2C initially shows a decrease of τ_c to 0.06 s at 36°C before it rises and stays constant around 4.9 s for $T \geq 38$°C which is in the same order of magnitude as the values obtained at low temperatures. Here it clearly differs from both SP-2A and SP-2B whose characteristic relaxation times increase by several orders of magnitude for $T > T_c$. Nevertheless the g_2 functions of all samples are found at similar time-scales.

Additionally, the dependence of τ_c on both shell size and concentration was analysed. Fig. 5.26b shows τ_c of SP-2A, SP-2B and SP-2C at various Φ_{eff} obtained at $T = 32$°C all for $q = 0.02\,\mathrm{nm}^{-1}$. For sample SP-2C with the largest shell thickness, large packing fractions lead to over-packed systems with an effective volume fraction of $\Phi_{eff} > 1$.

5.4.5 Ultra-small-angle X-Ray photon correlation spectroscopy

The performance of XPCS in ultra-small-angle X-Ray scattering geometry (USA-XPCS) enables the study of the dynamics in the system on a length scale of the next-neighbour distance between the particles. In the SAXS data (section 5.1), sample SP-3B showed a pronounced structure factor (see Fig. 3.7, 5.8 and 5.9). Due to the large deformable shell, an over-packed effective volume fraction of $\Phi_{eff} = 1.35$ was reached for SP-3B. Fig: 5.27 shows the g_2 functions of SP-3B for this Φ_{eff} at the accessible q values around q_{max} for a) T = 20°C, b) 36°C and c) 45°C. Therein, $q = 0.012\,\mathrm{nm}^{-1}$ is the lowest q value where a g_2 function was calculated. The lines represent the corresponding KWW fits. Due to the very high sample concentration, the dynamics are slow and hence the measurements have been performed with a total exposure time of 23 s whereas the maximum dose was kept constant by means of attenuators. As seen for the previously discussed samples, the g_2 functions show faster dynamics upon heating from $T = 20$°C to 36°C and a slowing down again upon further heating to 45°C, all for a constant q. Fig. 5.28a shows the q dependency of τ_c for $T = 20$°C and 42°C, whereas the solid lines represent fits of a power law $\tau_c \propto q^{-p}$.

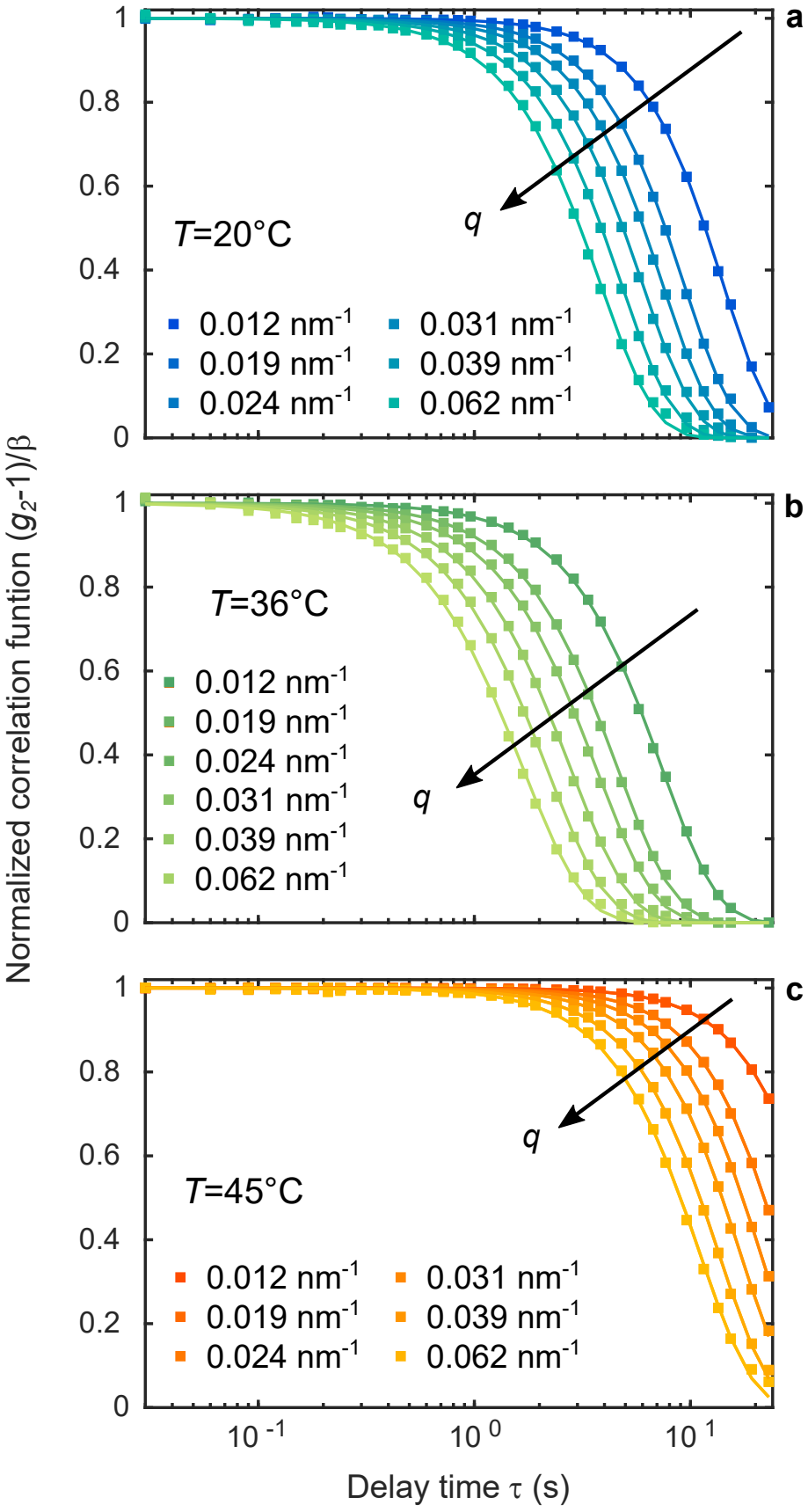

Figure 5.27: USA-XPCS results of SP-3B at $\Phi_{\text{eff}} = 1.35$: q dependent intensity correlation functions g_2 at a) T = 20°C, b) 36°C and c) 45°C.

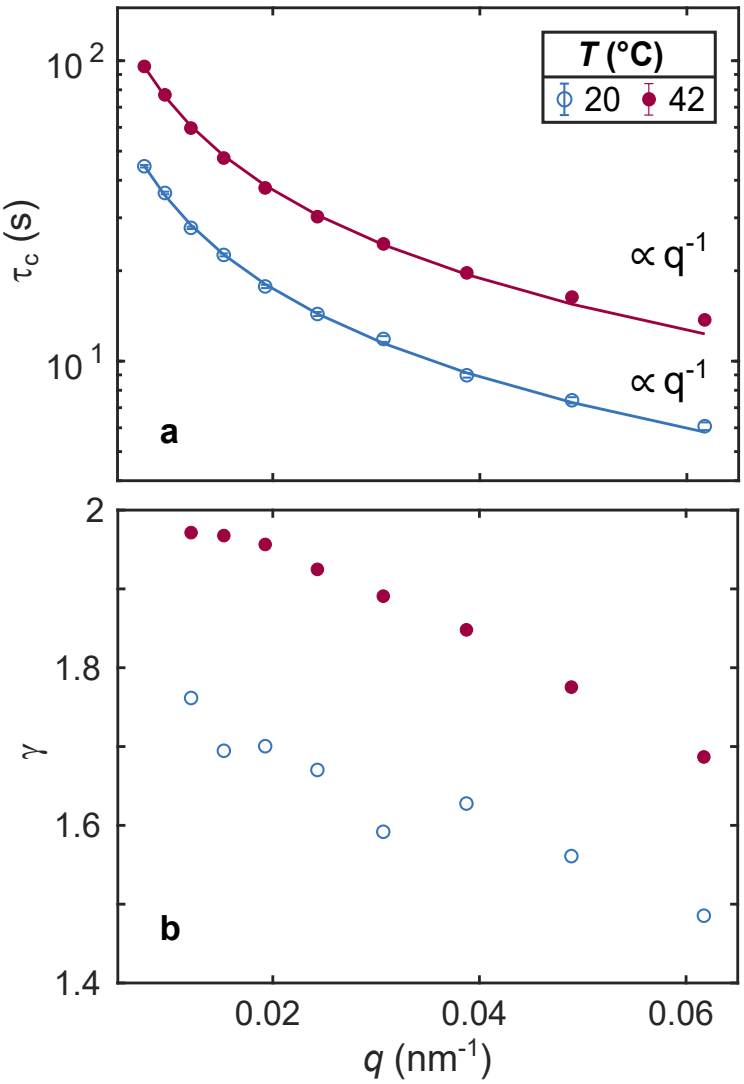

Figure 5.28: q dependency of a) characteristic relaxation time τ_c and b) KWW exponent γ, both corresponding to SP-3B with $\Phi_{\text{eff}} = 1.35$ at $T = 20°\text{C}$ and 42°C. The solid lines in a) represent a power law fit to the data with $\tau_c \propto q^{-p}$.

Interestingly, for both $T < T_c$ and $T > T_c$ a value of $p \approx 1$ (here $p = 0.98 \pm 0.01$) was found in contrast to the previous result where this dependency was found only for $T > T_c$ (see. Fig. 5.22). The KWW exponent, shown as a function of q in Fig. 5.28b, is found to be $\gamma > 1$ for all temperatures, indicating a compressed exponential decay of the g_2 functions. Here, γ decays as a function of q from 1.76 at $q = 0.012\,\text{nm}^{-1}$ to 1.49 at $q = 0.062\,\text{nm}^{-1}$ for 20°C and from 1.97 at $q = 0.012$ to 1.69 at $q = 0.012$ for 42°C, respectively, similar to sample SP-2B in Fig. 5.22. Despite the high volume fraction and the pronounced structure factor, the sample shows no indications of De-Gennes narrowing [109].

5.4.6 Reversibility

To study the reversibility of the de-swelling behaviour of the particles and the transition of dynamics present in highly concentrated silica-PNIPAm systems, DLS and XPCS measurements have been performed both upon heating from 25°C to 45°C and with sub-

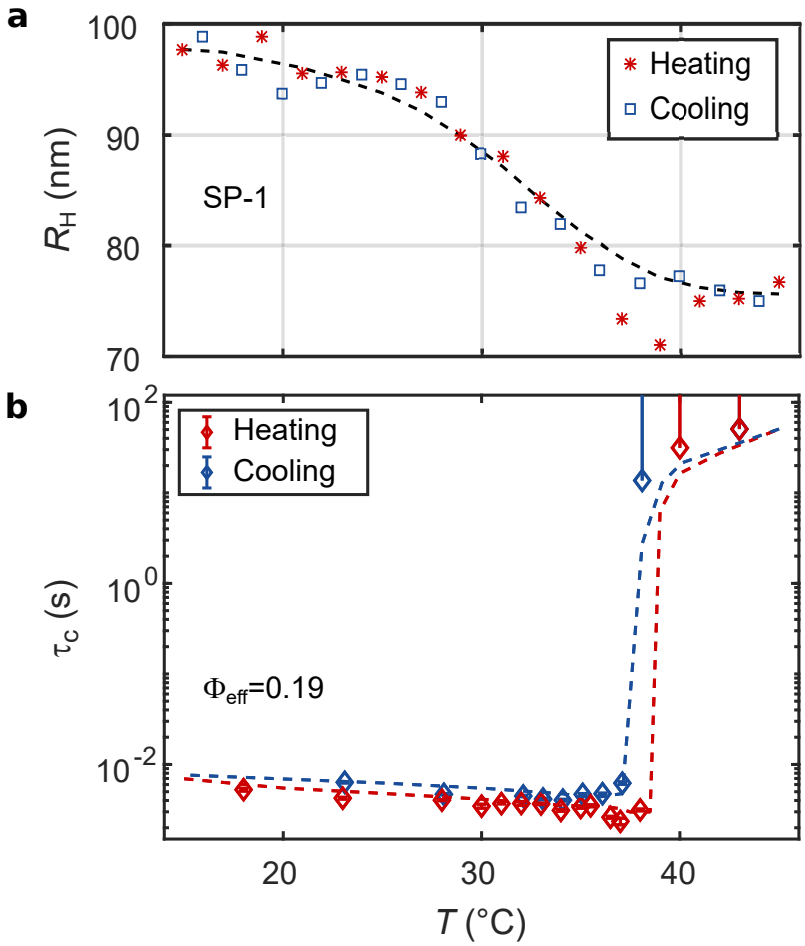

Figure 5.29: Temperature dependence of a) the hydrodynamic radius R_H of SP-1 characterized by DLS upon heating (red $*$) and cooling (blue $\square$), b) τ_c of SP-1 at $\Phi_{eff} = 0.19$.

sequent stepwise cooling down to 25°C. Fig. 5.29a shows the hydrodynamic radius of SP-1 as a function of temperature obtained by DLS. As described in section 5.4.2, the particles collapse from an initial $R_H \approx 100\,\text{nm}$ at 15°C to $R_H \approx 75\,\text{nm}$ at 45°C while crossing the LCST. The subsequent cooling reverses the behaviour whereby the radius increases. The de-swelling and swelling processes match each other without indications of a hysteresis which shows that the temperature-induced modification of hydrophilicity of the PNIPAm shell is completely reversible as shown in [62].

The reversibility of the transition of dynamics in highly concentrated systems was determined with sample system SP-1 at $\Phi_{eff} = 0.19$ in a separate temperature dependent XPCS experiment. Fig. 5.29b shows the overall behaviour of the characteristic relaxation time upon heating and cooling. To obtain representative results of τ_c in the slow regime at high temperatures the XPCS measurements have been additionally performed with an exposure time of 5 ms and a series of 2000 diffraction patterns keeping the same dose by using attenuators. With the total exposure time of 10 s and the result from the previous studies a KWW function with $\gamma \approx 2$ was adapted to the data at high T. The result shows an accelerating τ_c between 15°C and 37°C before the value rises by three orders of

magnitude as previously observed and shown in Fig. 5.24a. The cooling process shows a reversed behaviour with a drop of τ_c. In contrast to the dilute case (Fig. 5.29a) a small hysteresis can be identified between 38°C and 40°C. The comparison of Fig. 5.29a and b clarifies the occurrence of the transition of dynamics once the PNIPAm shell is collapsed at $T_c \approx 36$°C.

5.5 Dynamical influence of TMAO as co-solvent

The influence of TMAO on the dynamic temperature-dependence has been studied for sample SP-1, as with the static behaviour discussed in section 5.2. Therefore sample SP-1 has been prepared at $\Phi_{eff} = 0.095$ purely and with 0.11 M, 0.26 M and 0.52 M TMAO in the solution. Fig. 5.30 shows the associated g_2 functions at temperatures between 20°C and 45°C and $q = 0.023\,\mathrm{nm}^{-1}$. The g_2 functions of the pure silica-PNIPAm sample show a speed-up upon heating until $T = 40$°C before it slows down at $T_c = 42$°C (Fig. 5.30a). The higher T_c compared to SP-1 in section 5.4.3 is attributed to lower particle concentration. For the 0.11 M TMAO sample the g_2 functions also show faster dynamics upon heating with a slow down which is observed at 37°C (Fig. 5.30b). For 0.26 M TMAO an analogue behaviour is seen with $T_c = 34$°C and hence a further shift to lower temperatures (Fig. 5.30c). For temperatures $T < 35$°C TMAO has no significant influence on the g_2 functions shown in Fig. 5.30a-c. The sample with 0.52 M TMAO shows a different

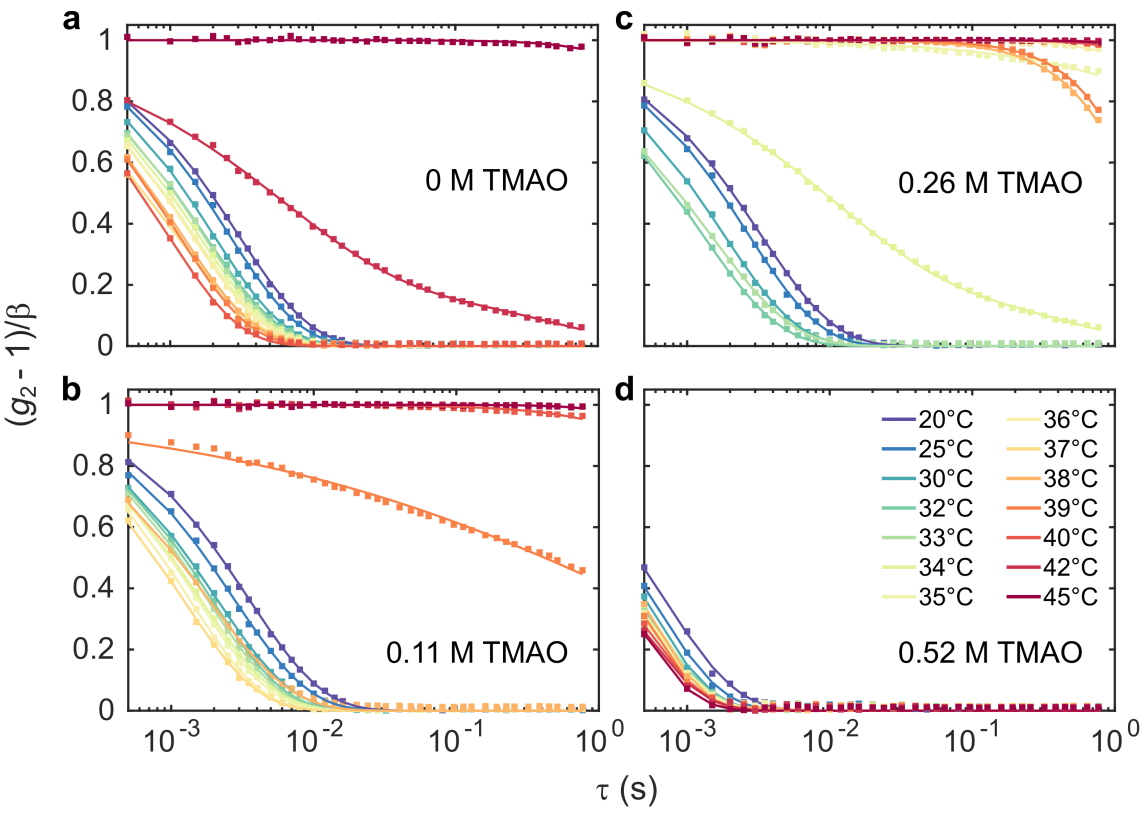

Figure 5.30: Intensity correlation functions g_2 of a) SP-1 at $\Phi_{eff} = 0.095$ for $q = 0.023\,\mathrm{nm}^{-1}$ in pure water and b)-d) with addition of 0.11, 0.26 and 1 M TMAO, all with their corresponding KWW fit. The measurements were performed between 20°C and 45°C.

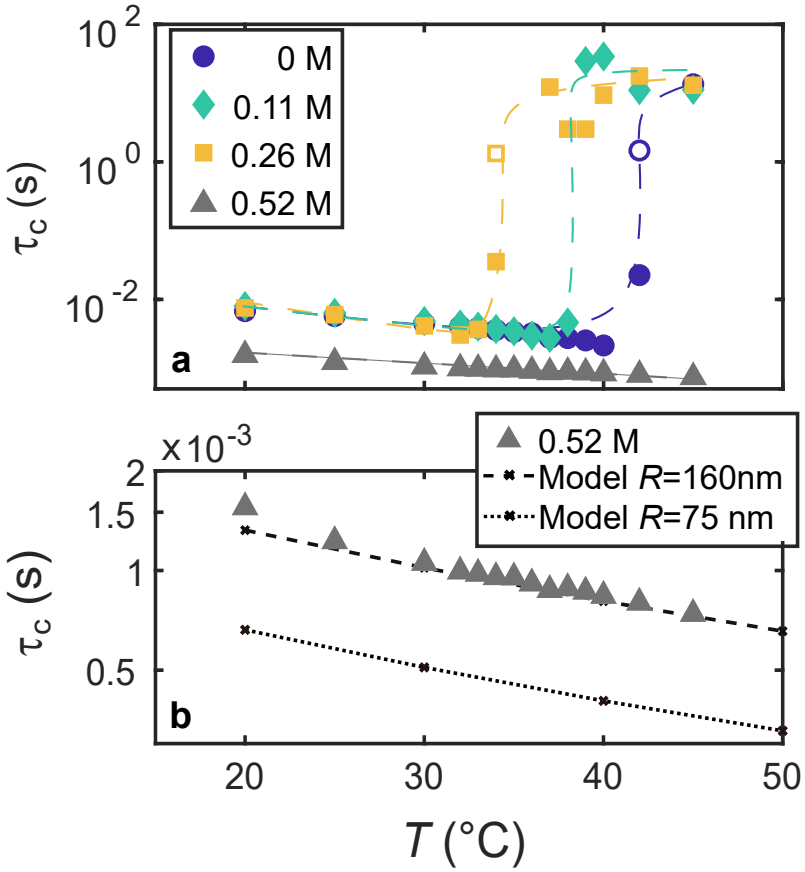

Figure 5.31: a) Temperature-dependence of the characteristic relaxation time τ_c of SP-1 at $\Phi_{eff} = 0.0095$ in water and with addition of 0.11, 0.26 and 0.52 M TMAO obtained at $q = 0.023\,\mathrm{nm}^{-1}$. Open symbols represent τ_{c2} corresponding to the second decay of the g_2 function for this concentration and temperature. The dashed lines represent guides to the eye. b) Temperature-dependence of τ_c for 0.52 M and the calculated τ_c for a diffusive aqueous system of spherical particles with a radius of $R = 160\,\mathrm{nm}$ (dashed line) and $R = 75\,\mathrm{nm}$ (dotted line).

behaviour (Fig. 5.30d). Here, all g_2 functions are shifted to smaller relaxation times, indicating faster dynamics than in the systems in Fig. 5.30a-c. Furthermore, the g_2 functions show a tendency to faster dynamics upon heating but no temperature-induced transition of dynamics.

Fig. 5.31a shows the characteristic relaxation times of all four samples as a function of temperature. All relaxation times of the 0 M, 0.11 M and 0.26 M TMAO samples decrease monotonously and match each other for all respective $T < T_c$ with an initial relaxation time of $\tau_c = 7.5\,\mathrm{ms}$. Thus, for those systems, TMAO has an influence on T_c which is shifted to smaller T with higher concentrations of TMAO whereas the nature of the dynamics is unaffected. For the 0.52 M sample, τ_c decreases monotonously upon heating for the whole temperature range with an initial relaxation time of $\tau_c = 1.5\,\mathrm{ms}$. In Fig. 5.31b τ_c of the 0.52 M TMAO sample is shown together with the calculated temperature dependent τ_c of a diffusive aqueous system of spherical particles with a radius of 75 nm, in agreement with the collapsed radius of SP-1 (see Table 4.1). Irrespective of an offset in τ_c, the course of the data matches the calculation. To match the data without offset, the calculated radius

of the diffusive particles would be 160 nm.

5.6 Interpretation and discussion of the dynamical properties

The dynamics of silica-PNIPAm core-shell particles were studied as a function of temperature, concentration and shell thickness via XPCS and USA-XPCS. The g_2 functions of SP-2B at $\Phi_{\text{eff}} = 0.55$ in section 5.4.3 showed a speed-up of dynamics, followed by a slowing down with increasing temperature wherein a double exponential decay at $T = 37°\text{C}$ points out a second dynamical process in the system. Two relaxation processes are usually present in glass formers or supercooled liquids [110–112] and during gel formation [85,113]. By evaluation of the g_2 functions three temperature regimes could be classified. In regime A, for $T <$LCST, the characteristic relaxation time τ_c decreases monotonously upon heating and hence the system speeds up. In the intermediate regime B, for LCST$< T < 37°\text{C}$, which is the regime where the particles collapse, τ_c decreases rapidly. In regime C for $T \geq 37°\text{C}$ the relaxation time τ_c increases several orders of magnitude pointing out a transition of dynamics between B and C.

From the g_2 functions a distinct q dependence of the corresponding τ_c was extracted. For regime A an anomalous dependency of $\tau_c \propto q^{-3}$ was found. While simple Brownian motion where $\tau_c = 1/Dq^2$ leads to the mean-squared displacement of the particle $\langle \Delta r^2(t) \rangle \propto t^a$ with $a = 1$, the relation $\tau_c \propto q^{-3}$ can be associated with $a = \frac{2}{3}$ [77]. A mean-squared displacement with $a < 1$ relates to sub-diffusive particle motion [74, 75]. A scaling of $\tau_c \propto q^{-3}$ has been observed for colloids in a polymer matrix [74] where the dynamics of the colloid is linked to the motion of the surrounding polymer chains. Polymer dynamics with the observed q^{-3} dependence of τ_c and a mean-squared displacement of $t^{2/3}$ have been interpreted as a characteristics of membrane-like polymers following the Zimm model [77–80]. This result suggests polymer-dominated dynamics below the LCST. Here, this is attributed to the swollen PNIPAm shells functioning as a polymer matrix. Silica cores can be associated as tracer particles with their motion coupled to the Zimm-like relaxation of the polymer chains in the surrounding network.

The KWW exponent γ in region A was found to be $\gamma \approx 0.5$. This stretched and thus slower than exponential decay of the correlation function suggests an anomalous, sub-diffusive motion of the particles [74,75,81]. It further may indicate dynamical heterogeneity with the presence of multiple structural relaxation processes in the system [82]. Passing the LCST the DLS data in regime B shows a rapid decrease of the particle radius until it is fully collapsed.

For the collapsed particles in regime C $\tau_c \propto q^{-1}$ and $\gamma = 1.8$ was found for $T = 42°\text{C}$. In contrast to regime A, γ decays with increasing q. The appearance of $\gamma > 1$ together with the q^{-1} relation can be attributed to ballistic, hyper-diffusive motion often reported for jammed non-diffusive soft materials such as colloidal gels, concentrated emulsions and glasses [83–91]. A similar trend has been described for soft glassy gels where the KWW exponent is predicted to be 1.5 for $q \to 0$ and $\gamma = 1.25$ for $q \to \infty$ [88, 90]. The proposed microscopical explanation for this type of dynamics observed for γ and p are random

micro-collapses of the colloidal gel. The particles strive for a dense packing by local reconstruction of the gel which results in a strain field and thus a movement of other surrounding particles. The observed dynamics in regime C agree with the dynamics in PNIPAm hydrogels where $\tau_c \propto q^{-1}$ and $\gamma > 1$ were found for temperatures both below and above the LCST [14, 114]. Together with the $I(q)$ where the appearance of attractive forces is observed at temperatures of regime C, the results point towards the formation of a colloidal gel once the PNIPAm shell is fully collapsed.

The transition of dynamics at a critical temperature $T_c \approx 36°C - 37°C$ as well as the appearance of a second relaxation process is interpreted as an effect of high particle concentration. Both effects are more pronounced for dense particle packings and influence the dynamics leading to the transition of dynamics with a characteristic relaxation time in the range of $\tau_c \approx 10\,s$. While the static analysis showed a transition from repulsive to attractive forces at high temperatures for all concentrations the respective evolution of dynamics towards high temperatures clearly shows different states. With the ability of soft nanogel particles to overlap and to deform in densely packed assemblies [44], agglomerations due to the collapsed shells are favoured. Furthermore, the appearing interparticle attraction fosters the formation of colloidal gels [85]. Both effects intensify with concentration and hence influence the dynamics accordingly. The results match the SAXS result in this regime, where indications of a sticky hard sphere behaviour has been observed in the system as it has been also described by [115–117].

Additionally, the PNIPAm shell thickness has a clear influence on particle motion before the change of dynamic occurs. The particles with a shell thickness of 10 nm and $\Phi_{eff} = 0.13$ show diffusive behaviour with the KWW exponent of $\gamma = 1$. For thicker shells and higher Φ_{eff} the g_2 functions become stretched pointing out sub-diffusive dynamics with $\gamma < 1$. Here, the critical transition temperature T_c is independent of the PNIPAm shell size. For the sample with the thinnest shell the process of the transition of dynamics occurs over a wide range of temperature steps between 36°C and 42°C whereas larger shells show a sudden slowing down within the temperature step of 1°C. The alluded temperature-dependent transition of structure and dynamics in highly concentrated systems as well as the particle size was demonstrated to be fully reversible with increase and subsequent reduction of the temperature in a broad range around the LCST. Within this a small hysteresis of dynamics has been found for concentrated systems.

The study of highly over-packed systems with $\Phi_{eff} > 1$ [18, 44] shows hyper-diffusive, ballistic motion with $\tau \propto q^{-1}$ and $\gamma > 1$ for temperatures below and above the LCST. The corresponding USAXS results indicate a transition from repulsive to attractive forces in the system upon heating with a pronounced structure factor peak for $T < T_c$ (see section 5.1.4). This suggests a jammed but well-ordered system for swollen over-packed silica-PNIPAm particles at low T whose dynamics are restricted due to deformation and inter-penetration of the PNIPAm-shells. It is noted, that over-packing of silica-PNIPAm systems leads to dynamics of a colloidal gel for particles in both the swollen and the collapsed state [46].

Both the $I(q)$ and the dynamics data show that an increase of TMAO concentration

on a densely-packed silica-PNIPAm system decreases the transition temperature T_c and eventually leads to a temperature-independently collapsed system with no thermo-response of structure and dynamics. The effect is not present in dilute PNIPAm suspensions [53] despite much higher TMAO concentrations. It can therefore be addressed to the dense particle packing and the lack of available water molecules for both TMAO and PNIPAm.

The preferential hydrogen bonding between water and TMAO reduces the number of hydrogen bonds between polymer and water molecules and therewith stabilizes the globular state of PNIPAm [53–55]. Thus TMAO decreases the LCST and accompanying with that the transition temperature T_c in densely-packed systems as observed for the SP-1 suspension with 0.11 M and 0.26 M TMAO. On the contrary, for the 0.52 M suspension, the result suggests a particle system with temperature-independently collapsed PNIPAm shell, with a diffusive-like temperature dependence of the relaxation time. In densely-packed silica-PNIPAm systems, a large amount of the water is in the swollen PNIPAm shells. Due to the high TMAO concentration water molecules are expelled from the polymer leading to a lack of water for PNIPAm which consequently collapses.

5.7 The phase diagram of silica-PNIPAm

All the previously discussed data can be assembled in a phase diagram of Silica-PNIPAm as a function of temperature and concentration in the representation of the effective volume fraction Φ_{eff} calculated at 20°C (Fig. 5.32). The phase diagram is shown for volume

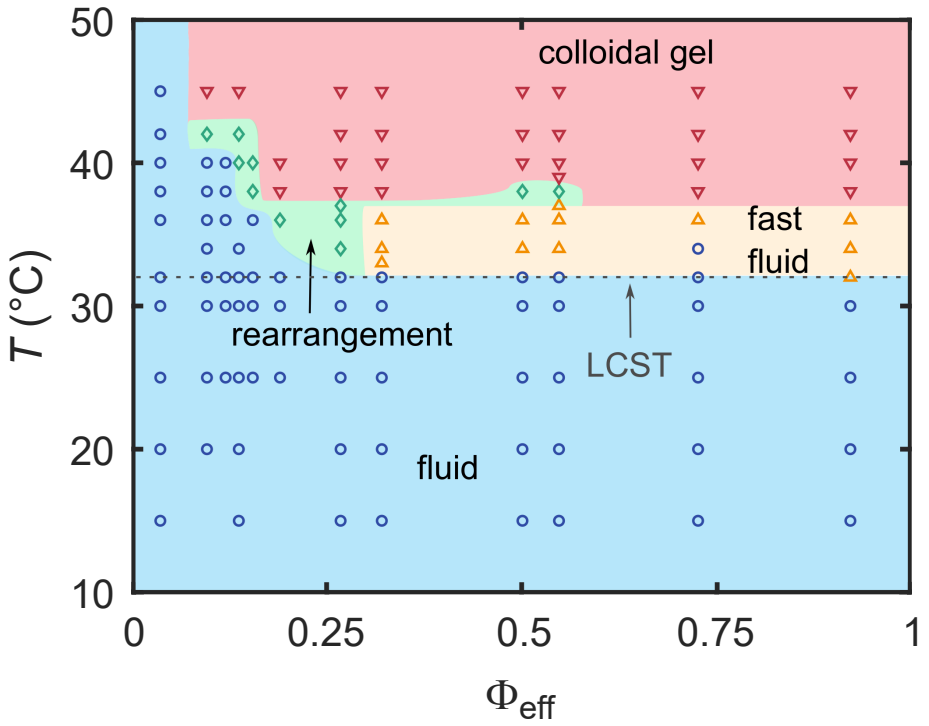

Figure 5.32: Phase diagram of silica-PNIPAm in the effective volume fraction Φ_{eff}-Temperature T representation for $\Phi_{\text{eff}} \leq 1$. Each symbol represents a performed SAXS and XPCS measurement. The blue circles (○) denote the region where the system behaves like a fluid. In the green region (◇) the g_2 functions show two relaxation processes associated with a structural rearrangement in the system. The neighbouring orange regime (△) relates to a rapid speed up of the particles. In the red regime (▽) the particles form a colloidal gel. The horizontal dashed line indicates the LCST at 32°C.

fractions $\Phi_{\text{eff}} \leq 1$. Based on all results four different phases were found:

1. A **fluid** phase for $T <$ LCST as well as for low Φ_{eff} where the dynamics show a monotonous speed-up with increasing temperature mainly driven by thermal motion and decrease of the particle radius. The g_2 functions show diffusive dynamics with $\gamma \approx 1$ for dilute suspensions and subdiffusive dynamics with $\gamma \approx 0.5$ at higher concentrations. The $I(q)$ show no temperature dependence in this regime. Systems with very low Φ_{eff} remain in this phase independent of temperature.

2. A **fast fluid** phase for medium to high Φ_{eff} and LCST $< T < T_{\text{c}}$. Here, τ_{c} decreases rapidly compared to the fluid phase. With increasing temperature the value of γ increases with $0.5 < \gamma < 1$. The $I(q)$ are still temperature-independent in this regime.

3. A **rearrangement** phase for medium concentrations and $T \approx T_{\text{c}}$. Here, the g_2 func-

tions show two relaxation processes whereas the overall dynamics is slower compared to the liquid phases. The $I(q)$ show indications of the appearance of attractive forces in the system.

4. A **colloidal gel** phase at high temperatures $T > T_c$. Here, τ_c increases several orders of magnitude compared to the fluid phases and the system shows the dynamics of a colloidal gel with $\gamma > 1$. In this regime the $I(q)$ suggest stronger attraction with increasing temperature.

The fluid phase (blue $\circ$) was found to be dominating where the colloidal suspension behaves like a liquid, showing a decrease of τ_c towards higher temperatures and lower concentrations. Dilute suspensions as SP-1 at $\Phi_{\text{eff}} = 0.035$ remain in this phase independent of temperature. At $T > 32°\text{C}$ a phase boundary occurs for $\Phi_{\text{eff}} \gtrsim 0.1$. Whereas the medium concentrations such as SP-1 at $\Phi_{\text{eff}} = 0.15$, SP-2A and SP-2B show a structural rearrangement expressed by a slow down accompanied with a second relaxation process (green $\diamond$), all $\Phi_{\text{eff}} \geq 0.32$ show a further rapid increase of τ_c up to $T \approx 36°\text{C}$ (orange $\triangle$). In the high-temperature regime (red $\bigtriangledown$) all $\Phi_{\text{eff}} \gtrsim 0.1$ slowed down by several orders of magnitude and show the dynamics of a colloidal gel as discussed for SP-1 at 0.19 and SP-2B in section 5.4.3. The phase diagram clarifies the possibility to achieve a transition from a liquid to a colloidal gel phase within one heating process. In contrast to the observation of a transition in PNIPAm microgels from a jammed glassy to a fluid state by heating up to the LCST [48] all here presented systems behave like a fluid in the regime of $T <$ LCST and have no indications for jamming or crystallization related to a critical packing fraction as in [41, 118–120]. Crystallization might be suppressed due to dispersity or too low cross-linking and hence low stiffness of the particles. Further, for this thesis, all samples were prepared freshly before the measurement whereas crystalline samples are usually given an equilibration time of up to several weeks [41].

6 Conclusion and Outlook

The temperature-dependent structure and dynamics of silica-PNIPAm core-shell nanoparticles have been determined via Dynamic Light Scattering (DLS), Small Angle X-ray Scattering (SAXS) and X-ray Photon Correlation Spectroscopy (XPCS). The application of modern area detectors with up to 2-kHz frame-rate enabled the study of PNIPAm systems via XPCS on a sub-millisecond time scale. The implementation of silica-PNIPAm core-shell particle systems allows to study the temperature-dependent behaviour of PNIPAm while the silica core provides a scattering object with large contrast for X-rays. Experiments have been performed in the vicinity of the volume phase transition of PNIPAm at the so-called lower critical solution temperature (LCST) of 32°C. The particle systems were studied with different core-to-shell size ratios and various concentrations spanning from dilute suspensions with $\Phi_{\text{eff}} \approx 0.03$ to over-packed sample systems with $\Phi_{\text{eff}} \approx 2$. The temperature-dependent particle sizes were obtained from dilute samples by DLS.

A sample (SP-2B) with a concentration of $\Phi_{\text{eff}} = 0.55$ has been selected to be discussed in detail. The results obtained by XPCS have been classified in three different temperature regimes as shown by the q- and temperature-dependence of the intensity correlation functions: Regime A was defined as the low temperature regime ($T <$ LCST) where the particle motion was found to be sub-diffusive with a KWW exponent $\gamma < 1$ and an anomalous relation of $\tau_{\text{c}} \propto q^{-3}$. In this regime the PNIPAm shell is swollen which suggests a model in which silica as quasi-tracer particles in a polymer matrix undergo Zimm-like dynamics in the surrounding polymer chains. Passing the LCST, an intermediate region B was defined for $32°\text{C} < T < 37°\text{C}$. The rapid collapse of the particles found for dilute suspensions in this temperature regime B is reflected in the concentrated system by a strong decrease of the relaxation time and hence a strong speed-up of the particles. At $T \approx 37°\text{C}$, which is defined as threshold temperature T_{c}, the dynamics of the system changes indicating a transition of the system. The region $T \geq T_{\text{c}}$ is defined as temperature regime C. Here, the system shows an increase of τ_{c} by several orders of magnitude, pointing towards a sudden slowing down of the system. Furthermore, the correlation functions become compressed ($\gamma > 1$) and the relaxation times are inversely proportional to q ($\tau_{\text{c}} \propto q^{-1}$). This relation matches the general behaviour of PNIPAm hydrogels [14]. This supports the transition from repulsive to attractive particle forces which is indicated by the $I(q)$. During the heating process, the colloidal silica-PNIPAm system undergoes a phase transition from a polymer-dominated liquid where the structural relaxation process speeds up upon raising the temperature until it rapidly turns into a jammed colloidal gel state without showing any indication of ageing.

The temperature-induced transition of structure and dynamics was found to be concentration dependent. In a study with systematically varied Φ_{eff}, all concentrations show an acceleration of the observed particle motion upon heating for $T < T_{\text{c}}$, with slower dynamics

for higher concentrations. For $T > T_c$ the corresponding behaviour varies with concentration. The slowing down of dynamics at T_c was found to be present for $\Phi_{eff} > 0.095$. On the contrary to the concentration-dependence of the dynamic behaviour, the SAXS data indicate a transition from repulsive to attractive forces as a result of the collapsing shell for all concentrations.

The attractive interparticle interactions paired with the slowing down of dynamics support the interpretation of colloidal gel formation in the dispersion once the particle shells are collapsed. Both effects are more pronounced for dense particle packings and influence the dynamics leading to the transition of dynamics with a characteristic relaxation time in the range of $\tau_c \approx 10\,s$. Additionally, the low-temperature PNIPAm shell thickness has a clear influence on particle motion before the transition of dynamics occurs. While particles with a shell thickness of $d \approx 10\,nm$ show diffusive behaviour with a KWW exponent of $\gamma = 1$, the g_2 functions become stretched for thicker shells ($d \approx 75\,nm$ and $140\,nm$) and thus show a shift towards sub-diffusive dynamics with $\gamma < 1$. Here, the critical transition temperature T_c was found to be independent of the PNIPAm shell size. The alluded temperature-dependent transition of structure and dynamics in highly concentrated systems as well as the particle size was demonstrated to be fully reversible with increase and subsequent reduction of the temperature in a broad range around the LCST. Based on all results a phase diagram with the overall temperature- and concentration dependence of silica-PNIPAm particles can be presented for the first time. It separates two different fluid states from a rearrangement phase and a jammed state at high packing fractions and temperatures where the system shows the behaviour of a colloidal gel. No crystal formation was present at any Φ_{eff} or temperature in contrast to studies on pure PNIPAm microgels [41].

The LCST commonly classifies the temperature-dependent behaviour of PNIPAm into two regimes where the particles are swollen or collapsed respectively. This thesis demonstrates another critical temperature $T_c \approx 37°C$. T_c is constant for all concentrated systems that show a temperature-induced transition of structure and dynamics. For highly concentrated colloidal PNIPAm systems, as found in smart nano- or micro-structured materials, the transition temperature T_c is more decisive than the LCST.

In future experiments, increasing the particle stiffness with higher cross-linking and aiming for highly monodisperse systems might enable a temperature-induced transition from a fluid to a crystalline state. A stiffer but disperse system can evolve into a glassy state, which is usually observed for supercooled liquids or high packing fractions. Hence, the phase diagram may be extended with a third axis relating to stiffness, covering more phases. Furthermore, more can be learned about tuning the de-swelling behaviour with co-solvents. Here, different amounts of TMAO have been added to the silica-PNIPAm suspension resulting in a shift of the LCST to lower temperatures. A clear preferential hydrophobic state was found with increasing TMAO concentration. Further studies have investigated the effect of various additions such as salt and ethanol on the de-swelling behaviour of PNIPAm hydrogels or single nanogel particles [121–123]. The investigation of the influence of co-solvents on structure and dynamics of densely-packed PNIPAm

systems would be an important next step.

This thesis reveals broad insight in the dynamic behaviour of silica-PNIPam nanogels during the volume phase transition of PNIPAm. However, the experimental access to probe the folding kinetics of PNIPAm chains and the possibly linked particle dynamics on this time-scale is limited. With the de-swelling thermo-response occurring on a microsecond time-scale [13] the trigger frequency of the current common photon-counting area detectors is too low and the flux is insufficient for reasonable statistics at shorter illumination times. Here, X-ray Free Electron Lasers (XFELs) can give access to ultrashort high-intensity coherent light pulses which enable ultrafast pump–probe experiments on ultrafast timescales with less than 100 femtoseconds, as for the European XFEL (Schenefeld, Germany). Furthermore, the upgrades of third-generation storage ring sources to diffraction-limited storage rings as PETRA IV [124] and ESRF-EBS [125], will provide an X-ray beam 100 times more brilliant and coherent than present. With the upgrades ten thousand times faster times and hence sub-microsecond dynamics can be approached which will enable the access to PNIPAm folding kinetics and polymer dynamics.

Bibliography

[1] R. Evans, D. Frenkel, and M. Dijkstra, "From simple liquids to colloids and soft matter", *Phys. Today* **72** (2019), no. 2, 38–39. doi:10.1063/pt.3.4135.

[2] A. P. Gast and W. B. Russel, "Simple Ordering in Complex Fluids", *Phys. Today* **51** (1998), no. 12, 24–30. doi:10.1063/1.882495.

[3] P. J. Yunker, K. Chen, M. D. Gratale, M. A. Lohr, T. Still, and A. G. Yodh, "Physics in ordered and disordered colloidal matter composed of poly(N-isopropylacrylamide) microgel particles", *Rep. Prog. Phys.* **77** (2014), no. 5, 056601. doi:10.1088/0034-4885/77/5/056601.

[4] M. Das, H. Zhang, and E. Kumacheva, "Microgels: old materials with new applications", *Annu. Rev. Mater. Res.* **36** (2006) 117–142. doi:10.1146/annurev.matsci.36.011205.123513.

[5] Y. Guan and Y. Zhang, "PNIPAM microgels for biomedical applications: from dispersed particles to 3D assemblies", *Soft Matter* **7** (2011), no. 14, 6375–6384. doi:10.1039/C0SM01541E.

[6] M. Karg, S. Wellert, I. Pastoriza-Santos, A. Lapp, L. M. Liz-Marzán, and T. Hellweg, "Thermoresponsive core–shell microgels with silica nanoparticle cores: size, structure, and volume phase transition of the polymer shell", *Phys. Chem. Chem. Phys.* **10** (2008), no. 44, 6708. doi:10.1039/b802676a.

[7] S. Nayak and L. A. Lyon, "Soft Nanotechnology with Soft Nanoparticles", *Angew. Chem. Int. Ed.* **44** (2005), no. 47, 7686–7708. doi:10.1002/anie.200501321.

[8] D. M. Heyes and A. C. Brańka, "Interactions between microgel particles", *Soft Matter* **5** (2009), no. 14, 2681. doi:10.1039/b901894h.

[9] H. Senff, W. Richtering, C. Norhausen, A. Weiss, and M. Ballauff, "Rheology of a Temperature Sensitive Core-Shell Latex", *Langmuir* **15** (1999), no. 1, 102–106. doi:10.1021/la980979q.

[10] K. László, A. Fluerasu, A. Moussaïd, and E. Geissler, "Deswelling kinetics of PNIPA gels", *Soft Matter* **6** (2010), no. 18, 4335–4338. doi:10.1039/C0SM00297F.

[11] S. A. Deshmukh, S. K. Sankaranarayanan, K. Suthar, and D. C. Mancini, "Role of solvation dynamics and local ordering of water in inducing conformational transitions in poly (N-isopropylacrylamide) oligomers through the LCST", *J. Phys. Chem. B* **116** (2012), no. 9, 2651–2663. doi:10.1021/jp210788u.

[12] S. M. Hashmi and E. R. Dufresne, "Mechanical properties of individual microgel particles through the deswelling transition", *Soft Matter* **5** (2009), no. 19, 3682–3688. doi:10.1039/B906051K.

[13] J. Wang, D. Gan, L. A. Lyon, and M. A. El-Sayed, "Temperature-jump investigations of the kinetics of hydrogel nanoparticle volume phase transitions", *J. Am. Chem. Soc.* **123** (2001), no. 45, 11284–11289. doi:10.1021/ja016610w.

[14] R. Hernández, M. Criado, A. Nogales, M. Sprung, C. Mijangos, and T. A. Ezquerra, "Deswelling of Poly (N-isopropylacrylamide) Derived Hydrogels and Their Nanocomposites with Iron Oxide Nanoparticles As Revealed by X-ray Photon Correlation Spectroscopy", *Macromolecules* **48** (2015), no. 2, 393–399. doi:10.1021/ma502118a.

[15] P. Holmqvist, P. Mohanty, G. Nägele, P. Schurtenberger, and M. Heinen, "Structure and dynamics of loosely cross-linked ionic microgel dispersions in the fluid regime", *Phys. Rev. Lett.* **109** (2012), no. 4, 048302. doi:10.1103/PhysRevLett.109.048302.

[16] A. Zaccone, J. J. Crassous, B. Béri, and M. Ballauff, "Quantifying the Reversible Association of Thermosensitive Nanoparticles", *Physical Review Letters* **107** (oct, 2011) 168303. doi:10.1103/physrevlett.107.168303.

[17] Q. Li, X. Peng, and G. B. McKenna, "Physical aging and compressed exponential behaviors in a model soft colloidal system", *Soft Matter* **15** (2019), no. 11, 2336–2347. doi:10.1039/c8sm02042f.

[18] F. Lehmkühler, J. Valerio, D. Sheyfer, W. Roseker, M. A. Schroer, B. Fischer, K. Tono, M. Yabashi, T. Ishikawa, and G. Grübel, "Dynamics of soft nanoparticle suspensions at hard X-ray FEL sources below the radiation-damage threshold", *IUCrJ* **5** (2018), no. 6, 801–807. doi:10.1107/S2052252518013696.

[19] W. H. De Jeu, "Basic X-ray scattering for soft matter". Oxford University Press, 2016.

[20] J. Als-Nielsen and D. McMorrow, "Elements of modern X-ray physics". John Wiley & Sons, 2011.

[21] S. Granick, "Soft Matter in a Tight Spot", *Phys. Today* **52** (1999), no. 7, 26–31. doi:10.1063/1.882747.

[22] G. Grübel and F. Zontone, "Correlation spectroscopy with coherent X-rays", *J. Alloys Compd.* **362** (2004), no. 1, 3–11. doi:10.1016/S0925-8388(03)00555-3.

[23] A. Robert, J. Wagner, T. Autenrieth, W. Härtl, and G. Grübel, "Coherent X-rays as a new probe for the investigation of the dynamics of opaque colloidal suspensions", *J. Magn. Magn. Mater.* **289** (2005) 47–49. doi:10.1016/j.jmmm.2004.11.014.

[24] H. Löwen, "Melting, freezing and colloidal suspensions", *Phys. Rep.* **237** (1994), no. 5, 249–324. doi:10.1016/0370-1573(94)90017-5.

[25] T. A. Witten, "Structured Fluids", *Phys. Today* **43** (1990), no. 7, 21–28. doi:10.1063/1.881249.

[26] H. Hamaker, "The London—van der Waals attraction between spherical particles", *Physica* **4** (1937), no. 10, 1058–1072. doi:10.1016/s0031-8914(37)80203-7.

[27] H. Löwen, "Possibilities of phase separation in colloidal suspensions", *Physica A* **235** (1997), no. 1-2, 129–141. doi:10.1016/s0378-4371(96)00334-2.

[28] W. G. Hoover and F. H. Ree, "Melting Transition and Communal Entropy for Hard Spheres", *The Journal of Chemical Physics* **49** (1968), no. 8, 3609–3617. doi:10.1063/1.1670641.

[29] P. N. Pusey and W. van Megen, "Phase behaviour of concentrated suspensions of nearly hard colloidal spheres", *Nature* **320** (1986), no. 6060, 340–342. doi:10.1038/320340a0.

[30] R. J. Baxter, "Percus–Yevick Equation for Hard Spheres with Surface Adhesion", *The Journal of Chemical Physics* **49** (1968), no. 6, 2770–2774. doi:10.1063/1.1670482.

[31] S. V. G. Menon, C. Manohar, and K. S. Rao, "A new interpretation of the sticky hard sphere model", *The Journal of Chemical Physics* **95** (1991), no. 12, 9186–9190. doi:10.1063/1.461199.

[32] R. Piazza, V. Peyre, and V. Degiorgio, ""Sticky hard spheres" model of proteins near crystallization: A test based on the osmotic compressibility of lysozyme solutions", *Physical Review E* **58** (1998), no. 3, R2733–R2736. doi:10.1103/physreve.58.r2733.

[33] S. Buzzaccaro, R. Rusconi, and R. Piazza, ""Sticky" Hard Spheres: Equation of State, Phase Diagram, and Metastable Gels", *Phys. Rev. Lett.* **99** (2007), no. 9,. doi:10.1103/physrevlett.99.098301.

[34] D. Rosenbaum, P. C. Zamora, and C. F. Zukoski, "Phase Behavior of Small Attractive Colloidal Particles", *Phys. Rev. Lett.* **76** (1996), no. 1, 150–153. doi:10.1103/physrevlett.76.150.

[35] H. Löwen, "Kolloide - auch für Physiker interessant?: Kolloidale Suspensionen als Musterbeispiele für Modelle der statistischen Mechanik", *Phys. J.* **51** (1995), no. 3, 165–168. doi:10.1002/phbl.19950510306.

[36] E. J. W. Verwey and J. T. G. Overbeek, "Theory of the stability of lyophobic colloids", *J. Colloid Sci.* **10** (1955), no. 2, 224–225. doi:10.1021/j150453a001.

[37] P. N. Pusey, E. Zaccarelli, C. Valeriani, E. Sanz, W. C. K. Poon, and M. E. Cates, "Hard spheres: crystallization and glass formation", *Philosophical Transactions of the Royal Society A: Mathematical, Physical and Engineering Sciences* **367** (2009), no. 1909, 4993–5011. doi:10.1098/rsta.2009.0181.

[38] E. Hückel, "Zur theorie konzentrierterer wässeriger Lösungen starker elektrolyte", *Phys. Z* **26** (1925) 93–147.

[39] G. Nägele, M. Watzlawek, and R. Klein, "Hard spheres versus Yukawa particles: Differences and similarities", *Progress in Colloid & Polymer Science* **104** (1997), no. 1, 31–39. doi:10.1007/bf01182412.

[40] E. B. Sirota, H. D. Ou-Yang, S. K. Sinha, P. M. Chaikin, J. D. Axe, and Y. Fujii, "Complete phase diagram of a charged colloidal system: A synchro- tron x-ray scattering study", *Phys. Rev. Lett.* **62** (1989), no. 13, 1524–1527. doi:10.1103/physrevlett.62.1524.

[41] U. Gasser, J.-J. Lietor-Santos, A. Scotti, O. Bunk, A. Menzel, and A. Fernandez-Nieves, "Transient formation of bcc crystals in suspensions of poly(N-isopropylacrylamide)-based microgels", *Physical Review E* **88** (2013), no. 5,. doi:10.1103/physreve.88.052308.

[42] U. Gasser and A. Fernandez-Nieves, "Crystal structure of highly concentrated, ionic microgel suspensions studied by small-angle x-ray scattering", *Physical Review E* **81** (2010), no. 5,. doi:10.1103/physreve.81.052401.

[43] W. C. K. Poon, E. R. Weeks, and C. P. Royall, "On measuring colloidal volume fractions", *Soft Matter* **8** (2012), no. 1, 21–30. doi:10.1039/c1sm06083j.

[44] P. S. Mohanty, S. Nöjd, K. van Gruijthuijsen, J. J. Crassous, M. Obiols-Rabasa, R. Schweins, A. Stradner, and P. Schurtenberger, "Interpenetration of polymeric microgels at ultrahigh densities", *Sci. Rep.* **7** (2017), no. 1, 1487. doi:10.1038/s41598-017-01471-3.

[45] M. J. Bergman, N. Gnan, M. Obiols-Rabasa, J.-M. Meijer, L. Rovigatti, E. Zaccarelli, and P. Schurtenberger, "A new look at effective interactions between microgel particles", *Nat. Commun.* **9** (2018), no. 1, 5039. doi:10.1038/s41467-018-07332-5.

[46] G. M. Conley, P. Aebischer, S. Nöjd, P. Schurtenberger, and F. Scheffold, "Jamming and overpacking fuzzy microgels: Deformation, interpenetration, and compression", *Sci. Adv.* **3** (2017), no. 10, e1700969. doi:10.1126/sciadv.1700969.

[47] M. Urich and A. R. Denton, "Swelling, structure, and phase stability of compressible microgels", *Soft Matter* **12** (2016), no. 44, 9086–9094. doi:10.1039/c6sm02056a.

[48] G. Romeo, A. Fernandez-Nieves, H. M. Wyss, D. Acierno, and D. A. Weitz, "Temperature-Controlled Transitions Between Glass, Liquid, and Gel States in Dense p-NIPA Suspensions", *Adv. Mater.* **22** (2010), no. 31, 3441–3445. doi:10.1002/adma.200904189.

[49] Y. Han, N. Y. Ha, A. M. Alsayed, and A. G. Yodh, "Melting of two-dimensional tunable-diameter colloidal crystals", *Physical Review E* **77** (2008), no. 4,. doi:10.1103/physreve.77.041406.

[50] J. R. Seth, L. Mohan, C. Locatelli-Champagne, M. Cloitre, and R. T. Bonnecaze, "A micromechanical model to predict the flow of soft particle glasses", *Nat. Mater.* **10** (2011), no. 11, 838–843. doi:10.1038/nmat3119.

[51] J. C. Pàmies, A. Cacciuto, and D. Frenkel, "Phase diagram of Hertzian spheres", arXiv:http://arxiv.org/abs/0811.2227v4. doi:10.1063/1.3186742.

[52] B. Sierra-Martin and A. Fernandez-Nieves, "Phase and non-equilibrium behaviour of microgel suspensions as a function of particle stiffness", *Soft Matter* **8** (2012), no. 15, 4141. doi:10.1039/c2sm06973c.

[53] M. A. Schroer, J. Michalowsky, B. Fischer, J. Smiatek, and G. Grübel, "Stabilizing effect of TMAO on globular PNIPAM states: preferential attraction induces preferential hydration", *Phys. Chem. Chem. Phys.* **18** (2016), no. 46, 31459–31470. doi:10.1039/c6cp05991k.

[54] A. Pica and G. Graziano, "Why does TMAO stabilize the globule state of PNIPAM?", *Polymer* **124** (2017) 101–106. doi:10.1016/j.polymer.2017.07.051.

[55] P. M. Reddy, M. Taha, P. Venkatesu, A. Kumar, and M.-J. Lee, "Destruction of hydrogen bonds of poly(N-isopropylacrylamide) aqueous solution by trimethylamine N-oxide", *The Journal of Chemical Physics* **136** (2012), no. 23, 234904. doi:10.1063/1.4729156.

[56] Y. Zhang, S. Furyk, D. E. Bergbreiter, and P. S. Cremer, "Specific Ion Effects on the Water Solubility of Macromolecules: PNIPAM and the Hofmeister Series", *J. Am. Chem. Soc.* **127** (2005), no. 41, 14505–14510. doi:10.1021/ja0546424.

[57] S. Micciulla, J. Michalowsky, M. A. Schroer, C. Holm, R. von Klitzing, and J. Smiatek, "Concentration dependent effects of urea binding to poly(N-isopropylacrylamide) brushes: a combined experimental and numerical study", *Phys. Chem. Chem. Phys.* **18** (2016), no. 7, 5324–5335. doi:10.1039/c5cp07544k.

[58] I. Bischofberger, D. C. E. Calzolari, and V. Trappe, "Co-nonsolvency of PNiPAM at the transition between solvation mechanisms", *Soft Matter* **10** (2014), no. 41, 8288–8295. doi:10.1039/c4sm01345j.

[59] P. H. Yancey, "Organic osmolytes as compatible, metabolic and counteracting cytoprotectants in high osmolarity and other stresses", *J. Exp. Biol.* **208** (2005), no. 15, 2819–2830. doi:10.1242/jeb.01730.

[60] F. Meersman, D. Bowron, A. K. Soper, and M. H. J. Koch, "An X-ray and neutron scattering study of the equilibrium between trimethylamine N-oxide and urea in aqueous solution", *Phys. Chem. Chem. Phys.* **13** (2011), no. 30, 13765. doi:10.1039/c1cp20842j.

[61] M. Karg, S. Wellert, S. Prevost, R. Schweins, C. Dewhurst, L. M. Liz-Marzán, and T. Hellweg, "Well defined hybrid PNIPAM core-shell microgels: size variation of the silica nanoparticle core", *Colloid Polym. Sci.* **289** (2010), no. 5-6, 699–709. doi:10.1007/s00396-010-2327-2.

[62] N. Nun, S. Hinrichs, M. A. Schroer, D. Sheyfer, G. Grübel, and B. Fischer, "Tuning the Size of Thermoresponsive Poly (N-Isopropyl Acrylamide) Grafted Silica Microgels", *Gels* **3** (2017), no. 3, 34. doi:10.3390/gels3030034.

[63] M. Karg, I. Pastoriza-Santos, L. M. Liz-Marzán, and T. Hellweg, "A versatile approach for the preparation of thermosensitive PNIPAM core–shell microgels with nanoparticle cores", *ChemPhysChem* **7** (2006), no. 11, 2298–2301. doi:10.1002/cphc.200600483.

[64] N. Stribeck, "X-ray scattering of soft matter". Springer Science & Business Media, 2007.

[65] G. Grübel, A. Madsen, and A. Robert, "Soft Matter Characterization", ch. X-ray photon correlation spectroscopy (XPCS), pp. 953–995. Springer, 2008.

[66] T. Li, A. J. Senesi, and B. Lee, "Small Angle X-ray Scattering for Nanoparticle Research", *Chem. Rev.* **116** (2016), no. 18, 11128–11180. doi:10.1021/acs.chemrev.5b00690.

[67] P. J. Flory, "Molecular Size Distribution in Linear Condensation Polymers1", *J. Am. Chem. Soc.* **58** (1936), no. 10, 1877–1885. doi:10.1021/ja01301a016.

[68] M. Kotlarchyk and S.-H. Chen, "Analysis of small angle neutron scattering spectra from polydisperse interacting colloids", *The Journal of Chemical Physics* **79** (1983), no. 5, 2461–2469. doi:10.1063/1.446055.

[69] C. P. Royall, S. R. Williams, and H. Tanaka, "Vitrification and gelation in sticky spheres", *The Journal of Chemical Physics* **148** (2018), no. 4, 044501. doi:10.1063/1.5000263.

[70] B. J. Berne and R. Pecora, "Dynamic light scattering: with applications to chemistry, biology, and physics". Courier Corporation, 1976.

[71] G. Williams and D. C. Watts, "Non-symmetrical dielectric relaxation behaviour arising from a simple empirical decay function", *Trans. Faraday Soc.* **66** (1970) 80–85. doi:10.1039/TF9706600080.

[72] H. Löwen, J.-P. Hansen, and J.-N. Roux, "Brownian dynamics and kinetic glass transition in colloidal suspensions", *Phys. Rev. A* **44** (1991), no. 2, 1169. doi:10.1103/PhysRevA.44.1169.

[73] S. Dierker, R. Pindak, R. Fleming, I. Robinson, and L. Berman, "X-ray photon correlation spectroscopy study of Brownian motion of gold colloids in glycerol", *Phys. Rev. Lett.* **75** (1995), no. 3, 449. doi:10.1103/PhysRevLett.75.449.

[74] R. Poling-Skutvik, K. I. S. Mongcopa, A. Faraone, S. Narayanan, J. C. Conrad, and R. Krishnamoorti, "Structure and dynamics of interacting nanoparticles in semidilute polymer solutions", *Macromolecules* **49** (2016), no. 17, 6568–6577. doi:10.1021/acs.macromol.6b01277.

[75] T. Hoshino, D. Murakami, Y. Tanaka, M. Takata, H. Jinnai, and A. Takahara, "Dynamical crossover between hyperdiffusion and subdiffusion of polymer-grafted nanoparticles in a polymer matrix", *Phys. Rev. E* **88** (2013), no. 3, 032602. doi:10.1103/PhysRevE.88.032602.

[76] H. Guo, G. Bourret, R. B. Lennox, M. Sutton, J. L. Harden, and R. L. Leheny, "Entanglement-Controlled Subdiffusion of Nanoparticles within Concentrated Polymer Solutions", *Phys. Rev. Lett.* **109** (2012), no. 5,. doi:10.1103/physrevlett.109.055901.

[77] A. Zilman and R. Granek, "Undulations and dynamic structure factor of membranes", *Phys. Rev. Lett.* **77** (1996), no. 23, 4788. doi:10.1103/PhysRevLett.77.4788.

[78] M. Mihailescu, M. Monkenbusch, H. Endo, J. Allgaier, G. Gompper, J. Stellbrink, D. Richter, B. Jakobs, T. Sottmann, and B. Farago, "Dynamics of bicontinuous microemulsion phases with and without amphiphilic block-copolymers", *J. Chem. Phys.* **115** (2001), no. 20, 9563–9577. doi:10.1063/1.1413509.

[79] P. Falus, M. Borthwick, S. Narayanan, A. Sandy, and S. Mochrie, "Crossover from stretched to compressed exponential relaxations in a polymer-based sponge phase", *Phys. Rev. Lett.* **97** (2006), no. 6, 066102. doi:10.1103/PhysRevLett.97.066102.

[80] S. Komura, T. Takeda, Y. Kawabata, S. K. Ghosh, H. Seto, and M. Nagao, "Dynamical fluctuation of the mesoscopic structure in ternary C 12 E 5–water–n-octane amphiphilic system", *Phys. Rev. E* **63** (2001), no. 4, 041402. doi:10.1103/PhysRevE.63.041402.

[81] H. Guo, G. Bourret, R. B. Lennox, M. Sutton, J. L. Harden, and R. L. Leheny, "Entanglement-controlled subdiffusion of nanoparticles within concentrated

polymer solutions", *Phys. Rev. Lett.* **109** (2012), no. 5, 055901. doi:10.1103/PhysRevLett.109.055901.

[82] R. A. Narayanan, P. Thiyagarajan, S. Lewis, A. Bansal, L. Schadler, and L. Lurio, "Dynamics and internal stress at the nanoscale related to unique thermomechanical behavior in polymer nanocomposites", *Phys. Rev. Lett.* **97** (2006), no. 7, 075505. doi:10.1103/PhysRevLett.97.075505.

[83] H. Guo, G. Bourret, M. K. Corbierre, S. Rucareanu, R. B. Lennox, K. Laaziri, L. Piche, M. Sutton, J. L. Harden, and R. L. Leheny, "Nanoparticle motion within glassy polymer melts", *Phys. Rev. Lett.* **102** (2009), no. 7, 075702. doi:10.1103/PhysRevLett.102.075702.

[84] W.-S. Jang, P. Koo, K. Bryson, S. Narayanan, A. Sandy, T. P. Russell, and S. G. Mochrie, "Dynamics of cadmium sulfide nanoparticles within polystyrene melts", *Macromolecules* **47** (2014), no. 18, 6483–6490. doi:10.1021/ma500956b.

[85] H. Guo, S. Ramakrishnan, J. L. Harden, and R. L. Leheny, "Gel formation and aging in weakly attractive nanocolloid suspensions at intermediate concentrations", *J. Chem. Phys.* **135** (2011), no. 15, 154903. doi:10.1063/1.3653380.

[86] C. Caronna, Y. Chushkin, A. Madsen, and A. Cupane, "Dynamics of nanoparticles in a supercooled liquid", *Phys. Rev. Lett.* **100** (2008), no. 5, 055702. doi:10.1103/PhysRevLett.100.055702.

[87] B. Chung, S. Ramakrishnan, R. Bandyopadhyay, D. Liang, C. Zukoski, J. Harden, and R. Leheny, "Microscopic dynamics of recovery in sheared depletion gels", *Phys. Rev. Lett.* **96** (2006), no. 22, 228301. doi:10.1103/PhysRevLett.96.228301.

[88] L. Cipelletti, S. Manley, R. Ball, and D. Weitz, "Universal aging features in the restructuring of fractal colloidal gels", *Phys. Rev. Lett.* **84** (2000), no. 10, 2275. doi:10.1103/PhysRevLett.84.2275.

[89] R. Mangal, S. Srivastava, S. Narayanan, and L. A. Archer, "Size-dependent particle dynamics in entangled polymer nanocomposites", *Langmuir* **32** (2016), no. 2, 596–603. doi:10.1021/acs.langmuir.5b03311.

[90] A. Duri and L. Cipelletti, "Length scale dependence of dynamical heterogeneity in a colloidal fractal gel", *EPL (Europhysics Letters)* **76** (2006), no. 5, 972. doi:10.1209/epl/i2006-10357-4.

[91] P. Kwaśniewski, A. Fluerasu, and A. Madsen, "Anomalous dynamics at the hard-sphere glass transition", *Soft Matter* **10** (2014), no. 43, 8698–8704. doi:10.1039/C4SM01671H.

[92] H. Conrad, F. Lehmkühler, B. Fischer, F. Westermeier, M. Schroer, Y. Chushkin, C. Gutt, M. Sprung, and G. Grübel, "Correlated heterogeneous dynamics in

glass-forming polymers", *Phys. Rev. E* **91** (2015), no. 4, 042309. doi:10.1103/PhysRevE.91.042309.

[93] X. Lu, S. Mochrie, S. Narayanan, A. Sandy, and M. Sprung, "How a liquid becomes a glass both on cooling and on heating", *Phys. Rev. Lett.* **100** (2008), no. 4, 045701. doi:10.1103/PhysRevLett.100.045701.

[94] W. Stöber, A. Fink, and E. Bohn, "Controlled growth of monodisperse silica spheres in the micron size range", *J. Colloid Interface Sci.* **26** (1968), no. 1, 62–69. doi:10.1016/0021-9797(68)90272-5.

[95] M. A. Boles and D. V. Talapin, "Many-Body Effects in Nanocrystal Superlattices: Departure from Sphere Packing Explains Stability of Binary Phases", *Journal of the American Chemical Society* **137** (mar, 2015) 4494–4502. doi:10.1021/jacs.5b00839.

[96] M. A. Boles, M. Engel, and D. V. Talapin, "Self-Assembly of Colloidal Nanocrystals: From Intricate Structures to Functional Materials", *Chemical Reviews* **116** (aug, 2016) 11220–11289. doi:10.1021/acs.chemrev.6b00196.

[97] Z. Jiang, X. Li, J. Strzalka, M. Sprung, T. Sun, A. R. Sandy, S. Narayanan, D. R. Lee, and J. Wang, "The dedicated high-resolution grazing-incidence X-ray scattering beamline 8-ID-E at the Advanced Photon Source", *J. Synch. Rad.* **19** (2012), no. 4, 627–636. doi:10.1107/s0909049512022017.

[98] "Beamline 8-ID-I: X-ray Photon Correlation Spectroscopy". https://beam.aps.anl.gov/pls/apsweb/beamline_display_pkg.display_beamline?p_beamline_num_c=12. Accessed: 31.05.19.

[99] "ID10 - Soft interfaces and coherent scattering beamline". https://www.esrf.eu/home/UsersAndScience/Experiments/CBS/ID10/ID10EH2/presentation.html. Acessed: 31.05.2019.

[100] "P10 beamline specifications". http://photon-science.desy.de/facilities/petra_iii/beamlines/p10_coherence_applications/beamline_specifications/index_eng.html. Accessed: 30.05.19.

[101] D. Pennicard, S. Lange, S. Smoljanin, J. Becker, H. Hirsemann, M. Epple, and H. Graafsma, "Development of LAMBDA: Large Area Medipix-Based Detector Array", *J. Instrum.* **6** (2011), no. 11, C11009. doi:10.1088/1748-0221/6/11/C11009.

[102] C. Ponchut, J. Rigal, J. Clément, E. Papillon, A. Homs, and S. Petitdemange, "MAXIPIX, a fast readout photon-counting X-ray area detector for synchrotron applications", *J. Instrum.* **6** (2011), no. 01, C01069. doi:10.1088/1748-0221/6/01/C01069.

[103] T. Narayanan, M. Sztucki, G. Belina, and F. Pignon, "Microstructure and Rheology near an Attractive Colloidal Glass Transition", *Phys. Rev. Lett.* **96** (2006), no. 25, 258301. doi:10.1103/physrevlett.96.258301.

[104] J. Wu, B. Zhou, and Z. Hu, "Phase Behavior of Thermally Responsive Microgel Colloids", *Phys. Rev. Lett.* **90** (2003) 048304. doi:10.1103/PhysRevLett.90.048304.

[105] C. M. Jeffries, M. A. Graewert, D. I. Svergun, and C. E. Blanchet, "Limiting radiation damage for high-brilliance biological solution scattering: practical experience at the EMBL P12 beamline PETRAIII", *Journal of Synchrotron Radiation* **22** (2015), no. 2, 273–279. doi:10.1107/s1600577515000375.

[106] M. Berger, J. Hubbel, S. Seltzer, and K. Olsen, "XCOM-Photon Cross Sections Database, NIST Standard Reference Database 8", 1987. doi:10.18434/t48g6x.

[107] C. Wu and X. Wang, "Globule-to-coil transition of a single homopolymer chain in solution", *Phys. Rev. Lett.* **80** (1998), no. 18, 4092. doi:10.1103/PhysRevLett.80.4092.

[108] A.-M. Philippe, D. Truzzolillo, J. Galvan-Myoshi, P. Dieudonné-George, V. Trappe, L. Berthier, and L. Cipelletti, "Glass transition of soft colloids", *Phys. Rev. E* **97** (2018), no. 4,. doi:10.1103/physreve.97.040601.

[109] P. D. Gennes, "Liquid dynamics and inelastic scattering of neutrons", *Physica* **25** (1959), no. 7-12, 825–839. doi:10.1016/0031-8914(59)90006-0.

[110] S. Capaccioli, M. Paluch, D. Prevosto, L.-M. Wang, and K. Ngai, "Many-body nature of relaxation processes in glass-forming systems", *J. Phys. Chem. Lett.* **3** (2012), no. 6, 735–743. doi:10.1021/jz201634p.

[111] H. Tanaka, "Origin of the excess wing and slow β relaxation of glass formers: A unified picture of local orientational fluctuations", *Phys. Rev. E* **69** (2004), no. 2, 021502. doi:10.1103/PhysRevE.69.021502.

[112] P. G. Debenedetti and F. H. Stillinger, "Supercooled liquids and the glass transition", *Nature* **410** (2001), no. 6825, 259. doi:10.1038/35065704.

[113] Q. Zhang, D. Bahadur, E. M. Dufresne, P. Grybos, P. Kmon, R. L. Leheny, P. Maj, S. Narayanan, R. Szczygiel, S. Ramakrishnan, et al., "Dynamic scaling of colloidal gel formation at intermediate concentrations", *Phys. Rev. Lett.* **119** (2017), no. 17, 178006. doi:10.1103/PhysRevLett.119.178006.

[114] K. László, A. Fluerasu, A. Moussaïd, and E. Geissler, "Kinetics of jammed systems: PNIPA gels", in *Macromolecular Symposia*, volume 306, pp. 27–32, Wiley Online Library. 2011.

[115] A. Y. C. Koh and B. R. Saunders, "Small-Angle Neutron Scattering Study of Temperature-Induced Emulsion Gelation: the Role of Sticky Microgel Particles", *Langmuir* **21** (2005), no. 15, 6734–6741. doi:10.1021/la050600h.

[116] J. Luo, G. Yuan, C. Zhao, C. C. Han, J. Chen, and Y. Liu, "Gelation of large hard particles with short-range attraction induced by bridging of small soft microgels", *Soft Matter* **11** (2015), no. 12, 2494–2503. doi:10.1039/c4sm02165g.

[117] Z. Meng, J. K. Cho, S. Debord, V. Breedveld, and L. A. Lyon, "Crystallization Behavior of Soft, Attractive Microgels", *The Journal of Physical Chemistry B* **111** (2007), no. 25, 6992–6997. doi:10.1021/jp073122n.

[118] H. Senff and W. Richtering, "Temperature sensitive microgel suspensions: Colloidal phase behavior and rheology of soft spheres", *J. Chem. Phys.* **111** (1999), no. 4, 1705–1711. doi:10.1063/1.479430.

[119] R. Shu, W. Sun, Y. Liu, T. Wang, C. Wang, X. Liu, and Z. Tong, "The jamming and unjamming transition in poly(N-isopropylacrylamide) microgel suspensions", *Colloids Surf., A* **436** (2013) 912–921. doi:10.1016/j.colsurfa.2013.08.031.

[120] A. N. S. John, V. Breedveld, and L. A. Lyon, "Phase Behavior in Highly Concentrated Assemblies of Microgels with Soft Repulsive Interaction Potentials", *J. Phys. Chem. B* **111** (2007), no. 27, 7796–7801. doi:10.1021/jp071630r.

[121] W. Liao, Y. Zhang, Y. Guan, and X. X. Zhu, "Gelation Kinetics of Thermosensitive PNIPAM Microgel Dispersions", *Macromol. Chem. Phys.* **212** (2011), no. 18, 2052–2060. doi:10.1002/macp.201100137.

[122] S. Christau, T. Moeller, J. Genzer, R. Koehler, and R. von Klitzing, "Salt-Induced Aggregation of Negatively Charged Gold Nanoparticles Confined in a Polymer Brush Matrix", *Macromolecules* **50** (2017), no. 18, 7333–7343. doi:10.1021/acs.macromol.7b00866.

[123] S. Backes, P. Krause, W. Tabaka, M. U. Witt, D. Mukherji, K. Kremer, and R. von Klitzing, "Poly(N-isopropylacrylamide) Microgels under Alcoholic Intoxication: When a LCST Polymer Shows Swelling with Increasing Temperature", *ACS Macro Letters* **6** (2017), no. 10, 1042–1046. doi:10.1021/acsmacrolett.7b00557.

[124] C. G. Schroer, I. Agapov, W. Brefeld, R. Brinkmann, Y.-C. Chae, H.-C. Chao, M. Eriksson, J. Keil, X. N. Gavaldà, R. Röhlsberger, O. H. Seeck, M. Sprung, M. Tischer, R. Wanzenberg, and E. Weckert, "PETRA IV: the ultralow-emittance source project at DESY", *Journal of Synchrotron Radiation* **25** (2018), no. 5, 1277–1290. doi:10.1107/s1600577518008858.

[125] P. Raimondi, "ESRF-EBS: The Extremely Brilliant Source Project", *Synchrotron Radiation News* **29** (2016), no. 6, 8–15. doi:10.1080/08940886.2016.1244462.

Own publications

Publications directly relating to this thesis

1. L. Frenzel, F. Lehmkühler, I. Lokteva, M. Sprung, S. Narayanan, G.Grübel, "Anomalous Dynamics of Concentrated Silica-PNIPAm Nanogels", *J. Phys. Chem. Lett.* (2019) 10, 5231-5236 doi:10.1021/acs.jpclett.9b01690

2. L. Frenzel, F. Lehmkühler, M. Koof, I. Lokteva, G.Grübel, "The Phase Diagram of Colloidal Silica-PNIPAm core-shell Nanogels", *Soft Matter* (2019) **in print** doi:10.1039/c9sm01884k

Miscellaneous

1. F. Lehmkühler, F. Schulz, M. A. Schroer, L. Frenzel, H. Lange, G. Grübel,"Local orientational order in self-assembled nanoparticle films: the role of ligand composition and salt", *J. Appl. Cryst.* (2019) 52, 777-782 doi:10.1107/S1600576719007568.

2. F. Lehmkühler, M. A. Schroer, V. Markmann, L. Frenzel, H. Lange, G. Grübel, F. Schulz, "Kinetics of pressure-induced nanocrystal superlattice formation", *Phys. Chem. Chem. Phys.*, (2019) 21, 21349-21354 doi:10.1039/C9CP04658E.

3. F. Lehmkühler, F. Schulz, M. A. Schroer, L. Frenzel, H. Lange, G. Grübel, "Heterogeneous local order in self-assembled nanoparticle films revealed by X-ray Cross Corelation", *IUCrJ* 5(3), 354 - 360 (2018) doi:10.1107/S2052252518005407.

4. M. A. Schroer, F. Lehmkühler, V. Markmann, L. Frenzel, J. Möller, H. Lange, G. Grübel, F. Schulz, "Supercrystal formation of gold nanorods by high pressure stimulation", *J. Phys. Chem. C* (2019) doi:10.1021/acs.jpcc.9b08173.

5. A. Jain, F. Schulz, I. Lokteva, L. Frenzel, G. Grübel, F. Lehmkühler, "Anisotropic and heterogeneous dynamics in an aging colloidal gel", (2019) *Soft Matter* **in review**.

Acknowledgements

First, I want to thank my PhD supervisor Prof. Dr. Gerhard Grübel for the possibility to write my thesis, the support and the trust put in me. I personally and scientifically learned a lot from you. I'm glad to have been part of your group and would do it over again the same way.

I very sincerely thank my supervisor Dr. Felix Lehmkühler for the absolute support I could always count on, the fruitful ideas, discussions, proof-reading of thesis and publications and especially for all the encouragment. Working together with you has taught me a lot and I have enjoyed participating in all the many nightshifts, conferences and workshops together. I felt we were a good team in the last years and you became a valued friend to me.

I thank Dr. Wojciech Roseker for always having advice for me, encouraging me and having an open ear whenever I needed it. Thank you for the support with the sometimes moody DLS device. You as well became a dear friend to me over the last years.

My sincere thank you also goes to Dr. Irina Lokteva, who supported me with the preparation of the samples studied in this thesis and who also participated in my experiments. I am greatful to have had your support on the chemistry part of the project.

My thank further goes to everyone of the FS-CXS group at DESY. I very quickly felt like being part of the group and I really enjoyed the last years with all the laughter, the gossip, the coffee breaks, the parties and all of the office conversations.

Thank you Avni Jain, for being my office mate in the first year and my colleague who became a dear friend.

Thank you to Michael Koof for participating in my experiments and the kind support with chemistry and sample preparation.

Thank you Matthias Riepp and Verena Markmann for being my office mates in the last years, I really enyojed it and would choose no other office.

Thanks to Joana Valerio, I'm happy I had you as my colleague and I always enjoyed chatting with you.

Thank you Donatella Rosetti for always taking care of everything, for many lovely and supporting conversations and for your patience with my Italian. I am very happy that we met.

Thank you Francesco Dallari, we only had a short overlap in the group but you were always encouraging and I also really enjoyed our conversations.

Thank you again to Felix and Wojtek for all the nice coffee breaks and conversations with beer and burgers. Our trip to the SAS conference in Michigan is one of my favorite memories from the last years.

Thank you also to Rustam Rysov, Michael Walther, André Philippi-Kobs, Dina Sheyfer,

Leonard Müller and Wonhyuk Jo for being part of my journey within the last years.

Thanks to Michael Höltig, who also shared the office with me in the first year and was always happy to give advice and explanations even long after his time in the group.

Thank you to Martin Schroer for several discussions and ideas relating to my project. Also, beamtimes with you were always fun.

Thanks to Mo and Aileen who were my "fellow sufferers" and went trough many stages together with me at the same time.

Thanks to Gerard Martí for the nice work he carried out as my summer student.

Further, I want to thank Michael Sprung for participating in my most relevant beamtime at APS and for teaching me how (not) to drive in the US. Thank you for your support, your ideas and explanations and of course also for the development of the XPCSGUI.

Thank you also to Suresh Narayanan for the support with my experiments at 8-ID, APS and with the following publications. Thanks to Yuriy Chushkin for the support at ID10, ESRF and to Fabian Westermeier for his help at P10, PETRA III and his general support and kind words.

For financial support I thank The Hamburg Centre for Ultrafast Imaging (CUI). It further was a great pleasure to be the CUI student representative together with Stephanie.

It may be a long time ago but I also want to thank my maths and physics teachers of the last years of school Markus Port and Gerd Winter. I am convinced that your teaching and motivation significantly contributed to my decision of studying physics.

I deeply want to thank all the people who unreleated to my scientific work supported me in the last years. Thanks to my Erlangen guys Jo, Max, Markus and especially Simon and Alex for sharing this academic journey with me since the beginning of our studies back in 2009. Thank you to Yara, Xenia and Svenja who were there for me, especially in the past year, whenever I struggled. Thank you to my "Lieblingsbriten" Alice and Richard for kindly helping me out with english wording and becoming dear friends. Thank you to my sister Amelie for always being her refreshingly honest self which often brings me back down to earth. And thank you to Ralph who was by my side through all the ups and downs in the past year.

Finally, I want to thank my parents for their unconditional support, precious advice and always being there for me in any situation. You were laying the foundation of my interest in science and physics. Without you I would not be where I am today.

Eidesstattliche Versicherung / Declaration on oath

Hiermit versichere ich an Eides statt, die vorliegende Dissertationsschrift selbst verfasst und keine anderen als die angegebenen Hilfsmittel und Quellen benutzt zu haben.

Die eingereichte schriftliche Fassung entspricht der auf dem elektronischen Speichermedium.

Die Dissertation wurde in der vorgelegten oder einer ähnlichen Form nicht schon einmal in einem früheren Promotionsverfahren angenommen oder als ungenügend beurteilt.

Hamburg, den 07.08.2019

Lara Frenzel